

Review

Not peer-reviewed version

Electromagnetic and Radon Earthquake Precursors

[Dimitrios Nikolopoulos](#)*, [Demetrios Cantzos](#), [Aftab Alam](#), Stavros Dimopoulos, [Ermioni Petraki](#)

Posted Date: 27 June 2024

doi: 10.20944/preprints202406.1939.v1

Keywords: electromagnetic radiation; radon gas; earthquakes; satellites; remote sensing; models; anomalies







Preprints.org is a free multidiscipline platform providing preprint service that is dedicated to making early versions of research outputs permanently available and citable. Preprints posted at Preprints.org appear in Web of Science, Crossref, Google Scholar, Scilit, Europe PMC.

Copyright: This is an open access article distributed under the Creative Commons Attribution License which permits unrestricted use, distribution, and reproduction in any medium, provided the original work is properly cited.

Review

Electromagnetic and Radon Earthquake Precursors

Dimitrios Nikolopoulos ^{1,*} , Demetrios Cantzos ¹ , Aftab Alam ² , Stavros Dimopoulos ¹ and Ermioni Petraki ¹ 

¹ University of West Attica, Petrou Ralli & Thivon 250, Aigaleo, GR-12244 Athens, Greece, dniko@uniwa.gr (D.N.); cantzos@uniwa.gr (D.C.); sdim@sdim.gr (S.D.); ermionipetraki@gmail.com (E.P.);

² Centre for Earthquake Studies, National Centre for Physics, Shahdra Valley Road, P.O. Box No. 2141, Islamabad 44000, Pakistan; aftabalamgeo@outlook.com (A.A.)

* Correspondence: Dimitrios Nikolopoulos dniko@uniwa.gr Tel.: +0030-210-5381338

Abstract: Earthquake forecasting is arguably one of the most challenging tasks in Earth sciences owing to the high complexity of the earthquake process. Over the past 40 years, there has been a plethora of work on finding credible, consistent and accurate earthquake precursors. This paper is a cumulative survey on earthquake precursor research, arranged into two broad categories: electromagnetic precursors and radon precursors. In the first category, methods related to measuring electromagnetic radiation in a wide frequency range, i.e., from a few Hz to several MHz, are presented. Precursors based on optical and radar imaging acquired by space borne sensors are also considered, in the broad sense, as electromagnetic. In the second category, concentration measurements of radon gas found in soil and air, or even in ground water after being dissolved, form the basis of radon activity precursors. Well-established mathematical techniques for analysing data derived from electromagnetic radiation and radon concentration measurements are also described with an emphasis on fractal methods. Finally, physical models of earthquake generation and propagation aiming at interpreting the foundation of the aforementioned seismic precursors, are investigated

Keywords: fractal; power-law; complexity; deterministic-fractal music

1. Introduction

Earthquakes, volcanic eruptions and tsunamis are all inevitable disastrous phenomena. Not only that they are unavoidable but the incredible difficulty in forecasting them renders these disasters even more hazardous and catastrophic. Finding an accurate seismic precursor is one of the greatest challenges for the scientific community worldwide. Seismic forecasting research dates back to more than fifty years. There is evidence that pre-seismic electromagnetic radiation or radon concentration observations can be utilised for forecasting, taking into account specific measurable features of the associated earthquake process. More specifically, if such an observation takes place near the geological rupture, some measurable precursory activity prior to the seismic event can be expected.

Reducing the uncertainty in the estimation of the occurrence time and location or even the size of a forthcoming massive seismic event is the main goal of earthquake forecasting [1]. Seismic forecasting usually falls into four categories [2]: long-term (10 years); intermediate-term (1 year); short-term (10^{-1} to 10^{-2} years); and immediate-term (10^{-3} years or less). Hayakawa and Hobara [3] classify earthquake forecasting into three categories: long-term (time-scale of 10 to 100 years); intermediate-term (time-scale of 1 to 10 years) and short-term. The separation into several stages is determined by the features of the processes that generate a massive earthquake and the needs for earthquake preparedness-which include a range of safety procedures for each level of forecast [1]. The reader should note, that there is no rarely any direct correlation between abnormalities in the measurements and earthquake occurrences, especially in short-term forecasting [4,5]. In seismic-prone countries, short-term earthquake pre-warning in a time window of weeks, days, or hours is deemed as most important, although being significantly more difficult than the long-term forecasting. The science of short-term earthquake forecasting is the study of short-term precursory activity occurring through systematic observations of physical quantities taking place near and before earthquake occurrences and can be further supported by serendipitous findings in observations not purposed for earthquake monitoring

but are nonetheless acquired near the earthquake location [6]. Abnormalities in electromagnetic fields, anomalous variations of radon concentration in soil, groundwater, surface water and atmosphere, erratic gas emissions, uneven surface distortions caused by pressure differentials, irregular adjustments to ionospheric parameters, ionospheric perturbations, anomalies detected in satellite devices and other remote sensory devices and excess Total Electron Content (TEC) are among these physical quantities [6].

Observations of pre-seismic electromagnetic disturbances (of the Radio Frequency-RF range) are one of the most promising tools for short-term earthquake forecasting. The related subject is termed seismo-electromagnetism [7]. As it has been shown by many studies (see e.g., the reviews [3,6,8–11] and references therein) pre-seismic electromagnetic emissions occur in a wide frequency range from frequencies well below 10 Hz (Ultra Low Frequencies-ULF), between some kHz range up to several MHz (altogether characterised hereafter as High Frequencies-HF) and between 100 MHz up to 300 MHz (Very High Frequencies-VHF). The research originated back in the 1970s where the first successful seismic forecast was reported for an earthquake of magnitude 2.6 occurring on August 3, 1973, near Blue Mountain Lake, New York [12]. Following this, the $M=7.4$ Heicheng China earthquake of February 4, 1975 was correctly anticipated by seismologists, boosting the prospect that credible earthquake forecasting may be feasible. This forecast led to the issuance of a warning within a period of 24 hours before the primary shock, perhaps avoiding more casualties than the 1328 deaths that the event resulted in. A major setback to the earthquake forecast endeavour was the 1976 $M=7.8$ Tangshan earthquake, which struck 18 months later and was not anticipated. The number of deaths caused by this earthquake reached the hundreds of thousands [6,8]. Seismologists's research has recently been focused on short-term forecast rather than long-term forecast [13]. The pre-seismic electromagnetic observations and abnormality recordings have been documented by several study teams throughout the globe as precursors of earthquakes. The EM variations are recorded by ground stations, remote sensory devices [14,15] and satellites [14,16].

Radon precursors of pre-seismic activity are also intriguing. Due to its importance, research on radon monitoring has become a rapidly growing topic in the search for premonitory signs before to earthquakes [5,6,8,17,17–25]. This is due to the fact that radon may travel great distances from the host rocks where it is created [26] and can be detected at very low levels [27]. Anomalous radon concentration variations in soil gas, groundwater and atmosphere may be observed prior to earthquakes [6,17,19,24,28,29]. Before earthquakes, anomalous radon fluctuations are addressed in soil gas, groundwater, atmosphere, and thermal spas [6,17,19,24,28,29]. The time-series features, such as the range, length, and number of radon anomalies, as well as the precursory time and epicentral distance, vary greatly [6,17,30,31]. However, the amounts of radon emissions are influenced by seasonal variations, rainfall and barometric pressure alterations [6,8,21,23,26,30,31] and for this reason, radon time-series are usually screened for atmospheric parameter influences [6,17,21–23]. The majority of the associations between radon and earthquakes are based on events of small and intermediate magnitudes. Large magnitudes earthquakes associations with radon observations also exist [5,32–36].

Ionospheric studies, satellite measurements and remote sensing devices have gained significant recent international interest in earthquake precursory investigations, after the realisation of the Lithosphere-Atmosphere-Ionosphere Coupling (LAIC) [37]. Due to the widespread availability of GPS data, many studies report GPS-based total electron content (TEC) data of the ionosphere, providing valuable information and convincing evidence [38–42]. Other researchers have studied the lower ionosphere extensively in relation to earthquakes by using different techniques to identify the precursory characteristics of earthquakes, as well as, the perturbation on the upper and lower regions [43–47].

Despite the massive scientific efforts, the causes of earthquake generation remain unknown. One important element is our inadequate understanding of the fracturing mechanisms of the crust [4,6,8,18–22,48–56]. Given that the fracture of heterogeneous materials is still not adequately described, despite a significant recent effort at the laboratory, theoretical, and numerical level [4], it is clear why the explanation of the genesis of earthquakes is still limited [4,6,18–22,48–56]. That explains why the related research is very significant, while the questions are far from being solved. Moreover, each earthquake

is unique and has a wide distribution. Thus, not only is the understanding of the complex related processes mandatory, but is also sedulous to identify credible earthquake precursors and meticulous work is needed for that [4]. This is complicated further when considering that the successful selection of an earthquake precursor might probably need an acceptable physical model to explain its existence [6]. Eftaxias et al. [4] stated that before the final catastrophe, several geological, geochemical, hydrological, and environmental parameters generate different features and scales that are associated and describe the earthquake's precursory processes.

2. Electromagnetic Precursors

2.1. ULF Emissions

In 1964, seismogenic electromagnetic emissions with frequencies lower than 10 Hz were first seen [57]. It has been found that variations in ground electric potential, ULF electromagnetic waves in the atmosphere, and other known phenomena occur prior to earthquakes [8–10,58–62]. Monitoring of ULF emissions directly recorded from the lithosphere is one of the several widely used seismo-electromagnetic methods. This is because ULF ($f=0.01\text{ Hz} - 10\text{ Hz}$) has great skin depth, low attenuation, less contamination and less penetration through the magnetosphere and ionosphere [63] and as a result, ULF waves can travel up to an observation point close to the Earth's surface with little attenuation [3]. Although most ULF precursors are electric, nowadays researchers study also magnetic ULF precursors [6,8,9]. It is noteworthy, nevertheless, that some contentious claims on ULF-range signals associated with earthquakes have also been reported[9].

The VAN method (from Varotsos, Alexopoulos, Nomicos), for ULF emissions has a long history of more than forty years [10,61,62]. The method introduced the concept of Seismic Electric Signals (SES). SES are ULF disturbances of frequencies $f < 1\text{ Hz}$. The most significant physical properties of SES is selectivity [8–10]. That reflects the fact that the SES choose preferable paths and, consequently, a ULF station is sensitive to SES from certain seismic areas only, namely from some specific focal areas. The map showing these potential areas is called selectivity map of a station and has to be determined in order that the station produces useful data. Due to selectivity, SES can be detected even from hundred kilometres away of the epicentre. By installing proper dipoles in a cross of 50 m, 100 m, 200 m and, preferably also, 1000 m, magnetotelluric variations are discriminated from anthropogenic disturbances. The VAN method has successfully predicted events within a precursory window of some days or weeks both in Greece [61,62] and Japan [3,10]. Nowadays the SES ULF signals (as other signals as well) are incorporated in the modern method of Natural Time (see **section 5**) which increases the successful forecasting of several earthquakes [e.g., 64, and references therein]. The discussion on the VAN method has divided the scientific community in those supporting it [10] it and those rejecting it [6].

The 1988 Spitak $M=6.9$ earthquake [65], the 1993 Guam $M=8.0$ earthquake [59], the 1996 Hetian $M=7.1$ event [66], and the 1997 Kagoshima $M=6.5$ earthquake [67] were all successfully predicted using ULF. Using the cumulative (daily sum) of the local energy of the earthquakes weighted by the squared distance from the measurement station method, which was suggested by Hattori et al. [68] and Hattori et al. [69], Han et al. [70] reported an increased probability of ULF magnetic anomalies 1-2 weeks before medium and strong shallow earthquakes, confirming previous findings published by Hattori et al. [69] and emphasizing that the perturbations are better associated with stronger and closer earthquakes. From data gathered from 17 stations in Japan, statistically significant diurnal geomagnetic anomalies were found two months before the $M_w=9.0$ 2011 Tohoku earthquake. Comparable estimations were published by Han et al. [71] and Xu et al. [72]. Prior to the catastrophic earthquakes that occurred in September 2015 at Coquimbo, Chile, September 2017 at Chiapas, Mexico, and September 2020 at Vrancea, Romania, ground-based stations recorded pre-seismic ULF anomalous geomagnetic disturbances [64,73–79]. Pre-seismic perturbations in the spectral density ratio between the horizontal and vertical ULF components are reported by Hirano and Hattori [80] and Ouyang

et al. [81]. ULF magnetic field emissions are continuously measured in Agra station in India with the help of 3-component search coil magnetometers with promising forecasting results [63]. Two large earthquakes of magnitudes $M=7.4$ and $M=6.8$ occurred in Pakistan have been successfully predicted within 16 days with fractal methods (see section 5). ULF geomagnetic data from the Panagjurishte and Surlari stations in Romania have been successfully utilised for the forecast of a $M_w=6.4$ earthquake occurred at the coastal zone of Albania on 26 November 2019 [79].

2.2. HF Emissions

In the range between a few kHz to several MHz , a number of HF emission disruptions have been reported prior to earthquakes. [4,23,34,35,82–87]. As stated by Hayakawa and Hobara [3], the two methods used to detect the seismic precursors are the direct measurement of the electromagnetic emissions radiated from the hypocentre of earthquakes in the lithosphere, or the indirect detection of propagation anomalous disturbances in the atmosphere and ionosphere caused by transmitter signals already in place. The identification of HF electromagnetic disturbances can aid in determining the source of seismic activity. According to Eftaxias et al. [4,82], the various frequencies of the HF electromagnetic precursors, in conjunction with the detected time lag between events and impending earthquakes, indicate distinct stages and mechanisms of the earthquake preparation processes. It is also believed that events at different scales and features will occur prior to an earthquake, as it is an abrupt mechanical breakdown in the heterogeneous earth's crust and thus, the multiplexed operations that occur may be the initial source of numerous electromagnetic precursors of the widespread earth's crust collapse [4,82,86]. These are transient phenomena and a way to examine them is by analysing the observed pre-seismic time series, however, including sequences of discrete, brief time periods. The goal is to identify a clear shift in dynamical properties as the catastrophic event approaches near. In order to develop a quantitative identification of electromagnetic precursors, several mathematical concepts are utilised (see section ??, so as to set the criteria, to isolate detected anomalous electromagnetic emissions versus the noisy abnormal statistical patterns [84–86,88–91].

Several publications [e.g., 4,34,82,83,86, and references therein] suggest that the high persistency and organisation in a launched electromagnetic anomaly points to the development of a positive feedback mechanism regulating the sudden fracto-electromagnetic process that occurs during earthquake preparation. There is increasing evidence that a feedback mechanism similar to this might be a sign of the earthquake fracture process. Naturally, there is no study that can establish the high precursory value of a particular abnormality on its own. There is still much to be done to comprehensively address the HF electromagnetic precursors. That is also valid for the ULF precursors also. Separating two events that happened at different times, like an earthquake and its potential HF electromagnetic precursor, is a challenging task. It is still to be determined if alternative methods may provide more data that would enable one to acknowledge the seismogenic source of the detected HF electromagnetic abnormalities and connect them to a pivotal phase of earthquake production.

Apart from persistency the strong anti-persistent properties of an electromagnetic time-series, as well as, the change between persistency and antipersistency are also evidence of an underlying non-linear feedback of the system initiating the crack-opening process and leads the system out of equilibrium ([34,35,92], and references therein). The reader should note that according to Eftaxias et al. [4], the anti-persistent behaviour is comparable to that of systems that experience a continuous phase transition at equilibrium. Stationary-like features possibly observed in anti-persistent sections of pre-seismic electromagnetic time series, might be attributed also to the heterogeneous part of the fracturing media. According to Contoyiannis et al. [88], Kaporis et al. [84,85] and Eftaxias et al. [89,90], the precursory electromagnetic antipersistent anomalies are associated to a continuous thermal phase transition with strong critical characteristics. Although finding an anomaly in HF pre-seismic series is necessary for the anticipation of a forthcoming event, it is far from considering it as a prerequisite for the occurrence of an event [4,92]. In actuality, there is no evidence connecting the discovery of several electromagnetic abnormalities with noticeably strong, crucial behaviour, to the occurrence

of significant earthquakes. Notably, it is important to rule out any potential relationship of these anomalies with magnetic storms, artificial electromagnetic sources, or, solar flares [4], with the note that the latter may trigger seismicity and have impact to the earthquake preparation zone [93]. In relation, Anagnostopoulos et al. [94] consider that the sun is an agent provoking seismic activity through coronal holes driven by high speed solar wind streams.

2.2.1. VHF Emissions

VHF have been also employed in the search of electromagnetic earthquake precursors. According to Pullinets [95], one of the two authors of the LAIC model [37], in actuality, the LAIC is a complex system made up of subsystem interactions and a synergy of several processes, one of which is the VHF electromagnetic emission frequency band, which further functions by altering the characteristics of the atmosphere and ionosphere. Although some scientists dispute with the precursory usability of VHF emissions (e.g., [8], and references therein), the scientific interest is stimulated in the recent years on this subject. For example, Sorokin et al. [96] report a full-fledged theoretical physical model, according to which, the over-horizon propagation of pulsed VHF radiation, can be explained. As also, the origin of such seismic related phenomena in link to the generation in the troposphere, the thermal effects and associated IR emissions, as well as, the modification of plasma distribution in the *D*, *E* and *F* layers of the ionosphere. Ouzunov et al. [97] report atmospheric variations in the intensity of broadband wireless signal propagation correlated with pre-earthquake processes. Since 2012, these authors have continued to conduct ground observations in Bulgaria in the VHF band between 1.8 GHz and 3.5 GHz, discovering phenomena related to a natural amplification of the signal's strength days or hours before the seismic occurrences, even distant from the observation zones, such as the $M=5.6$ earthquake of May 22, 2012, in Bulgaria, $M=5.1$ earthquake of August 12, 2018, in Albania, the $M=4.1$ earthquake of August 2, 2018, in Southern Bulgaria and the $M=5.5$ earthquake of October 28, 2018, in Romania. A VHF early warning system is utilised among other systems in Mexico [98]. Moriya et al. [99], on the basis of a designed a data-collection system, report several anomalous VHF-band radio-wave propagation prior to earthquakes, with most significant, the Tokachi-oki earthquake ($M_j=8.0$, M_j , M_j a magnitude defined by the Japan Meteorological Agency) on 2003 September 26 and the southern Rumoi sub-prefecture earthquake ($M_j=6.1$) on 2004 December 14. Devi et al. [100] states that the VHF emissions indicate unusual atmospheric parameters brought on by earthquake precursor processes, which may allow for the reception of VHF communications at distances more than 1,000 km. According to the authors, the lower VHF TV transmissions of less than 70 MHz are linked to modifications in the tropospheric environment and the ionospheric mode of propagation. Regarding VHF or higher frequencies that are pertinent to observations in radio astronomy. According to Erickson [101], anthropogenic electromagnetic emissions are primarily caused by mobile communications, car ignition systems, industrial equipment, and radio and television broadcasting stations. Eftaxias et al. [102] report VHF disturbances prior to earthquakes in Greece showing that the related features are possibly correlated with the fault model characteristics of the associated earthquake and the degree of geotectonic heterogeneity within the focal zone.

2.3. Remote Sensing and Satellite Techniques

The application of space-borne remote sensing has grown in popularity and effectiveness within the field of natural disasters [103]. Improved quality data with repeated spatio-temporal coverage covering large areas in rough geomorphological and geological conditions can be obtained through the development of geospatial technologies and advanced data processing [104–106]. The post-disaster visualisation of remote sensing images helps in knowledge production, emergency intervention thinking and decision-making during the earthquakes [107]. In fact, the seismo-electromagnetic research has entered a new phase with the development of the remote sensing tools. This is because they make it possible to monitor a number of locations throughout the globe, including various seismic occurrences taking place in tectonic systems with differing geomagnetic conditions. That is essential to

the related research. For the remote sensing data to yield reliable findings, a worldwide coverage with sufficient spatial and temporal resolution is needed [8].

The remote sensing of the co-seismic effects of earthquakes is of importance as well. Co-seismic effects occur as around 100 m-long earth cracks, which are followed by landslides, lateral spreading and changes to urban and suburban areas. For instance, landslides and substantial lateral spreading were noted following the earthquakes in Kashmir in 2005 and Mirpur in 2019 [108,109]. Human casualties from earthquakes are brought on by landslides, which also significantly alter agriculture and the food supply chain. These overall structural, stratigraphic and hydrogeological seismically-generated side-effects are significant features in remote sensing and satellite studies. As another example, the Landsat satellite imagery has been used to study the dynamic relationship between observed seismicity and lineament density[110]. Ground-based remote sensing techniques are efficient non-destructive geophysical methods that provide high-resolution subsurface images to detect several co-seismic features. Remote sensing data from a number of satellites and sensors are also useful tools for such hazard co-seismic mapping.

The Synthetic Aperture Radar (SAR) remote sensing techniques are among the best candidates for mapping co-seismic changes Interferometric SAR (InSAR) is one of the most powerful remote sensing techniques of the SAR family, that has been used to detect several surface deformations over large areas with high accuracy [111]. InSAR-based remote sensing methods allow low-speed surface deformations to be detected over vast areas with centimeter to millimeter precision [112]. The permanent Scatterers InSAR method is also accepted as a robust technique for mapping co-seismic deformation and in-field conditions, as well as, movements of urban infrastructures [113,114]. Space-borne remote sensing techniques are less effective towards this directions because they cannot provide complete information on the near-surface features produced as a consequence of an earthquake with the potential to damage the built environment.

Like the non-destructive near-surface geophysical remote sensing methods, the ground penetrating radar (GPR) method has been applied to shallow subsurface seismic investigations due to its high-resolution, time and cost-effective nature [115–117]. GPR has gained popularity in studies related to the detection of faults and fracture networks [118], slope instabilities [117] and landslides [119]. The GPR is one of the reliably accurate mapping tools to study a single site and imaging of a localised subsurface deformation but difficult to perform such surveys over an extensive earthquake Karst depressions-landslide affected area to detect the near-surface target features. Among the aforementioned geohazards, few studies focusing on co-seismic liquefaction and related ground failure have been conducted using field GPR measurements [120,121].

2.3.1. TEC

Total Electron Content, or TEC, is the electron density of a 1 m² cylinder that is vertically stacked from a ground point to the ionosphere [122,123]. One TECU is the TEC measurement unit and equals 10¹⁶ electrons per square meter vertically arranged up to the ionosphere. By definition, TEC is associated with the LAIC model. GPS receivers and ionosondes are used to continuously monitor TEC at various locations across the world [123]. The corresponding data is accessible through a number of repositories and URLs [123–127] via the Ionosphere Exchange (IONEX) data file structure [128].

To investigate seismically generated TEC fluctuations in the ionosphere, researchers have used a variety of schemes and approaches [39,123,129–134]. There has been much discussion about anomalous variations in the ionospheric F_2 peak electron density $N_m F_2$ (plasma frequency $f_o F_2$), which are recorded by ionosondes and TEC, which, in turn, are determined by ground-based GPS receivers and appear prior to earthquakes [39]. Based on 184 $M \geq 5.0$ earthquakes which occurred in Taiwan over a 6-year period between 1994 and 1999, Liu et al. [39] conducted a statistical investigation that showed anomalous decreases in the ionospheric $N_m F_2$ in the afternoon within 1-5 days prior to the earthquakes and pronounced reductions in the ionospheric GPS TEC in the afternoon and late afternoon periods within 5 days prior to 20 $M \geq 6.0$ earthquakes in Taiwan.

According to Liu et al. [130], while pre-earthquake ionospheric anomalies may occur almost at any local time, TEC over a possible epicentre region typically decreases or increases significantly in the afternoon and/or, evening periods, one to six days prior to the occurrence of an earthquake. According to these authors, during the period of earthquake preparation, the generated seismoelectric fields may permeate the ionosphere and perturb TEC alterations within it, hence modifying the seismo-electromagnetic environments surrounding the epicentre. A few days prior to the May 12, 2008 $M_w=7.9$ Wenchuan earthquake, Zhao et al. [135], Liu et al. [39], and Pulinets and Ouzounov [37] report that ionospheric GPS TEC enhancement and, or, reduction anomalies simultaneously appear above the epicentre and its magnetic conjugate point.

Increased ionosphere observations from space and on Earth clearly show that there is a coupling mechanism between lithosphere-based seismic activity and ionosphere-based deviations or disturbances in electron concentrations, particularly prior to major earthquakes [122,123,125]. The measurements include variability in the critical frequency of the F_2 layer, f_oF_2 and TEC [125,136]. Compared to costly and sparse f_oF_2 observations using earth- or space-based ionosondes, TEC measurements are more readily acquired with the use of global GPS TEC [125]. The efficiency of the impact of earthquakes on the ionosphere is growing with earthquake magnitude and depth representing relative density TEC anomalies within area of 1000 km radius around the earthquake's hypocentre [126]. Gulaeva and Arikan [126] suggest that the positive TEC storm anomalies are twice as much as those of non-storm values and that this observation supports dominant post-earthquake TEC enhancement with ionosphere peak decreasing during 12 h for daytime but growing by night-time during 6 h after the earthquake and followed by gradual recovery afterwards.

According to Sorokin et al. [96], there are two possible causes of the TEC ionospheric anomalies: variations brought on by acoustic gravity waves and variations created by electric fields. Variations in the density of TEC are caused by a variety of natural events, including dust storms, thunderstorms, solar radiation, volcanic activity, radioactive gases, and thunderstorms [137–139]. For instance, TEC increased during the 2014-2015 high solar radiation cycle, which was brought on by high-energy solar particles interacting with the earth's ionosphere resulted in TEC shifting [122]. Therefore all these parameters should be taken into account when studying TEC ionospheric variations.

3. Radon Precursors

3.1. Radon Properties

Radon (^{222}Rn) is a natural radioactive noble gas. It is produced when radium (^{226}Ra) decays. According to Nazaroff and Nero [26] there are thirty-nine known isotopes of radon, ranging from ^{193}Rn to ^{231}Rn . Radon has a half-life of 3.823 days and is the most stable isotope. ^{220}Rn , or else, thoron, has a half-life of 54.5 seconds, ^{220}Rn . Due to its short half-life, thoron decays rapidly and because of this it is often detected at low concentrations. That depends however on the concentration of its parent nucleus (^{224}Ra), especially in comparison to that of ^{226}Ra . Radon is primarily responsible for the radioactivity present in the atmosphere at sea level [140].

Radon emissions mostly originate from soil [26]. About 10% of the radon that is diluted in soil gets released into the atmosphere [140]. In addition to soil, radon may be found in surface and underground waters, as well as fragmented rock [140,141]. While all radon atoms produced are diluted in fluids, only a portion of radon emerges from porous media and fractured rock, enters the volume of the pores and dissolves within the pore's fluid [141]. Once there, either convection or molecular diffusion advection can cause a macroscopic transport [26]. Interconnected pores and water aquifers allow this movement to appear [141]. Radon dissolves into the water present in the pores of soil and rock and is carried away by it [26]. The migration of radon in soil and fragmented rock is implemented by all fluids present there, enclosed air included [17,26]. The most crucial elements for these processes are the pressure differentials, the temperature gradients, and the permeability of soil [6].

Radon is a significant radiological risk factor since it contributes significantly to the effective dose equivalent and makes up over half of the population's exposure to natural sources and the leading natural cause of lung cancer [142–144]. Due to this, radon is a subject of extensive research worldwide [142–151]. In addition to the above health risks, radon offers several beneficial uses in a variety of applications. In meteorology, the amount of uranium is calculated from the changes of radon's emission in soil and the obtained information, is then utilized to monitor air masses. When assessing how accurate chemical transport models are in estimating greenhouse gas emissions, radon can be a helpful tracer for understanding how the atmosphere functions [152].

Radon is also among the various hydrological, geochemical, geological and environmental species that have been employed in hydrological studies and for faults identification [153–155]. The shift in concentrations of CO₂ [156,157] near faults and the anomalous variations in groundwater levels [158], have been employed as well because the corresponding concentration variations, reflect the water-rock interactions [159] and the pathways generated by active faults [156]. Due to these properties, several hydro-geological species that have been utilised as tracers of pre-seismic activity [6,8]. Especially radon has been studied as well for co-seismic effects and tidal strain [160]. Radon's half-life in association with its inert nature, provides it with the ability to travel long distances without significant loss [27]. Because of this, radon has been extensively used to study tectonic activity [6,8,17,161,162]. Under this perspective, radon is the best among the various hydro-geological species for earthquake forecast.

Radon combines hydrological, geological and environmental properties. Hydrologically, it dilutes to water [26] molecules and water aquifers. It is present in surface and, most importantly, underground waters [140,141]. Geologically, it is easily transferred within soil and rock reaching areas away [5]. Environmentally, it is naturally emitted and present in aspects of the environment, i.e., atmosphere, earth, water. It is naturally radioactive and easily detected. All these combination properties have made radon one of the best precursors of seismic activity and the one with the longest history in earthquake related studies [8,17,86,161,162].

3.2. Pre-Seismic Radon Anomalies

Abnormal radon changes before earthquakes have been found in groundwater, soil gas, atmosphere, and thermal spas (e.g., [6,8,17,29,52,148,161,161,161–163,163,164,164–166,166,167,167–174]) and, recently, between radon TEC (please see Section 2.3.1) [132–134,175]. There are considerable variations in the relationships between magnitude, precursory time and epicentral distance in connection with the range and number of radon anomalies and other features of the associated time series (e.g., [6,8,17,30,31]). For instance, the epicentral distances of earthquakes identified with the aid of radon, vary from 10 km to 100 km, whereas the recorded precursory durations span from three months to a few days before the earthquake's occurrence. Comparable ranges have also been published by Cicerone et al. [6], Ghosh et al. [17], Petraki et al. [162], Conti et al. [8] and Huang et al. [161]. Several precursory signals have been obtained with passive techniques (no electricity needed), which offer rough time-series estimations, since these methods integrate the radon concentrations over extended periods of time (of at least >1-4 weeks), necessitated for the measurement. This roughness poses significant bias to the precursory estimations. Nowadays, radon precursory signals are monitored with active techniques (require electricity). The active techniques are implemented with portable monitors which allow for high rates of radon monitoring (typically between 1 min⁻¹ and 1 hour⁻¹). As a consequence, these techniques offer detailed signals of radon and fine estimations (e.g., [5,6,8,17,161,162]). It is crucial to mention that additional factors influence the estimates of radon and earthquakes. For instance, seasonal fluctuations, geological and geophysical conditions, rainfall, and changes in barometric pressure all have an impact on radon concentrations levels [6,21–23,26,30,31,140,161]. Because of this, the associated time series data are typically shown alongside the precursory signals of radon. Most of the correlations between radon and earthquakes are based on small-to intermediate-sized magnitudes. This further limits the calculations since, as of right now, it appears that neither for

mild earthquakes nor even for powerful earthquakes is there a universal model that can be used as a hallmark of a particular impending seismic event ([4,82,83,176], and references therein).

3.2.1. Soil

The release of radon from soil is important for research on earthquake forecasting. Because of this, one of the key elements in forecasting strong earthquakes, is the monitoring of radon emanations and this is done by various research groups [5,19,24,25,27,31,36,48,51,52,52,54,148,163,164,164–168,168–175,177–182]. The stability of the emission response of radon to seismic occurrences at the monitoring station, determines how successful these investigations are. Radon concentration in soil depends on a number of parameters and is, hence, varies between different natural environments. The objectives of the detection of radon pre-earthquake precursors, are guided by the certain prospects of each region [49,50,162,183]. Traditionally, because of well investigated relationships between radon and environmental parameters, the deviations are believed to be indicative of changes brought by tectonic force during the earthquake preparation. In general, twice the standard deviation or more from the average soil radon concentration at a site of observation, is thought to reflect appreciable anomalies. The radon anomalies are attributed to earthquake-related stress-strain changes underneath the earth's crust, but this has been a subject of significant argumentation [5,8].

Two approaches have been taken to the study of soil radon as an earthquake precursor: one involves doing simulation experiments in the lab and the other, involves monitoring the concentration of radon in soil gas at a specific place, over an extended period of time, in comparison to unusual emission changes in respect to seismic occurrences. In order to understand the gas dynamics underlying the ascent of radon from deep below the earth's crust to the surface, a number of in-situ and laboratory experiments, as well as, models have been suggested [6,8,17,162].

Based on observations and conclusions drawn from all of the aforementioned worldwide studies, it has been determined that some radon gas, which originates from the decay of radium in rocks inside the crust, stays in the crustal matrix, while the remainder migrates away through interconnected pores and aquifers using diffusion, fluid flow, and alpha recoil. Changes in the strain field are caused by the accumulation of tectonic stress before to an earthquake. According to Fleischer and Mogro-Campero [184], the deformation of rock mass under stress creates new channels that allow gasses from deep earth to ascend to the surface.

3.2.2. Groundwater

Although the idea that radon anomalies in groundwater may be connected to earthquakes was initially put up in 1927, the Great Tashkent earthquake of 1966 produced the first indication of an abnormally high radon concentration in groundwater [185]. Subsequently, a number of groups employed the concentration of radon in groundwater to study earthquakes [20,28,30,163,186–201]. Groundwater radon concentrations frequently increase before earthquakes (e.g., [36,179,180,194,202]). A few times, before an earthquake, the amount of radon in groundwater's has decreased [20,187,188,194]. Significant earthquakes may be related to groundwater radon's peculiar behaviour as it offers information about subsurface dynamics [180], particularly in areas where high-stress buildup occurs in the crust [203]. The processes driving seismic activity can be better understood by examining the links between seismicity and geochemical signal variability [180].

The route that groundwater follows underground, or the kinds of rocks and soil it encounters, determines the amount of radon that is present in the groundwater [204] or escapes from it [205]. The measurement of the underground water baseline is crucial because radon gas permeates the water from these rocks and soils and alters the amount of radon in these waters. Baseline radon concentrations in groundwater vary greatly. According to Kandari et al. [206], radon concentrations in 15 water samples from the Dehradun region, which is close to an active fault, range from 1.70 BqL^{-1} to 7.57 BqL^{-1} . In southern Catalonia, 15 hot springs had groundwater radon levels ranging from 1.4 BqL^{-1} to 105 BqL^{-1} [207]. Using an AlphaGUARD system, Spanish researchers measured 28 groundwater samples

collected from northeastern Gran Canaria (Canary Islands, Spain). They found that the highest and lowest levels of dissolved radon concentration were 76.9 BqL^{-1} and 0.3 BqL^{-1} , respectively [208]. Range values are provided globally [142–144,209]. Significantly more radon is found in groundwater in thermal spas [140,210–212].

The seasonal fluctuation in groundwater radon concentrations may be attributed to temperature, precipitation, and other climatic conditions, but its anomalies may also be linked to shifts in tectonic stress [200,213]. While it is now well accepted that radon anomalies may be associated with earthquakes, anomalies are typically exceedingly hard to locate since variations in radon concentration frequently exhibit the features of nonlinear dynamic fluctuations. Thus, the development of efficient identification techniques is necessary. To some extent, the conventional statistical techniques are erroneous and subjective. A few data mining techniques, such artificial neural networks and machine learning, have had some success recently [164,200,201,213].

3.2.3. Atmosphere

The primary source of atmospheric radon concentration is the exhalation from the earth and with a lesser extent the escape from surface and subsurface water [26]. Numerous processes are involved and meteorological elements have a significant impact on them [144]. Therefore, detecting anomalies in air radon in relation to earthquakes, is significantly more challenging than detecting them in groundwater or soil radon. Prior studies computed anomalies in atmospheric radon concentrations by establishing a threshold level for the anomalies based on a normal variation period and removing the seasonal component anticipated from a sinusoidal model [167,214]. The results of these conventional methods depend on how the seasonal component is determined because the assessment is based on departures from the assumed sinusoidal model and the selected normal period of average fluctuations [215].

Japan is the primary source of studies on earthquake forecasting using atmospheric radon. Iwatata et al. [167] reported that anomalies in the atmospheric radon concentration have been linked to the moment releases of large earthquakes based on ten years of continuous observation of the concentration over north-eastern Japan and Hokkaido. Yasuoka and Shinogi [216], reported that two months before to the main shock of the 1995 Kobe earthquake ($M_w=6.9$; January 17, 1995, N34.6°, E135.0°), an increase in atmospheric radon concentration was noticed at Kobe Pharmaceutical University. Goto et al. [217] reported anomalous atmospheric radon concentrations associated with a shallow inland earthquake ($M_j=5.5$, depth=7 km; 5 July 2011, N 34.0°, E 135.2°) in northern Wakayama. Yasuoka et al. [29] reported that the residual values for each day could be fitted very well to a log-periodic oscillation model by applying the exponential smoothing method to the fluctuations of the residual values. The authors stated that the residual values stopped increasing on December 31, 1994, and, they concluded that this corresponded to the critical point of best fit model. These authors contended that rather than main stresses causing the Kobe earthquake directly, local stresses are responsible for the unusual ^{222}Rn fluctuation as well. Using the irreversible thermodynamic model, Kawada et al. [218] proposed that the preseismic radon shift was caused by a little change in crustal strain. Furthermore, a quantitative study by Omori et al. [215], revealed that the unusually high radon concentration (about 10 Bqm^{-3}) before the Kobe earthquake increased air conductivity and was sufficient to produce an ionospheric disturbances. Yasuoka et al. [219] claimed that further mechanically-induced precursors were seen prior to the Kobe earthquake. Igarashi et al. [190], for instance, described such precursory variations in groundwater radon concentration. Tsunogai and Wakita [220] documented further pre-seismic variations in crustal strain, groundwater discharge rate, and chloride ion content in groundwater. Because of the mechanical behaviour of the crust, these pre-seismic fluctuations should be related to one another [29,190,218]. The fact that the temporal change in atmospheric radon concentration has not been compared with that in other preseismic events was noted by Igarashi et al. [190]. The linkage between preseismic fluctuations in the subsurface, atmosphere, and ionosphere could have been substantially verified if radon activity was clearly linked to the earthquake preparation process [190]. Additionally, current research supports the link between atmospheric radon and the Kobe earthquake [217,221].

4. Models

4.1. Electromagnetic Precursors Models

4.1.1. Models for the ULF Precursors

Three are the main models that have been proposed for the interpretation of the magnetic component of the pre-seismic ULF disturbances:

1. Magneto-hydrodynamic model [222]. According to this model, an electrically conducting fluid flowing through a magnetic field causes an additional induced field to be created. If B is the magnetic field, the Maxwell's equations indicate that the induced magnetic field B_i can be given by the equation $B_i = R_m \cdot B$, where R_m is the magnetic Reynolds number, comparable to the hydrodynamic Reynolds number, the latter determining the relative significance of the convective and diffusive components.
2. Piezomagnetic model [223]. This model states that an applied stress causes ferromagnetic rocks to shift in magnetisation, which in turn, induces a secondary magnetic field.
3. Electrokinetic model [224]. This model suggests that electric currents flowing in the earth due to electrified interfaces present at solid-liquid boundaries, induce magnetic fields.

Varotsos et al. [225] established a theory about the current produced by charged distortions and currents induced by piezo-electric effects. The electrokinetic theory serves as the foundation for this theory. In water-saturated media with fluid-filled channels, electrokinetic currents can be found [226,227]. In order to model the parameters of these electrokinetic currents, Surkov et al. [228] assumed that an earthquake hypocentre is surrounded by water-saturated porous rocks with fluid-filled pore channels where cations from the fluid are adsorbed by the walls of pores and cracks in the solid material. According to this author, the fluid moving along the channel, carries anions, and, as a consequence, produces an extrinsic electric current between the fluid and the surrounding walls.

When an earthquake is prepared, the seismic hypocentre within the earth's crust, is surrounded by cracks and fractured material, where new fractures are continuously produced forming the, so called, fracture zone. The fracture zone can range in size from a few hundred metres to several kilometres. Feder [229] postulated that there is a fractal structure present in the pore's space within the fracture zone. Newly developed cracks are sealed off as soon as they arise under reduced pressure, as a result of the pressure release that is caused by cracking. This, in turn, allows water from the uncracked outside zone, to enter as soon as a network of linked channels, or, fractal clusters is formed. This can be seen, alternatively, as a grid of new cracks that are closed as the water sinks from the nearby locations of greater pressure. According to Surkov et al. [228] during the cluster formation the porosity and permeability of rocks decrease from the centre of the fracture zone towards the perimeter. An interior area manages to surpass the percolation threshold and due to this, the permeability outside the fracture zone tends to zero. In actuality, there is a limited permeability since crustal rocks have a large variety of inter-connectible small cracks. Furthermore, the rock's conductivity together with the surface and bulk conductivities of the tiny fluid-filled cracks contribute to a non-zero conductivity of the surrounding space. However, according to Surkov et al. [228], the conductivity beyond the fracture zone is minimal. This indicates that, because of the recently formed fluid-filled cracks, the conductivity's value is more closely tied to the conductivity of the percolation threshold. It is important to note that only the percolation hypothesis can adequately explain the range of fracture diameters. Surkov et al. [228] limited the study by using a basic percolation hypothesis that ignored the crack-channel size distribution. The correlation length ξ where $\xi = 1 |p - p_c|^{-\nu}$ with p being the probability that a channel can conduct the fluid, p_c is the critical probability in the percolation threshold and $\nu=0.88$.

The three main ULF models have described successfully major earthquakes identified with ULF data: The $M_w=9.0$ earthquake at Tohoku, Japan; The $M_w=8.3$ earthquake at Coquimbo, Chile; The

$M_w=8.1$ earthquake at Chiapas, Mexico and the Vrancea seismicity, at Romania [29,49,168,187,190,191,216,219,221,230].

4.1.2. Models for the HF Precursors

The behaviour of a stressed rock is comparable to that of an electromagnetically strained rock [176]. The crack propagation is the basic process responsible for the material's failure [83]. The release of photons, electrons, ions, and neutral particles is observed when fracture, deformation, wearing, and peeling cause new surface characteristics to appear in various materials [4,82,83,89,91]. The total of these emissions is referred to as fracto-emissions [83]. The significant charge separation brought on by the rupture of the inter-atomic ionic bonds is the source of the electric charge between the micro-crack faces. An electric dipole or a more intricate system is created by the electric charges on the surfaces of freshly developed micro-cracks. It has been shown that a dynamical instability controlling the oscillations in the velocity and shape of a crack on the fracture surface controls the crack's mobility [83].

According to experimental data, micro-fracturing events repeat and get more irritating until a multi-crack state occurs, indicating that local branching is the instability mechanism at work. It's important to note that laboratory research has identified strong fracto-emissions during unstable crack propagation [22,23,34,83,231]. Because of the intense wall vibrations of the cracks during the micro-branching instability stage, the cracked material functions as an efficient emitter. As a result, opening of cracks in a material can be seen as a potential precursor of general fracture because electromagnetic emissions occur in a wide frequency range from *kHz* to *MHz* when the material is stretched. These electromagnetic precursor are detected in-field during measurement and at laboratories under controlled conditions [4,34,82,89,90,176]. Owing to the previously indicated viewpoint, the main technique for forecasting earthquakes is to record the electromagnetic emissions from potential micro-fractures in the focal region prior to the final break-up [4].

As stated in by several papers (e.g., [82,88,91,176], and references therein), a "symmetry breaking" is linked to a thermal second-order phase transition. For non-equilibrium irreversible processes, the evolution of the "symmetry breaking" with time has been reported in order to obtain an understanding of the catastrophic nature of the fracture events. The investigation revealed that the system's balance is progressively lost. This allowed for the estimation of the duration beyond which the process responsible for the pre-seismic electromagnetic emissions could continue as a non-equilibrium instability.

The analysis has indicated three key periods (i) the crucial epoch, that also known as the critical window, in which the short-range correlations transit to long-range ones (ii) the "symmetry breaking" epoch; and (iii) the integration of the "symmetry breaking." It is widely acknowledged that a notable rise in localisation and directionality occurs at the terminal phase of the earthquake preparedness procedure. Therefore, it's critical to identify distinctive epochs in the precursory electromagnetic activity progression and to connect these to the corresponding final phases of the earthquake preparation process.

Tracing "symmetry-breaking" could indicate that the focal area's heterogeneous component, which encircles the fault plane's strong asperities'backbone, has reached the point of microfracture propagation completion. At this point, the rupture has become blocked at the boundary of the strong asperities'backbone. Asperities are already under "siege" [83].

4.2. Radon Precursors Models

Scholz et al. [232] presented the Dilatancy-Diffusion model, which connects anomalous radon changes to the mechanical crack development rate in the volume of a dilatancy, so as to simulate the underlying dynamics of radon prior to earthquakes. This model states that the first medium is a porous, fractured, submerged rock. Favourably placed fractures open when tectonic forces grow because the cracks expand and disengage close to the pores. As a result, the preparation zone's overall pore pressure decreases, allowing water from the surrounding medium to enter the zone. Radon

emission may fluctuate suddenly as a result of the pore pressure returning and the number of cracks growing.

The crack-avalanche model [177,233] states that the growing of tectonic stress forms a fractured focal rock zone. This zone gradually changes in volume and form over time. The slow crack propagation, which is controlled by stress corrosion in the rock matrix saturated by groundwater, may be linked to the unusual behaviour of radon concentration, according to the hypothesis of stress corrosion [234].

The LAIC model [37,95] describes also radon's stress accumulation in the ground. This is attributed to the relative movement of tectonic blocks, which, in turn, lead to the formation of micro-cracks, cracks, and fractures. Radon gas released from micro-fractures combines with water and travels via various media to the earth. Water and carrier gases are often responsible for the transportation of radon from the Earth's deep strata to the surface [235].

Nikolopoulos et al. [5,21,32,35,236], Petraki et al. [22,23], Alam et al. [36,179,180,202] and Petraki [86] proposed the asperity model [83] (please see **Section 4.1.2**) to explain radon emanation during preparation of earthquakes. Pre-seismic radon anomalies are attributed to variations of fractional Brownian (fBm) profile movements. In the views described in **section 4.1.2**, the focal area consists of a backbone of strong and large asperities that sustain the system and a strongly heterogeneous medium which surrounds it. The fracture of the heterogeneous system in the focal area obstructs the backbone of asperities. As the fracture begins critical persistent, strong anti-persistent and interchanged persistent, antipersistent radon anomalies occur. This has been associated with several earthquakes in Greece and China.

Other aspects have been expressed by other investigators. For example, Talwani et al. [237] reported that the anomalous behaviour of radon gas could be because of the opening of pore's spaces during rock fracturing as a result of seismic events. Explosion tests have been performed to identify the relationship between the dynamic loading effect and the observed concentrations of radon [18]. The experimental results revealed that the increase in radon values is a consequence of seismic waves applied to the rock. According to other investigators [238–240] crustal activities have been identified as one of the reasons for radon emission.

5. Analysis Methods

Several investigations on earthquake forecast have been based on visual observations [6,11,162]. Despite providing some indications, the visual observations are not enough to support the pre-seismic nature of the derived signals (e.g., [5,86], and references therein). Due to this, the analysis nowadays rely on the physical background of the related earthquake processes. The analysis' mainstream comprises the fractal methods [4,34–36,55,60,84,85,89,90,102,148,156,179,231,236,241–257], methods based on the theory of information and entropy [82,88,91,176], symbolic dynamics [21,23,86,258–262] and natural time methods [64,263–267]. Within the above framework, several metrics have been utilised as adequate for the related analysis. These metrics comprise exponents from the spectral power law (e.g., [34,84,256], Detrended Fluctuation Analysis (DFA) (e.g., [4,236]), Rescaled-Range Analysis (R/S) (e.g., [268]), Multifractal Detrended Fluctuation Analysis (MFDFA) (e.g., [36,55]), fractal dimensions from Katz's, Sevcik's and Higuchi's methods [34,148], Hurst exponents and entropy values from (i) entropy per letter; (ii) conditional entropy; (iii) entropy of the source; (iv) t-entropy; (v) Tsallis entropy; (vi) perturbation entropy; (vii) normalised Tsallis entropy and parameters for critical phenomena (e.g., [4,82]).

Spectral power-law analysis and Hurst exponent analysis have been utilised in all ULF, HF and radon precursors. DFA, fractal dimensions from the Katz's, Sevcik's and Higuchi's methods and R/S analysis have been used with success both for HF and radon precursors. Symbolic dynamics with entropy per letter, Tsallis entropy and normalised Tsallis entropy have been also employed for both HF and radon precursors but to a lesser degree. Natural time has been employed mainly in ULF signals. The remaining techniques and metrics have been used mainly for HF precursors. Multifractal

Detrended Fluctuation Analysis (MFDFA) has been employed in all types of precursors [55,180,242,257,269–271] but will not be presented here due to its complicated interpretation [272].

Due to their importance in both electromagnetic and radon precursors, the important properties of fractal behaviour, long-memory and Hurst exponent analysis are given in the following sub-sections, firstly. DFA is presented thereafter because it is a robust method that has been used in both LF, HF and radon precursors. The fractal dimension calculations through the Katz's, Sevcik's and Higuchi's methods are given next because they have been utilised both in HF electromagnetic and radon precursors and, finally, the R/S analysis because it is the main direct method to calculate Hurst exponents and has been employed both in HF electromagnetic and radon precursors.

5.1. Important Properties: Fractal Behaviour, Long-Memory and Hurst Exponents

5.1.1. Fractal Behaviour

Many physical systems in nature display fractal behaviour, which is reflected when these systems are stretched, translated, or rotated in space. Based on their mathematical characteristics, these systems are classified as either self-similar or self-affine. These systems are fractals because each component of the system is a large-scale imitation or representation of the system as a whole due to the self-affinity and self-similarity that define all system components. This characteristic allows for the investigation of fractal systems through part-by-part analysis. System fractals can exhibit self-similarity or self-affinity. While self-affine systems behave almost in this way, self-similar systems have exact inter-parts representations.

The system's complexity [273], which indicates whether the system is driven by linear mechanisms and order [274,275], is also connected with the scaling and fractal behaviour. The correlations are strong because a system's complex behavior may be predicted by its fractal behaviour and vice versa.

5.1.2. Long-Memory

The long-memory [273,276,277] of a system can show if the system has long-range interactions or is random. In specific it may reveal if a geo-system has strong persistent and antipersistent behaviour or if the long-range interactions are rather loose. If system exhibits long-memory, then the past, present and future states of the system are linked together in a manner that the presence of the system is not only derived from its past (Markovian behaviour) but defines also its future (non-Markovian behaviour) [82,176]. This behaviour is characteristically seen when the fracture of the earth's crust yield to the inevitable general breakdown during the unstoppable approaching of an ensuing earthquake [4,83,89,90]. Precisely there the past determines the presence and also the inevitable future breakdown of the system.

5.1.3. Hurst Exponent

Because it may depict enduring connections in space or time, the Hurst exponent (H) provides a straightforward technique for assessing a system's long memory [278,279]. Time-evolving fractal events may be identified with the Hurst exponent and the corresponding time series' roughness can be evaluated [280]. Important details about the time series are revealed by the Hurst exponent's value [242,278,279,281,282]:

- (i) The series has positive long-range autocorrelation if $0.5 < H \leq 1$. A series' high value is followed by another high value and vice versa. High Hurst exponents suggest persistent interactions that are anticipated to remain until the series' remote future;
- (ii) Low values of the time series follow high values if $0 \leq H < 0.5$, and vice versa. In the future of the time series, there is a persistent transition between low and high values for low H values (anti-persistence);
- (iii) If $H = 0.5$ the time series completely uncorrelated, i.e., the related processes are random.

5.2. Significant Analysis Methods for Electromagnetic and Radon Precursors

5.2.1. Power-Law Analysis

In the event that a temporal fractal is present in the time series, the power spectral density, $S(f)$, will exhibit a power-law behaviour:

$$S(f) = a \cdot f^{-\beta} \quad (1)$$

In equation (1), a represents the spectral density amplification, f denotes a transform's frequency and β is the power-law exponent, which measures the strength of the power-law associations. This transform can be the wavelet transform [84] or the FFT of the signal [256,257]. Given its perceived benefits, the wavelet transform based on the Morlet base function are most frequently employed [5,34,82,84,176,231,236,246]. In particular, f represents the central frequency of the Morlet wavelet.

Equation (1)'s logarithmic transformation yields:

$$\log S(f) = \log a + \beta \cdot \log f \quad (2)$$

Given that equation (1) is a straight line, β and a may be found by using the least squares approach to fit the associated data.

The technique has been utilised mostly in sliding windows of various lengths moved one sample forwards. Independent windows are also utilised as well, under the restriction that the square of the Spearman's (r^2) coefficient in each window should have $r^2 \geq 0.95$, for the power-law fit to be acceptable.

5.2.2. DFA

The original time signal is first integrated in order to apply DFA. Then, within a window of size n , the integrated signal's fluctuations, $F(n)$, are found. The linear $\log(F(n)) - \log(n)$ transformation is then fitted using least-squares to get the integrated time series's scaling exponent (self-similarity parameter), α . Depending on the dynamics of the system, the $\log(F(n)) - \log(n)$ line may show one crossover at a scale n where the slope displays an abrupt shift, two crossovers at two distinct scales n_1 , n_2 [86], or nothing at all.

The following process may be used to construct the DFA of a one-dimensional temporal signal $y_i, (i = 1, \dots, N)$ [34,86,283]:

- (i) First, the original time series is integrated:

$$y(k) = \sum_{i=1}^k (y(i) - \langle y \rangle) \quad (3)$$

In equation (3), the symbols $\langle \dots \rangle$ represent the total average value of the time series, whereas k represents the different time scales.

- (ii) Next, the integrated time series $y(k)$ is divided into equal length bins, n , that do not overlap.
- (iii) The trend in the bin is subsequently expressed by the function $y_n(k)$, which is then fitted. Simple linear trends or polynomials of order 2 or higher order may be used. The notation $y_n(k)$ indicates the y coordinate of this linear function in each box n .
- (iv) Next, each box of length n is detrended in the integrated time series $y(k)$ by subtracting the local linear trend, $y_n(k)$. In this way, and for every bin, the detrended time series $y_d^n(k)$ is calculated as follows:

$$y_d^n(k) = y(k) - y_n(k) \quad (4)$$

- (v) Next, for each bin of size n , the root-mean-square (rms) of the integrated and detrended time series' fluctuations is calculated as

$$F(n) = \sqrt{\frac{1}{N} \sum_{k=1}^N \{y(k) - y_d^n(k)\}^2} \quad (5)$$

where, $F(n)$ are the rms fluctuations of the detrended time series $y_d^n(k)$.

- (vi) The technique steps (i)–(v) are repeated for different sizes (n) of the scale boxes. This indicates the precise kind of relationship that exists between $F(n)$ and n . An exponential relationship exists between $F(n)$ and n if the time series contains long-term associations.

$$F(n) \sim n^\alpha \quad (6)$$

The DFA scaling exponent α of equation (6) assesses the strength of the time series' long-term relationships.

- (vii) Equation (4)'s logarithmic translation yields a linear relationship between $\log F(n)$ and $\log(n)$. A strong linear relationship implies that the accompanying fluctuations have a long memory since they are long-lasting. This study uses the square of the Spearman's (r^2) to assess the linear fit's accuracy. According to Nikolopoulos et al. [34,231,236,283], good linear fits are considered as having $r^2 \geq 0.95$ or higher.

As with sub-section 5.2.1, DFA has also been utilised in sliding windows of various lengths moved one sample forwards.

5.2.3. Fractal Dimension Analysis with Katz's Method

The transpose array $[s_1, s_2, \dots, s_N]^T$ of the series s_i , $i = 1, 2, \dots, N$, is first determined in accordance with Katz's method, where $s_i = (t_i, y_i)$ and y_i are the measured series values at the time instances t_i [284,285]. This process yields the fractal dimension, D .

The two subsequent points of the time series (s_i and s_{i+1}) are represented by the value pairs (t_i, y_i) and (t_{i+1}, y_{i+1}) , for which the Euclidean distance is:

$$\text{dist}(s_i, s_{i+1}) = \sqrt{(t_i^2 - t_{i+1}^2) + (y_i^2 - y_{i+1}^2)} \quad (7)$$

The distances in equation (7) add up in a curve whose total length is:

$$L = \sum_{i=1}^{i=N} \text{dist}(s_i, s_{i+1}) \quad (8)$$

This curve will stretch in the planar to d , if it does not cross itself, where d is :

$$d = \max(\text{dist}(s_i, s_{i+1})), i = 2, 3, \dots, N \quad (9)$$

By combining equations (7), (8) and (9), the Katz fractal dimension, D , becomes

$$D = \frac{\log(n)}{\log(n) + \log(d/L)} \quad (10)$$

where $n = L/\bar{a}$ and \bar{a} is the average value of the distances of the points.

5.2.4. Fractal Dimension Analysis with Higuchi's Method

To determine a time series' fractal dimension, D

$$y(1), y(2), y(3), \dots, y(N) \quad (11)$$

recorded at $i = 1, 2, \dots, N$ intervals, the following is the construction of a new sequence, y_m^k [247,248,286]:

$$y_m^k : y(m), y(m+k), y(m+2k), \dots, y(m + \left\lfloor \frac{N-m}{k} \right\rfloor k) \quad (12)$$

The length of the curve associated to the time series is given by [286]:

$$L_m(k) = \frac{1}{k} \left(\sum_{i=1}^{\left\lfloor \frac{N-m}{k} \right\rfloor} y(m+ik) - y(m + (i-1)k) \right) \left(\frac{N-1}{\left\lfloor \frac{N-m}{k} \right\rfloor k} \right) \quad (13)$$

In both equations m and k are integers that specify the time interval between the series' samples and are connected by the formula $m = 1, 2, \dots, k$, where $\lfloor \dots \rfloor$ is the Gauss notation, namely, the bigger integer part of the included value.

By inserting the normalisation factor

$$\frac{N-1}{\left\lfloor \frac{N-m}{k} \right\rfloor k} \quad (14)$$

The lengths of equation (14) show an average value, $\langle L(k) \rangle$, that displays a power law of the following form:

$$\langle L(k) \rangle \propto k^{-D} \quad (15)$$

The Higuchi's fractal dimension, D , is finally calculated by the slope of the linear regression of logarithmic transformation of $\langle L(k) \rangle$ versus k where $k = 1, 2, \dots, k_{max}$. It must be noted that the time intervals are $k = 1, \dots, k_{max}$ for $k_{max} \leq 4$, i.e., $k = 1, 2, 3, 4$, for $k_{max} = 4$ and $k = \left\lceil 2^{(j-1)/4} \right\rceil$, $j = 11, 12, 13, \dots$, for $k > 4$ ($k_{max} > 4$). Again $\lfloor \dots \rfloor$ is the Gauss notation [285].

5.2.5. Fractal Dimension Analysis with Sevcik's Method

Using the approach of Sevcik [287], the fractal dimension of a time series is estimated from the Hausdorff dimension, D_h , as [285].

$$D_h = \lim_{\epsilon \rightarrow 0} \left[-\frac{\log(N(\epsilon))}{\log(\epsilon)} \right] \quad (16)$$

where $N(\epsilon)$ is the total number of ϵ -length segments that together form a curve related to the time series. $N(\epsilon) = L/2\epsilon$ [285] and D_h are as follows if the length of the curve is L .

$$D_h = \lim_{\epsilon \rightarrow 0} \left[-\frac{\log(L) - \log(2\epsilon)}{\log(\epsilon)} \right] \quad (17)$$

The N points of the curve L can be mapped to a unit square of $N \times N$ cells of the normalized metric space by twice performing a linear transformation. Equation (18) yields the fractal dimension of Sevcik' with this transformation [285,287]:

$$D_h = \lim_{N \rightarrow \infty} \left[1 + \frac{\log(L) - \log(2\epsilon)}{\log(2(N-1))} \right] \quad (18)$$

The calculation improves as $N \rightarrow \infty$.

5.2.6. Rescaled Range Analysis

In order to identify trends that could recur in the future, the R/S analysis uses two variables: the range, R , and the standard deviation, S , of the data [278,279]. In accordance with the R/S technique, the average, $\langle x \rangle_N = \frac{1}{N} \sum_{n=1}^N x(n)$, over a period of N time units, transforms a time series

$X(N) = x(1), x(2), \dots, x(N)$ into a new variable $y(n, N)$ in a specific time period $n, (n = 1, 2, \dots, N)$. The so-called cumulative deviation of the time series, $y(n, N)$, has the following formula:

$$y(n, N) = \sum_{i=1}^n (x(i) - \langle x \rangle_N) \quad (19)$$

The rescaled range is calculated as [86,278,279]:

$$R/S = \frac{R(n)}{S(n)} \quad (20)$$

The distance between the lowest and largest value of $y(n, N)$ defines the range $R(n)$ in:

$$R(n) = \max_{1 \leq n \leq N} y(n, N) - \min_{1 \leq n \leq N} y(n, N) \quad (21)$$

The standard deviation $S(n)$ is calculated as follows:

$$S(n) = \sqrt{\frac{1}{N} \sum_{n=1}^N (x(n) - \langle x \rangle_N)^2} \quad (22)$$

R/S exhibits power-law dependence on the bin size n

$$\frac{R(n)}{S(n)} = C \cdot n^H \quad (23)$$

where H is the Hurst exponent and C is a proportionality constant.

The final equation's log transformation is a linear relationship:

$$\log\left(\frac{R(n)}{S(n)}\right) = \log(C) + H \cdot \log(n) \quad (24)$$

This is used to directly calculate the Hurst exponent H , which is the slope of the best line fit. It is important to note that the only direct method to calculate Hurst exponents is via the R/S analysis.

6. Precursors and Earthquake Related Parameters

Several attempts have been made to link earthquake related parameters and data derived from precursors. There is a variety of empirical relationships between earthquake magnitudes, preparation zone areas, precursory time and other earthquake-related characteristics. Following some of these empirical relations are given.

Rikitake [288] proposed a model showing the relations between anomaly, the precursory time T in days, the magnitude of an earthquake M and distance from epicentre R in km . According to this model:

$$\log T = 0.76 \cdot M - 1.83 \quad (25)$$

Talwani [289] suggested an empirical earthquake forecast model as

$$M_L = \log D - 0.07 \quad (26)$$

where M_L is the local magnitude of an earthquake and D is the forecasting period in days).

Guha [290] provided another model associating the precursory time T in days and the magnitude M of an earthquake as

$$\log T = A + B \cdot M \quad (27)$$

where A and B are statistically determined coefficients.

Dobrovolsky et al. [291] proposed an empirical relationship for the calculation of the earthquake preparation zone R_D (km) and the magnitude (M) of the ensuing earthquake:

$$R_D = 10^{0.43 \cdot M} \quad (28)$$

Fleischer [292] suggested that the epicentral distance D in km and the magnitude M of an earthquake are associated as

$$D = (1/1.66) \cdot 10^{A \cdot M} \quad (29)$$

where $A=0.813$ for $M<3$ and $A=0.480$ for $M>3$.

Fleischer and Morgo Campero [293] suggested that

$$X_M = 10^{0.48 \cdot M} \quad (30)$$

where x_M is the dislocation range in km and M is the magnitude of an earthquake where $M \geq 3$.

Virk [294] proposed a different relation that combined the epicentral distance D in km and the magnitude M of an earthquake as

$$D = 10^{A \cdot M} \quad (31)$$

where $A=0.32$ for $10 \text{ km} < D < 50 \text{ km}$, $A=0.43$ for $50 \text{ km} < D < 100 \text{ km}$, $A=0.56$ for $100 \text{ km} < D < 500 \text{ km}$ and $A=0.63$ for $500 \text{ km} < D < 1250 \text{ km}$.

The epicentral distance, R_E , in km between a monitoring site and the earthquake's epicentre can be calculated as

$$R_E = D \cdot R \quad (32)$$

where R is the Earth's radius (6370 km) and

$$D = \cos \alpha_i \cdot \cos \alpha_j + \sin \alpha_i \cdot \sin \alpha_j \cdot (\cos(\beta_i - \beta_j)) \quad (33)$$

with (α_i, β_i) are the coordinates of the earthquake and (α_j, β_j) are the coordinates of the monitoring station [180].

Chetia et al. [165] used multiple linear regressions to examine the greatest variability caused by pressure, temperature and rainfall in soil gas radon. They suggested that the precursory time T (days), epicentral distance D (km) and magnitude M (M_w) are connected with the relationship

$$\log(DT) = 0.79 \cdot M + b \quad (34)$$

where b equals 0.18, a is approximately 3.51 and D equals roughly to $D 100.58M$.

The reader may recall, in relation to the estimations given in this section, that there is no-one to one correspondence between recorded anomalies and occurrence of an earthquake [4]. Moreover, the earthquake generation processes are multi-facet [4] and therefore a combination of techniques is needed [4,34,36,82,272] to increase the scientific evidence. In view of these references the estimations presented in this section have significant limitations. On the other hand, several papers of the previous decades, but also modern, make use of these estimations. For several scientist these are considered as adequate and enough.

7. Table of Papers

Table 1 presents a collection of papers for electromagnetic precursors. **Table 2** shows the papers collection for radon precursors. The papers in both tables are presented chronologically and therefore old events are also included. To avoid unessential records, historical earthquakes are limited to very strong and extremely strong. Although the knowledge and methodologies have evolved, the techniques of treatment of these old earthquakes are not definitely new, since they refer to the available ones of the publication time. The historical electromagnetic precursors also include the great papers

that pioneered and opened breakthroughs in the seismic knowledge. Especially in radon precursors, the data include traditional anomaly treatment that hold up-to-date, that is the grade of anomalous behaviour in respect to the baseline and the anomaly duration. Modern methods include in both cases fractal behaviour and self-organisation analysis.

The collection of papers is the most significant part of this review, because it gathers the knowledge and may assist the related research. For the reason that the papers are many, a special presentation approach was selected so as every row to present all the data of each earthquake and the maximum of available information. Since every paper is special and the published information is not uniform, a certain variety of data that are available in most of the papers have been included as column names, but effort has been put to present special information also. All papers have been accessed in the site of each journal and the available information were downloaded as BibTEX file, or converted to BIB format from the corresponding RIS record of each journal. Digital Object Identification (doi) data were also searched and inserted wherever available.

In the next pages both tables are given.

Table 1. Papers of electromagnetic precursors. The papers are presented in chronological order from the oldest to the newest. The precursory time includes also the after shock data presented in some papers. ED is the effective-sensitive distance between the monitoring site and the epicentre of the earthquake. In blank cells there is no information available in the reference(s).

Location	Magnitude	Date(s)	Emission type	Measurement frequency	Instrumentation	Method(s)	Precursory time	ED	Reference
Chile	9.5	22/05/1960	Radio	18 MHz	Radioastronomy receiver	Visual observation	6 days	Worldwide	[295]
Hollister, California	5.2	28/11/1974	ULF magnetic		Array of 7 proton magnetometers	Visual observation	7weeks-several months	11 km	[296]
Tangshan,China	7.8	28/07/1976	Resistivity			Visual observation	2-3 years	<150 km	[297]
Tangshan,China	7.8	28/07/1976	Self potential and magnetotelluric			Visual observation	3 months	<120 km	[297]
Sungpan-Pingwu,China	7.2	16/08/1976	Telluric currents			Visual observation	1month	<200 km	[298]
Sungpan-Pingwu,China	6.8	22/08/1976	Telluric currents			Visual observation	1month	<200 km	[298]
Sungpan-Pingwu,China	7.2	23/08/1976	Telluric currents			Visual observation	1month	<200 km	[298]
Kyoto, Japan	7.0	31/03/1980	LF electric	81 kHz	Electric antenna	Visual observation	0.5 h	250 km	[43]
Tokyo, Japan	5.3	25/09/1980	LF electric	81 kHz	Electric antenna	Visual observation	1 h	55 km	[43]
Tokyo, Japan	5.5	28/01/1981	LF electric	81 kHz	Electric antenna	Visual observation	3/4 h	50 km	[43]
Kalamata, Greece	6.2	13/09/1986	Electric			Visual observation	3-5 days	200 km	[299]
Spitak, Armenia	6.9 (M_s)	07/12/1988	ULF magnetic	0.01-1Hz	3-axis magnetometers	Visual observation,statistical analysis	4h	128 km	[7]
Spitak, Armenia	6.9 (M_s)	07/12/1988	ULF magnetic	0.005-1Hz	3-axis magnetometers	Visual observation,statistical analysis	4h	120 km,200 km	[65]
Loma Prieta, California	7.1 (M_s)	18/11/1989	ULF magnetic	0.01Hz		Visual observation,statistical analysis	3h	7 km	[65]
Loma Prieta, California	7.1 (M_s)	19/11/1989	ULF,HF electromagnetic	0.01Hz,32kHz	Ground-based magnetometers	Visual observation	3h	52 km	[58]
Spitak, Armenia	6.9 (M_s)	23/01/89	LF to HF electromagnetic	140,450,800,4500,15000 Hz	COSMOS-1809 satellite with 12 satellite orbits of f<450 Hz	Visual observation,FFT	<3h		[300]
Upland, California	4.3	17/04/1990	ULF magnetic	3-4Hz	Vertical magnetic sensor	Power law,FFT	1 day	160 km	[301]
West Iran	7.5	20/06/1990	Ionospheric radiowave	0-8kHz,10-14kHz	INTERCOSMOS-19 satellite	Visual observation, Modelling	16days	250-2000 km	[302]
Watsonville, California	4.3	23/03/1991	ULF magnetic	3.0-4.0 Hz	North-south magnetic sensor	Statistical AnalysisPower law with FFT	data averaged over 2 days	600 km	[301]
Watsonville, California	4.3	23/03/1991	ULF magnetic	3.0-4.0 Hz	Vertical magnetic sensor	Power law-FFT	data averaged over 2 days)	600 km	[301]
NW Crete,Greece	6.0	21/11/1992	HF electric	41,53 MHz	Electric dipole antennas	Visual observation	1-3 days	20-150 km	[303]
Coalinga, California	4.0	15/01/1992	ULF magnetic	3.0-4.0 Hz	Vertical magnetic sensor	Power law-FFT	data averaged over 2 days	400 km	[301]
Hokkaido, Japan	7.8	12/07/1993	foF2 ionospheric			Visual observation,statistical analysis	3 days	290 km,780 km,1280 km	[136]
Guam	7.1 (M_s)	08/08/1993	ULF magnetic	0.02-0.05 Hz	3-axis ring core type fluxgate magnetometers	Fractal analysis,FFT	1 month	65 km	[60,304]

Continued on next page

Location	Magnitude	Date(s)	Emission type	Measurement frequency	Instrumentation	Method(s)	Precursory time	ED	Reference
Guam	8.3 (M_f)	08/08/1993	ULF magnetic	0.02-0.05 Hz	3-axis ring core type, fluxgate magnetometers	Multifractal Detrended Fluctuation Analysis	1 month	65 km	[242]
Hokkaido, Japan	8.2 (MJMA)	07/12/1993	SES	≤ 1 Hz	Electric antennas	Natural time analysis	1 month	δlat and $\delta\text{long} < 30$	[305]
Hokkaido-Toho Oki, Japan	8.1 (M_W)	04/10/1994	HF electric		Borehole antenna	Visual observation	20 min	>1000 km	[281]
Hokkaido, Japan	7.6 (MJMA)	04/10/1994	SES	≤ 1 Hz	Electric antennas	Natural time analysis	1 month	δlat and $\delta\text{long} < 30$	[305]
Hokkaido, Japan	7.4 (MJMA)	28/12/1994	SES	≤ 1 Hz	Electric antennas	Natural time analysis	1 month	$\delta\text{lat}, \delta\text{long} < 30$	[305]
Hyogo-ken Nanbu (Kobe), Japan	7.2 (MJMA)	17/01/1995	HF electric	22.2 MHz	Phase-switched interferometer polarized antennas		1 h	77 km	[306]
NE Samos, Greece	5.0	07/05/1995	HF electric	41,53 MHz	Electric dipole antennas	Visual observation	1-3 days	20-150 km	[303]
Kozani-Grevena, Greece	6.6 (M_W)	13/05/1995	HF electric, LF magnetic				2 weeks	70 km, 200 km	[307]
Kozani-Grevena, Greece	6.6 (M_W)	13/05/1995	HF electric	41,54 MHz, magnetic 3,10 kHz	Electric dipole and magnetic loop antennas	Fractal analysis	20 h	284 km	[308,309]
Kozani-Grevena, Greece	6.6 (M_W)	13/05/1995	HF electric	41,54 MHz, magnetic 3,10 kHz	Electric dipole and magnetic loop antennas	Fractal analysis and Statistical methods.	20 h	284 km	[309]
Kozani-Grevena, Greece	6.6 (M_W)	13/05/1995	HF electric	41,54 MHz, magnetic 3 kHz	Electric dipole and magnetic loop antennas	Fractal analysis and Statistical methods.	20 h	284 km	[84]
Kozani-Grevena, Greece	6.6 (M_W)	13/05/1995	HF electric	41 MHz	Electric dipole and magnetic loop antennas	Fractal analysis and Statistical methods.	20 h	284 km	[310]
Kozani-Grevena, Greece	6.6 (M_W)	13/05/1995	HF electric and LF magnetic	41,54 MHz and 3,10 kHz	Electric dipole and magnetic loop antennas	Intermittent dynamics of critical fluctuations	20 h	284 km	[311]
Kozani-Grevena, Greece	6.6 (M_W)	13/05/1995	SES	≤ 1 Hz	Electric antennas	Visual and mathematical analysis	4 weeks	70-80 km	[312,313]
Kozani-Grevena, Greece	6.8 (M_S)	13/05/1995	SES	≤ 1 Hz	Electric antennas	Visual and mathematical analysis	24,25 days	70-80 km	[313]
Kozani-Grevena, Greece	6.8 (M_S)	13/05/1995	SES	≤ 1 Hz	Electric antennas	Visual and mathematical analysis	22 min	70-80 km	[314]
SE Crete, Greece	5.0	29/07/1995	HF electric	41,53 MHz	Electric dipole antennas	Visual observation	1-3 days	20-150 km	[303]
Hyogo-ken Nanbu (Kobe), Japan	7.2 (MJMA)	11/06/1996	DC potential, LF radio waves and MF and HF radio waves	223 Hz and 77.1 MHz and 1-20 kHz, 163 kHz	LF Omega transmitter and receiver	Visual, statistical analysis	<7 days	>100 km	[315]
Hyogo-ken Nanbu (Kobe), Japan	7.2 (MJMA)	11/06/1996	HF radio waves	10.2 kHz	LF Omega transmitter and receiver	Statistical Analysis, modelling	2 days	70 km	[7]
Akita-ken Nairiku-nanbu, Japan	5.9	11/08/1996	LF and HF electric	10 kHz and 1 MHz	Vertical-dipole ground electrodes	Visual analysis and analysis of related parameters	6 days	<100 km	[315]
Chiba-ken Toho-oki, Japan	6.6	11/09/1996	Electric	10 kHz, 1 MHz	Vertical-dipole ground electrodes	Visual analysis and analysis of related parameters	3 days	320 and 430 km	[315]
Umbria-Marche, Italy	5.5	26/03/1998	LF radio waves,	0.006 Hz	Radio wave vertical antenna		1.5 months	818 km	[316]
San Juan Bautista, California	5.1 (M_W)	12/08/1998	UHF magnetic	0.01-10 Hz	3-component magnetic field inductor coils	Power spectrum analysis	2 h	3 km	[317]

Continued on next page

Location	Magnitude	Date(s)	Emission type	Measurement frequency	Instrumentation	Method(s)	Precursory time	ED	Reference
Egio,Eratini,Greece	6.6(M_W)	07/09/1999	LF electric and HF magnetic	41,54 MHz and 3,10kHz	Electric dipole, magnetic loop antennas	Fractal analysis,Block Entropy	12-17h	<300 km	[318]
Athens, Greece	5.9 (M_W)	07/09/1999	SES and LF electric and HF magnetic	1Hz and 41,54,135 MHz and 3,10 kHz	ULF, Electric dipole and magnetic loop antennas	Fractal analysis,Block Entropy	<3 h	247 km	[89]
Athens, Greece	5.9 (M_W)	07/09/1999	HF magnetic	3,10 kHz	Magnetic loop antennas	Delay Times Method, Block Entropy,Spectral Fractal Analysis	12-17 h	247 km	[319]
Athens, Greece	5.9 (M_W)	07/09/1999	HF magnetic	3,10 kHz	Magnetic loop antennas	Fractal analysis	12-17 h	247 km	[320]
Athens, Greece	5.9 (M_W)	07/09/1999	HF magnetic	3,10 kHz	Magnetic loop antennas	Symbolic Dynamics	12-17h	247 km	[320]
Athens, Greece	5.9 (M_W)	07/09/1999	HF magnetic	3,10 kHz,HF electric 41,54 MHz	Electric dipole antennas, magnetic loop antennas	Wavelet Power Spectrum analysis	12-17 h	247 km	[308,309]
Athens, Greece	5.9 (M_W)	07/09/1999	HF magnetic	10 kHz	Electric dipole antennas, magnetic loop antennas	Block Entropy	12-17 h	247 km	[261]
Athens, Greece	5.9 (M_W)	07/09/1999	HF magnetic	3,10 kHz	Magnetic loop antennas	Block Entropy	12-17 h	247 km	[320]
Athens, Greece	5.9 (M_W)	07/09/1999	HF magnetic	3,10 kHz,electric 154 MHz	Electric dipole and magnetic loop antennas	Intermittent dynamics of critical fluctuations	20 h	247 km	[311]
Athens, Greece	5.9 (M_W)	07/09/1999	LF electric and HF magnetic	135 MHz and 3,10 kHz,	Electric dipole and magnetic loop antennas	Intermittent dynamics of critical fluctuations	>3 h	247 km	[311]
Athens, Greece	5.9 (M_W)	07/09/1999	HF magnetic	10 kHz	Magnetic loop antennas	Tsallis Entropy	12-17 h	247 km	[321]]
Chi-Chi, Taiwan	7.6 (M_W)	20/09/1999	foF2 ionospheric		IPS-42 ionosonde	Visual observation	3-4 days	120 km	[322]
Chia-Yii, Taiwan	6.4 (M_W)	22/10/1999	foF2 ionospheric		IPS-42 ionosonde	Visual observation	b1-3 days	179 km	[322]
Izu-Penisula,Japan	6.4 (MJMA)	01/07/2000	ULF magnetic	0.001-1 Hz	3-axis ring core-type fluxgatemagnetometers	Fractal analysis with FFT, Higuchi,Bulgara-Klein methods	<1 month	80 km-1160 km	[250]
Izu-Penisula,Japan	6.4 (MJMA)	01/07/2000	ULF magnetic	0.001-1 Hz	3-axis ring core-type fluxgatemagnetometers	Fractal analysis with FFT,Fractal dimension	<1 month	80 km-1160 km	[256]
Izu-Penisula,Japan	6.1 (MJMA)	09/07/2000	ULF magnetic	0.001-1 Hz	3-axis ring core-type fluxgatemagnetometers	Fractal analysis with FFT, Higuchi,Bulgara-Klein methods	<1 month	80 km-1160 km	[250]
Izu-Penisula,Japan	6.1 (MJMA)	09/07/2000	ULF magnetic	0.001-1 Hz	3-axis ring core-type fluxgatemagnetometers	Fractal analysis with FFT,Fractal dimension	<1 month	80 km-1160 km	[256]
Izu-Penisula,Japan	6.3 (MJMA)	15/07/2000	ULF magnetic	0.001-1 Hz	3-axis ring core-type fluxgatemagnetometers	Fractal analysis with FFT, Higuchi,Bulgara-Klein methods	<1 month	80 km-1160 km	[250]
Izu-Penisula,Japan	6.3 (MJMA)	15/07/2000	ULF magnetic	0.001-1 Hz	3-axis ring core-type fluxgatemagnetometers	Fractal analysis with FFT,Fractal dimension	<1 month	80 km-1160 km	[250]

Continued on next page

Location	Magnitude	Date(s)	Emission type	Measurement frequency	Instrumentation	Method(s)	Precursory time	ED	Reference
Izu-Peninsula, Japan	6.4 (MJMA)	18/08/2000	ULF magnetic	0.001-1 Hz	3-axis ring core-type fluxgate magnetometers	Fractal analysis with FFT, Higuchi, Bulgara-Klein methods	<1 month	80 km-1160 km	[256]
Lefkas, Greece	5.9 (M_W)	14/06/2003	LF electric and HF magnetic	41,54 MHz and 3,10 kHz	Electric dipole and magnetic loop antennas	Fractal analysis, Block Entropy	12-17h	<300 km	[318]
Andaman, Sumatra, Indonesia	9.0 (M_W)	26/12/2004	ULF magnetic	1 Hz	3-axis ring core-type, fluxgate magnetometers	Spectral density ratio analysis, transfer functions analysis, fractal dimension	<1.5 month	<750 km	[323]
Andaman, Sumatra, Indonesia	8.7	26/12/2004	ULF magnetic	1 Hz	CHAMP satellite vector magnetic antennas	Wavelet Power Spectrum analysis	2 h	700 km	[324]
Nias, Sumatra, Indonesia	8.7 (M_W)	28/03/2005	ULF magnetic	1 Hz	3-axis ring core-type, fluxgate magnetometers	Spectral density ratio analysis, transfer functions analysis, fractal dimension	<1.5 month	<750 km	[323]
Nias, Sumatra, Indonesia	8.7 (M_W)	28/03/2005	ULF magnetic	1 Hz	CHAMP satellite vector magnetic antennas	Wavelet Power Spectrum analysis	2 h	700 km	[324]
Miyagi-ken oki Japan	7.2 (M_W)	16/08/2005	Electric	49.5 MHz	Discon-type antenna from 25-1300 MHz	Multifractal detrended fluctuation analysis	2-3 weeks, few days for Kunimi station	90-140 km	[241]
Mid Niigata prefecture	6.8(MJMA)	16/08/2005	DC and ULF magnetic and HF electro-magnetic	0.02-0.05 Hz and 40 kHz	3-axis ring core-type fluxgate magnetometers, Discon type antennas from 25-1300 MHz	Signal analysis with FFT	17-21, 5-7 days	<220 km	[325]
Greece	5.2 (M_L)	18/01/2007	SES	≤ 1 Hz	Electric and magnetic antennas	Natural time analysis	3 min	<150 km	[326]
Greece	5.8 (M_L)	03/02/2007	SES	≤ 1 Hz	Electric and magnetic antennas	Natural time analysis	22 min	<150 km	[326]
Vanuatu, Japan	7.1 (MJMA)	25/03/2007	TEC		DEMETER satellite	Statistical analysis	15 days		[327]
Honshu, Japan	6.7 (MJMA)	25/03/2007	TEC		DEMETER satellite	Statistical analysis	15 days		[327]
Lesvos, Greece	6.1 (M_L)	12/06/2007	LF electric and HF magnetic	41,54 MHz and 3,10 kHz	Electric dipole and magnetic loop antennas	DFA, Power law	10-12 days	30 km	[231]
Wenchuan, China	8.0 (M_S)	12/05/2008	DC, ULF	≤ 1 Hz	Cr18Ni9C electrodes	Visual observations	3 days	1000 km	[328]
Greece	6.4 (M_W)	08/06/2008	SES	≤ 1 Hz	Electric and magnetic antennas	Natural time analysis		<30 km	[264]
L'Aquila, Italy	6.3	06/04/2009	LF electric and HF magnetic	41,54 MHz and 3,10 kHz	Electric dipole and magnetic loop antennas	Fractal analysis, Block Entropy, DFA, R/S analysis, Hurst analysis,	<3h	816 km	[4,82]
Oran, Algeria	5.5 (M_W)	06/06/2008	Rinex, F_2 disturbances, TEC		Geodetic stations	Seismological, Spectral analysis	Several days		[329]
Tokachi, Japan	8.0 (MsMA)	26/09/2003	SES	≤ 1 Hz	Electric antennas	Natural time analysis	1 month	$\delta lat, \delta long < 30$	[305]

Continued on next page

Location	Magnitude	Date(s)	Emission type	Measurement frequency	Instrumentation	Method(s)	Precursory time	ED	Reference
Yutian, China	7.3 (M_S)	20/03/2008	TEC and ULF electric field data		Onboard DEMETER, Swarm and China Seismo-Electromagnetic satellites	Statistical, visual analysis	3 min-2 days		[330]
Lake Baikal, Siberia	6.3	27/08/2008	Electromagnetic signals from thunderstorms	VLF range	Single-point lightning direction finder-rangefinder	Visual observations	hours		[331]
Indonesia	5.0	07/01/2009	Electromagnetic signals from thunderstorms	VLF range	Single-point lightning direction finder-rangefinder	Visual observations	7 days		[331]
Chichi-jima, Japan	7.8 (MJMA)	22/10/2010	SES	≤ 1 Hz	Electric antennas	Natural time analysis	1 month	$\delta\text{lat}, \delta\text{long} < 30$	[305]
Conception, Chile	8.8 (M_W)	27/02/2010	$N_m f_2$ ionospheric anomalies		FORMOSAT-3/COSMIC satellite	Kriging interpolation, global $N_m f_2$ map	5 h	epicentre area	[332]
Tohoku, Japan	9.0 (MJMA)	11/3/2011	SES	≤ 1 Hz	Electric antennas	Natural time analysis	1 month	$\delta\text{lat}, \delta\text{long} < 30$	[305]
Tohoku, Japan	9.0 (MJMA)	11/3/2011	GPS TEC		Modified single layer mapping function at the ionospheric pierce points at 350 km	GPS satellites (PRN 18, PRN26)	40-50 min	500-600 km	[333, 334]
Tohoku, Japan	9.0 (MJMA)	11/03/2011	Ionospheric measurements	HF 3-25 MHz	Ionosonde detection network combined with Digisondes and COSMIC satellite	HF Doppler, planar ionospheric disturbances	6 h after	2000 km	[335]
Japan	6.0	14/03/2012	Electromagnetic signals from thunderstorms	VLF range	Single-point lightning direction finder-rangefinder	Visual observations	10 days	3000 km	[331]
India	5.6	25/04/2012	HF electric field	3.012 kHz	GPS Terrestrial vertical antenna	Visual observations	1-13 days	2671 km	[336]
India	5.6	27/04/2012	HF electric field	3.012 kHz	GPS Terrestrial vertical antenna	Visual observations	1-13 days	3284 km	[336]
Dholavira, India	5.1 (M_W)	20/06/2012	ULF magnetic and data K_p, D_{st}	0.001-0.5 Hz	Digital fluxgate magnetometer	Visual and fractal dimensions	7 days	around, above epicentre	[337]
Yutian, China	6.3 (M_S)	12/08/2012	ULF electric field data, TEC	≤ 1 Hz	Onboard DEMETER, Swarm and China Seismo-Electromagnetic satellites	Statistical, visual analysis	10-20 days		[330]
India	5.9	22/07/2013	HF electric field	3.012 kHz	GPS Terrestrial vertical antenna	Visual observations	1-13 days	2642 km	[336]
India	5.7	20/09/2013	HF electric field	3.012 kHz	GPS Terrestrial vertical antenna	Visual observations	1-13 days	1905 km	[336]

Continued on next page

Location	Magnitude	Date(s)	Emission type	Measurement frequency	Instrumentation	Method(s)	Precursory time	ED	Reference
India	5.7	02/10/2013	HF electric field	3.012kHz	GPS Terrestrial vertical antenna	Visual observations	1-13 days	2766 km	[336]
Yutian, China	7.3 (M_S)	12/02/2014	TEC and ULF electric field data		Onboard DEMETER, Swarm and China Seismo-Electromagnetic satellites	Statistical,visual analysis	same days		[330]
Greece	6.9	24/05/2014	SES and geomagnetic signals	0.5-40 Hz and 0.0001-100 kHz	Mikhnevo GPO (seismometric, radiophysical, magnetometric, electrical equipment				[338]
Ileia,Greece	4.4 (M_L)	30/08/2015	HF magnetic	3,10 kHz	Magnetic loop antennas	Fractal analysis	3 days	24 km	[35]
Illapel, Chile	8.3 (M_W)	16/09/2015	Co-seismic ionospheric TEC	0.1-1 Hz	Global Navigation Satellite System	Wave perturbation ionosphere model with seismic source		1500 km	[339]
Ileia,Greece	4.5 (M_L)	12/12/2015	HF magnetic	3,10 kHz	Magnetic loop antennas	Fractal analysis	3 days	24 km	[35]
Sumatra	7.8 (M_W)	02/03/2016	TEC	3.012kHz	GPS Terrestrial vertical antenna	3D tomography method	11-16 min after	1°,75km	[340]
Afghanistan	6.6	10/04/2016	Seismic and geomagnetic and acoustic signals	0.5-40 Hz and 0.0001-100kHz and 10^{-4} -20Hz	Mikhnevo observatory,LEMI-018 triaxial fluxgate magnetometer	Visual observations		2000-3000 km	[338]
Italy	6.6	30/06/2016	Seismic and geomagnetic and acoustic signals	0.5-40 Hz and 0.0001-100kHz and 10^{-4} -20Hz	Mikhnevo observatory,LEMI-018 triaxial fluxgate magnetometer	Visual observations		2000-3000 km	[338]
Chiapas,Mexico	M8.2	06/07/2017	SES	≤ 1 Hz		Natural time analysis	few hours		[64]
Greece	6.6	20/07/2017	Seismic and geomagnetic and acoustic signals	0.5-40 Hz and 0.0001-100kHz and 10^{-4} -20Hz	Mikhnevo observatory,LEMI-018 triaxial fluxgate magnetometer	Visual observations		2000-3000 km	[338]
Mexican flat slab	M7.1	19/09/2017	SES	≤ 1 Hz		Natural time analysis	several hours		[64]
Iraq	7.3	12/11/2017	Seismic and geomagnetic and acoustic signals	0.5-40 Hz and 0.0001Hz-100kHz and 10^{-4} -20Hz	Mikhnevo observatory,LEMI-018 triaxial fluxgate magnetometer	Visual observations		2000-3000 km	[338]
Ileia,Greece	4.5 (M_L)	07/05/2018	HF magnetic	3,10 kHz	Magnetic loop antennas	Fractal analysis	3 days	24 km	[35]
Lombok,Indonesia	6.4	28/07/2018	Ne,Te and TEC	Onboard sensors	China Seismo-Electromagnetic Satellites	dTEC,Statistical analysis	1-5 days	2000 km	[341]
Lombok, Indonesia	6.8	05/08/2018	Ne,Te and TEC	Onboard sensors	China Seismo-Electromagnetic Satellites	dTEC,Statistical analysis	1-5 days	2000 km	[341]
Lombok, Indonesia	5.9	09/08/2018	Ne,Te data and TEC	Onboard sensors	China Seismo-Electromagnetic Satellites	dTEC,Statistical analysis	1-5 days	2000 km	[341]
Lombok, Indonesia	6.9	19/08/2018	Ne,Te data and TEC	Onboard sensors	China Seismo-Electromagnetic Satellites	dTEC,Statistical analysis	1-5 days	2000 km	[341]

Continued on next page

Location	Magnitude	Date(s)	Emission type	Measurement frequency	Instrumentation	Method(s)	Precursory time	ED	Reference
Indonesia	7.5 (M_W)	28/09/2018	Physical properties of atmosphere and NeTe,Ionospheric disturbances		China Seismo Electromagnetic Satellites	Seismological,climatological analysis	3,7,6 months and 2.7 months	3°	[342]
Zakynthos,Greece	6.6 (M_L)	25/10/2018	LF electric and HF magnetic	41,54 MHz and 3,10 kHz	Electric dipole and magnetic loop antennas	Fractal analysis,Block Entropy, DFA, R/S analysis,Hurst analysis	post activity	40 km	[34]
Ileia,Greece	4.3 (M_L)	04/02/2019	HF magnetic	3,10 kHz	Magnetic loop antennas	Fractal analysis	3 days	24 km	[35]
Ridgecrest, Mexico	M7.1	06/072019	SES	≤ 1 Hz		Natural time analysis	several hours before and after		[64]
Indonesia	6.9 (M_W)	07/07/2019	VLF	48.83-366.21 Hz	Electric Field Detector of China Seismo-Electromagnetic Satellites	Electric field PSD	before and after	near the epicentre	[343]
Indonesia	7.2 (M_W)	14/07/2019	VLF	48.83-366.21 Hz	Electric Field Detector of China Seismo-Electromagnetic Satellites	Electric field PSD	before and after	near the epicentre	[343]
Laiwui, Indonesia	7.2 (M_W)	14/07/2019	TEC,plasma,Global ionospheric Map		China Seismo-Electromagnetic Satellite	Cross-validation analysis and moving mean method	1,3,8 days		[339]
Jiashi, China	6.4 (M_S)	19/01/2020	Electron density and rock temperature		Zhangheng-1 electromagnetic satellite	15 days	150 km	[344]	
Yutian, China	6.5 (M_S)	25/06/2020	ULE,TEC,Global ionospheric Map	≤ 1 Hz	Onboard DEMETER, Swarm and China Seismo-Electromagnetic satellites	Statistical,visual analysis	same days		[330]
Turkey	7.8 (M_W)	06/02/2023	TEC		Global Navigation Satellite System,ionosondes	Statistical,visual analysis	22-25 min after	750 km	[16]
Turkey	7.5 (M_W)	06/02/2023	TEC		Global Navigation Satellite System,ionosondes	Statistical,visual analysis	22-25 min after	750 km	[16]

Table 2. Papers of radon precursors. The papers are presented in chronological order from the oldest to the newest. The precursory time includes also the after shock data presented in some papers. RA stands for the relative amplitude of the radon anomalies and AD for the anomaly duration. SSNTDs stands for solid state nuclear track detectors. ED is the effective-sensitive distance between the monitoring site and the epicentre of the earthquake. In blank cells there is no information available in the reference(s). Russian Federation is used as the successor state of the former USSR .

Location	Magnitude	Date(s)	RA	AD (days)	Instrumentation	Methodology	Precursory time	ED	Reference
Pohai Bay,China	7.4	18/07/1969	60 %	170 days	Instruments of Kutzan station of radon in water	Visual observations		200 km	[189]
Szechwan Luhuo,China	7.9	06/02/1973	120 %	9 days	Instruments of Tangku station of radon in water	Visual observations		170 km	[187,189]
Markansu, Russian Federation	7.3	04/02/1975	38 % and 17 %	270 days and 50 days	Instruments of Alma-Ata station of radon in water	Visual observations		530 km	[189]
Liaoning,Haicheng,China	7.3	04/02/1975	38 % and 17 %	270 days and 50 days	Instruments of Tangangzi station of radon in soil	Visual observations		50 km	[189,345]
Liaoning,Haicheng,China	7.3	04/02/1975	10 %	1 day	Instruments of Liaoyang station of radon in soil	Visual observations		85 km	[189,346]
Gazli,Russian Federation	7.3	17/05/1976	220 %	4 days	Instruments of Tashkent station of radon in water	Visual observations		470 km	[189]
Yunnan Lungling,China	7.5	29/05/1976	20 %	510 days	Instruments of Lungling station of radon in soil	Visual observations		190 km	[187,189]
Yunnan Lungling,China	7.5	29/05/1976	8 %	160 days	Instruments of Erhyuan station of radon in soil	Visual observations		470 km	[187,189]
Szechwan Songpan Pingwu,China	7.2	16/08/1976	29 %	480 days	Instruments of Erhyuan station of radon in soil	Visual observations		40 km	[187,189]
Szechwan Songpan Pingwu,China	7.2	16/08/1976	70 %	7 days	Instruments of Kutzan station of radon in soil	Visual observations		320km	[189,346]
Hopeh Tangshan,China	7.8	27/07/1976	30 %	5 days	Instruments of Tangshan station of radon in water	Visual observations		5 km	[189,347]
Hopeh Tangshan,China	7.8	27/07/1976	50 %	15 days	Instruments of Antze station of radon in water	Visual observations		100 km	[189,347]

Continued on next page

Location	Magnitude	Date(s)	RA	AD	Instrumentation	Methodology	Precursory time	ED	Reference
Isferi Batnen,Russian Federation	6.6	31/01/1977	-30 %	60 days	Instruments of Tashkent station of radon in water	Visual observations		190 km	[189]
Hopeh Chienan,China	6.0	04/03/1977	70 %	3 days	Instruments of Peking station of radon in water	Visual observations		200 km	[189,346]
Hopeh Lutai,China	6.7	12/03/1977	30 %	1 day	Instruments of Tungchao station of radon in water	Visual observations		115 km	[189,346]
Isferi Batnen,Russian Federation	6.6	24/03/1977	-20 %	125 days	Instruments of H-O-Garm station of radon in water	Visual observations		200 km	[189]
Alma-Ata, Russian Federation	7.1	04/02/1978	32 %	50 days	Instruments of Alma-Ata station of radon in water	Visual observations		65 km	[189]
Zaslai,Russian Federation	6.7	01/11/1978	-30 %	470 days	Instruments of Obi-Garm station of radon in water	Visual observations		270 km	[189]
Zaslai,Russian Federation	6.7	01/11/1978	-40 %	470 days	Instruments of Yavros station of radon in water	Visual observations		300 km	[189]
Izu-Oshima,Japan	6.8	14/01/1978	7 %	230 days	Instruments of SKE-1 station of radon in water	Visual observations		25 km	[187,189]
Izu-Oshima,Japan	6.8	14/01/1978	-8 %	7 days	Instruments of SKE-1 station of radon in water	Visual observations		25 km	[187,189]
Imperial valley,California,USA	6.6	15/10/1979	400 %	116 days and 50 days	Instruments of KPAS station	Radon in water		335 km	[188,189]
Irpinia, Italy	6.5	23/11/1980	170 %	5-6 months	Instruments of Rieti station of radon in ground-water	Visual observations	4 months	150 km	[348]
Japan	7.9	06/03/1984	few days		Instruments for radon in groundwa-ter	Bayesian statistics, $\pm 2\sigma$	1 week	1000 km	[349]
Japan	6.7	06/02/1987	few days	4	Instruments for radon in groundwa-ter	Bayesian statistics, $\pm 2\sigma$	3 days	130 km	[349]
Equador	6.9	06/03/1987	230 %	30 days	Radon in soil,SSNTDs	Visual observations	50 days	200 km	[350]

Continued on next page

Location	Magnitude	Date(s)	RA	AD	Instrumentation	Methodology	Precursory time	ED	Reference
Uttarkashi, India	7.0 (M_s)	20/10/1991	180 %	7 days	Radon in soil, SSNTDs	Visual observations	1 week	450,330 km	[351,352]
Mindoro, Philippines	7.1	11/04/1994	600%	7 days	BARASOLVDG	Visual observations	22 days	48km	[353]
Kobe, Japan	7.2	1/17/1995	-2 %	4 months	Radon in atmosphere, flow ionisation chamber at 18 m	Daily min data analysis	4 to 0 months	130 km	[29,216,354]
Chamoli, India	6.5(M_s)	29/03/1999	200 %	2 days	Radon in soil, water with emanometric technique	$\pm 2\sigma$ 1-7 days	393 km	[352]	
Hiwacho-Mitsugaichi, Shobara, Japan	7.3 (MJMA)	06/10/2000	16-20 %	>6 months	Gas flow ionisation chamber	Residual analysis		207 km	[355]
Scotia sea, Antarctica	7.5 (M_s)	04/08/2003	400-700 %	16 days	CR-39, TASTRAK	Visual, power law	6	1176 km	[356]
Chengkung, Taiwan	6.8	10/12/2003	-13 %	6 months	Radon in water, liquid scintillation counter, wells 167-187 m deep	30 km	65 days	20 km	[194]
Yura, Hidaka, Japan	7.4(MJMA)	05/10/2004	16-20 %	>6 months	Gas flow ionisation chamber	Residual analysis		22 km	[355]
Indonesia	9.1	26/12/2004	60 %	4-6 days	Radon and progeny in gases from thermal springs at Bakreswar, India, $\pm 2\sigma$, visual observations	2275 km	[357]]		
Middle Kurils, Simushir Island, Kamchatka Peninsula	8.1(M_W)	20/04/2006	33-35 %		Gas-discharge counter for radon progeny	Visual observations	8 months-3 years	800 km	[154]
Olutorsk, Kamchatka Peninsula	7.6 (M_W)	/20/04/2006	33-35 %	33-35 %	Gas-discharge counter for radon progeny	Visual observations	8 months-3 years	1035 km	[154]
Middle Kurils Kamchatka Peninsula Simushir Island, Pacific Ocean	8.3 (M_W)	13/01/2007	33-35 %		Gas-discharge counter for radon progeny	Visual observations	8 months-3 years	800 km	[154]
Wenchuan, China	8 (M_s)	12/05/2008	10 times the base-line	12 days	SD-3 A, automatic radon instrument, Guzan station	Statistical analysis		155 km	[205]
Wenchuan, China	8 (M_s)	12/05/2008	5 times the base-line	scattered days	FD-125, ZnS(Ag)	Sliding window power law, DFA, Fractal Dimension, 13 method combination analysis	1 -2 months	150-500 km	[36]

Continued on next page

Location	Magnitude	Date(s)	RA	AD	Instrumentation	Methodology	Precursory time	ED	Reference
Kato Achaia,Peloponnese,Greece	6.5(M_L)	06/08/2008	20 times the base-line	12 h	Alpha GUARD,CR-39,radon in soil	Sliding window power law,statistics, outliers	2 months	40 km	[5]
Kato Achaia,Peloponnese,Greece	6.5(M_L)	06/08/2008	20 times the base-line	12 h	Alpha GUARD radon in soil	Sliding window power law,DFA,spectrogram,scalogram	2 months	40 km	[23]
Kato Achaia,Peloponnese,Greece	6.5(M_L)	06/08/2008	20 times the base-line	12 h	Alpha GUARD radon in soil	Sliding window Fractal dimension analysis,Hurst exponents	2 months	40 km	[23]
Kato Achaia,Peloponnese,Greece	6.5(M_L)	06/08/2008	20 times the base-line	12 h	Alpha GUARD radon in soil	Sliding window R/S ,DFA and Block Entropy analysis,R-L,Variogram methods,Fractal Dimensions	2 months	40 km	[21]
Aegean Sea,Lesvos area,Greece	5.0 (M_L)	19/03/2008	20 times the base-line	1 h	Alpha GUARD radon in soil	Sliding window R/S ,DFA and Block Entropy analysis,R-L,Variogram methods,Fractal Dimensions	3 months	40-70 km	[21]
Tohoku,Japan	9.0(MJMA)	11/03/2011	80-160 times the base-line	>16 days	Radon,thoron instrumentation at Seongryu Cave	Statistical,visual analysis	1 month		[205]
PhekN agaland,India	5.8	29/07/2012	2-3 times the base-line	1 month	LR-115 in soil	$\pm 2\sigma$,visual observations	16-31 days	224 km	[358]
Myanmar,India	6.0	29/07/2012	2-3 times the base-line	1 month	LR-115 in soil	$\pm 2\sigma$,visual observations	16-31 days	132 km	[358]
Awaji Island,Japan	6.7 (MJMA)	13/04/2013	16-20 %	>6 months	Gas flow ionisation chamber	Residual analysis		44 km	[355]
Luhsan,Cina	7 (M_S)	20/04/2013	10 times the base-line	20 days	SD-3 A,automatic radon instrument,Guzan station	Statistical analysis		82 km	[205]
Gansu,China	6.6 (M_S)	22/07/2013	10-20 %	2 months	FD-125 instrument,radon in ground-water	Monofractal,Multifractal DFA		688 km	[180]
Evia Island,Greece	5.0 (M_L)	15/11/2014	-5 times the base-line	10 min	VDG BARA-COL,radon in soil	Sliding window R/S ,DFA,scalograms	10-12 days	100 km	[32]
Nepal	7.8	25/04/2015	4 times the base-line	15 days	LR-115 in soil	$\pm 2\sigma$,visual observations	5 days	722 km	[359]

Continued on next page

Location	Magnitude	Date(s)	RA	AD	Instrumentation	Methodology	Precursory time	ED	Reference
West Bengal, India	7.8	26/04/2015	3.5 times the base-line	15 days	LR-115 in soil	$\pm 2\sigma$, visual observations	6 days	612 km	[359]
Kalamei, Nepal	7.8	12/05/2015	3 times base-line	15 days	LR-115 in soil	$\pm 2\sigma$, visual observations	5 days	618 km	[359]
Lesvos Island, Greece	4.1 (M_L)	10/09/2015	8-20 times the base-line		Alpha GUARD radon in soil	Sliding window R/S, DFA, scalograms		50 km	[236]
Lesvos Island, Greece	4.6 (M_L)	26/10/2015	8-20 times the base-line		Alpha GUARD radon in soil	Sliding window R/S, DFA, scalograms		50 km	[236]
Zhupanovo, Kamchatka Peninsula	7.2 (M_W)	30/01/2016	33-35 %		Gas-discharge counter for radon progeny	Visual observations	8 months-3 years	110 km	[154]
Jiuzhaigou	7 (M_S)	08/08/2017	± 3 times	>2 months	SD-3 A, automatic radon instrument, Songpan station	Statistical analysis		67 km	[205]
Uglovoye Podnyatiye, Kamchatka Peninsula	7.3 (M_W)	20/12/2018	33-35 %		Gas-discharge counter for radon progeny	Visual observations	8 months-3 years	490 km	[154]
North Kurils, Kamchatka Peninsula	7.5 (M_W)	25/03/2020	33-35 %		Gas-discharge counter for radon progeny	Visual observations	8 months-3 years	449 km	[154]

Evaluating **Table 1** and **Table 2**, it can be supported that the majority of publications are based on visual observations of collected data and some extend of statistical analysis. This can be explained by the fact that both for historical and new earthquakes it is very difficult to collect data from at least one station nearby. As mentioned by Cicerone et al. [6], it is a serendipitous finding to have a strong earthquake and a station which collects data during the seismic rupture and is installed in the, generally mentioning, effective epicentre's area. As mentioned in several publications and expressed collectively in Eftaxias [176], there is no one to one correspondence between earthquake occurrence and anomaly detection. Moreover, even the most advanced methods do not manage to have a very effective forecasting of earthquakes. These facts complicate the analysis even today (2024).

The most advantageous methods seem nowadays to reflect the fractal and self organisation nature of the rupturing crust of the earth during preparation of earthquakes. Very robust method is the natural time analysis with has much more to give. The satellites are now several and can be accessed conveniently. This provides new insights in the related research. Remote sensing and SAR techniques are very powerful as well. Not omitting of course the number of installed stations worldwide. These new tools give boost to the modern approaches which are also multi-facet and with the collaboration of different groups.

Historically radon gas has the majority of publications in relation to earthquakes with many radon papers presenting associations with very strong earthquakes. Nowadays there is a balance between radon and electromagnetic precursors, with the latter to have more options due to the different frequency ranges and the remote sensing and satellite methods. Radon has also provided new approaches and therefore both precursors are very significant. In fact electromagnetic and radon precursors seem to be the subject of many papers up to date.

The collaboration between scientists and the multi level approaches with different methodologies is the key point to the seismic reasearch in the following years. This research is ongoing and in a continuous search for credible and powerful precursors.

8. Conclusions

This paper is a review on electromagnetic and radon precursors for earthquake forecasting. The electromagnetic precursors emerge in a diverse frequency band ranging from ultra low to very high frequencies. Nowadays electromagnetic data are collected from satellites, whereas the remote sensing techniques are in increasing usage also. Within the electromagnetic spectrum is also the TEC measurements and the modern approach of SAR studies. The various investigators are still working independently, nevertheless there is great space for inter-collaborations. The traditional approach is still the recordings from ground stations, with the precursors of the ULF range to have the greater history and potential. *MHz,KHz* frequencies provide also very good estimations. On the other hand, radon precursors are those with the oldest usage. Many great earthquakes have been studied with the help of radon stations worldwide. Radon is easily detected and may travel far due to its inert nature. For this reason it assist in forecasting of earthquakes from far.

The majority of the reported precursory anomalies have been and still are visually observed. Several statistical approaches have been utilised in the papers. Especially for radon, the $\pm 2\sigma$ criterion is the one most frequently used. In the recent years advanced methods have been published and used in several new publications. Special mention is in the modern approach of Natural Time which has great potential and many future earthquakes to be applied to. Power-law as well as Monofractal and Multifractal Detrended Fluctuation Analysis have been used in both electromagnetic and radon precursors. Usage has been done to *R/S* analysis, fractal dimension analysis and Hurst exponents. Block entropy and several entropy measures have been used as well. Combinational analysis between different monofractal methods has been used with success. All these modern methods attempt to outline the fractal and self organised critical features of the fracturing parts of the earth's crust during preparation of earthquakes. Much research needs to be implemented and new approaches are still on demand.

Several models have been proposed for the interpretation of the collected precursory data. The LAIC model has been in great use by many papers. The theory of asperities has been employed both in electromagnetic and radon precursors. In radon research other models have also been utilised. Since each earthquake is a special event it is difficult to find a universal model which covers all aspects of the research outcomes. The main problem is that many precursors have characterised so, after the occurrence of the earthquakes. This is a disadvantage that will be overcome as the research is progressing. There are papers that forecast earthquakes prior to their occurrence and this is still the most distinguishing issue. The work of researchers from different sub-disciplines of electromagnetic and radon precursors will provide better forecasting results in terms of science. **Author Contributions:**

Conceptualization, D.N. and E.P.; methodology, D.N. D.C. and E.P.; software, D.N., D.C., S.D., A.A. and E.P.; formal analysis, D.N. and D.C.; investigation, D.N. and E.P.; resources, D.N., A.A. and E.P.; data curation, D.N., A.A. and E.P.; writing-original draft preparation, D.N.; writing-review and editing, D.C., A.A. and E.P.; supervision, D.N.; project administration, D.N.

Funding: This research received no external funding

Informed Consent Statement: Not applicable

Data Availability Statement: Not applicable.

Conflicts of Interest: The authors declare no conflict of interest.

References

1. Keilis-Borok, V.I.; Soloviev, A.A. *Nonlinear Dynamics of the Lithosphere and Earthquake Forecast*; Springer: Heidelberg, 2003.
2. Keilis-Borok, V. Earthquake Forecast: State-of-the-Art and Emerging Possibilities. *Annual Review of Earth and Planetary Sciences* **2002**, *30*, 1–33.
3. Hayakawa, M.; Hobara, Y. Current status of seismo-electromagnetics for short-term earthquake prediction. *Geomatics, Natural Hazards and Risk* **2010**, *1*, 115–155. doi:http://dx.doi.org/10.1080/19475705.2010.486933.
4. Eftaxias, K.; Balasis, G.; Contoyiannis, Y.; Papadimitriou, C.; Kalimeri, M. Unfolding the procedure of characterizing recorded ultra low frequency, kHz and MHz electromagnetic anomalies prior to the L'Aquila earthquake as pre-seismic ones - Part 2. *NHESS* **2010**, *10*, 275–294. doi:http://dx.doi.org/10.5194/nheiss-9-1953-2009.
5. Nikolopoulos, D.; Petraki, E.; Marousaki, A.; Potirakis, S.; Koulouras, G.; Nomicos, C.; Panagiotaras, D.; Stonham, J.; Louizi, A. Environmental monitoring of radon in soil during a very seismically active period occurred in South West Greece. *J. Environ. Monit.* **2012**, *14*, 564–578.
6. Cicerone, R.; Ebel, J.; Britton, J. A systematic compilation of earthquake precursors. *Tectonophysics* **2009**, *476*, 371–396. doi:https://doi.org/10.1016/j.tecto.2009.06.008.
7. Molchanov, A.; Kopytenko, A.; Voronov, M.; Kopytenko, A.; Matiashvili, G.; Fraser-Smith, C.; Bernardi, A. Results of ULF magnetic field measurements near the epicenters of the Spitak (Ms= 6.9) and Loma-Prieta (Ms= 7.1) earthquakes: comparative analysis. *Geophys. Res. Lett.* **1992**, *19*, 1495–1498.
8. Conti, L.; Picozza, P.; Sotgiu, A. A Critical Review of Ground Based Observations of Earthquake Precursors. *Frontiers in Earth Science* **2021**, *9*. doi:10.3389/feart.2021.676766.
9. Shrivastava, A. Are pre-seismic ULF electromagnetic emissions considered as a reliable diagnostics for earthquake prediction? *Current Science* **2014**, *107*, 596–600.
10. Uyeda, S.; Nagao, T.; Kamogawa, M. Short-term earthquake prediction: Current status of seismo-electromagnetics. *Tectonophysics* **2009**, *470*, 205–213. doi:http://dx.doi.org/10.1016/j.tecto.2008.07.019.
11. Petraki, E.; Nikolopoulos, D.; Nomicos, C.; Stonham, J.; Cantzos, D.; others. Electromagnetic Pre-earthquake Precursors: Mechanisms, Data and Models-A Review. *J. Earth Sci. Clim. Change* **2015**, *6*, 1–11. doi:10.4172/2157-7617.1000250.
12. Aggarwal, P.; Sykes, R.; Simpson, W.; Richards, G. Spatial and temporal variations in ts/tp and in P wave residuals at Blue Mountain Lake, New York: Application to earthquake forecast. *Journal of Geophysical Research* **1975**, *80*, 718–732.
13. Parvaiz, K.; Sharad, T.; Azad, M.; Purushottam, B.; Purohit, P.; others. Scientific efforts in the direction of successful earthquake forecast. *International Journal of Geomatics and Geosciences* **2011**, *1*, 669–677.
14. Zong, J.; Tao, D.; Shen, X. Possible ELF/VLF Electric Field Disturbances Detected by Satellite CSES before Major Earthquakes. *Atmosphere* **2022**, *13*. doi:10.3390/atmos13091394.

15. Thomas, J.E.; Ekanem, A.M.; George, N.J.; Akpan, A.E. Ionospheric perturbations: a case study of 2007 five major earthquakes using DEMETER data. *Acta Geophysica* **2023**, *71*, 1607–1618.
16. Vesnin, A.; Yasyukevich, Y.; Perevalova, N.; Şentürk, E. Ionospheric Response to the 6 February 2023 Turkey&-Syria Earthquake. *Remote Sensing* **2023**, *15*. doi:10.3390/rs15092336.
17. Ghosh, D.; Deb, A.; Sengupta, R. Anomalous radon emission as precursor of earthquake. *J. Appl. Geophys.* **2009**, *187*, 245–258.
18. Zafrir, H.; Steinitz, G.; Malik, U.; Haquin, G.; Gazit-Yaari, N. Response of Radon in a seismic calibration explosion, Israel. *Radiat. Meas.* **2009**, *44*, 193–198.
19. Chyi, L.; Quick, T.; Yang, T.; Chen, C. Soil gas radon spectra and Earthquakes. *TAO* **2005**, *16*, 763–774.
20. Kuo, T.; Lin, C.; Fan, K.; Chang, G.; Lewis, C.; Han, Y.; Wu, Y.; Chen, W.; Tsai, C. Radon anomalies precursory to the 2003 Mw=6.8 Chengkung and 2006 Mw=6.1 Taitung earthquakes in Taiwan. *Radiat. Meas.* **2009**, *44*, 295–299.
21. Nikolopoulos, D.; Petraki, E.; Vogianis, E.; Chaldeos, Y.; Giannakopoulos, P.; Kottou, S.; Nomicos, C.; Stonham, J. Traces of self-organisation and long-range memory in variations of environmental radon in soil: Comparative results from monitoring in Lesbos Island and Ileia (Greece). *J. Radioanal. Nucl. Chem.* **2014**, *299*, 203–219.
22. Petraki, E.; Nikolopoulos, D.; Fotopoulos, A.; Panagiotaras, D.; Nomicos, C.; Yannakopoulos, P.; Kottou, S.; Zisos, A.; Louizi, A.; Stonham, J. Long-range memory patterns in variations of environmental radon in soil. *Anal. Methods* **2013**, *5*, 4010–4020.
23. Petraki, E.; Nikolopoulos, D.; Fotopoulos, A.; Panagiotaras, D.; Koulouras, G.; Zisos, A.; Nomicos, C.; Louizi, A.; Stonham, J. Self-organised critical features in soil radon and MHz electromagnetic disturbances: Results from environmental monitoring in Greece. *Appl. Radiat. Isotop.* **2013**, *72*, 39–53.
24. Singh, S.; Kumar, A.; Singh, B.B.; Mahajan, S.; Kumar, V.; Dhar, S. Radon Monitoring in Soil Gas and Ground Water for Earthquake Prediction Studies in North West Himalayas, India. *Terr. Atmos. Ocean Sci.* **2010**, *21*, 685–690.
25. Singh, M.; Ramola, R.; Singh, B.; Sing, S.; Virk, H. Subsurface soil gas radon changes associated to earthquakes. *Nucl. Tracks Radiat. Meas.* **1991**, *19*, 417–420.
26. Nazaroff, W.; Nero, A. *Radon and its Decay Products in Indoor Air*; John Wiley & Sons Inc.: New York, 1988.
27. Richon, P.; Bernard, P.; Labed, V.; Sabroux, J.; Beneito, A.; Lucius, D.; Abbad, S.; Robe, M. Results of monitoring ²²²Rn in soil gas of the Gulf of Corinth region, Greece. *Radiat. Meas.* **2007**, *42*, 87–93.
28. Erees, F.; Aytas, S.; Sac, M.; Yener, G.; Salk, M. Radon concentrations in thermal waters related to seismic events along faults in the Denizli Basin, Western Turkey. *Radiat. Meas.* **2007**, *42*, 80–86. doi:https://doi.org/10.1016/j.radmeas.2006.06.003.
29. Yasuoka, Y.; Igarashi, G.; Ishikawa, T.; Tokonami, S.; Shinogi, M. Evidence of precursor phenomena in the Kobe earthquake obtained from atmospheric radon concentration. *Appl. Geochem.* **2006**, *21*, 1064–1072.
30. Namvaran, M.; Negarestani, A. Measuring the radon concentration and investigating the mechanism of decline prior an earthquake (Jooshan, SE of Iran). *J. Radioanal. Nucl. Chem.* **2012**. doi:10.1007/s10967-012-2162-7.
31. Zoran, M.; Savastru, R.; Savastru, D.; Chitaru, C.; Baschir, L.; Tautan, M. Monitoring of radon anomalies in South-Eastern part of Romania for earthquake surveillance. *J. Radioanal. Nucl. Chem.* **2012**, *293*, 769–781.
32. Nikolopoulos, D.; Petraki, E.; Nomicos, C.; Koulouras, G.; Kottou, S.; Yannakopoulos, P.H. Long-Memory Trends in Disturbances of Radon in Soil Prior ML=5.1 Earthquakes of 17 November 2014 Greece. *J. Earth Sci. Clim. Change* **2015**, *6*, 1–11.
33. Nikolopoulos, D.; Valais, I.; Michail, C.; Bakas, A.; Fountzoula, C.; Cantzos, D.; Bhattacharyya, D.; Sianoudis, I.; Fountos, G.; Yannakopoulos, P.H.; Panayiotakis, G.; Kandarakis, I. Radioluminescence properties of the CdSe/ZnS Quantum Dot nanocrystals with analysis of long-memory trends. *Radiat. Meas.* **2016**, *92*, 19–31.
34. Nikolopoulos, D.; Petraki, E.; Yannakopoulos, P.H.; Priniotakis, G.; Voyiatzis, I.; Cantzos, D. Long-lasting patterns in 3 kHz electromagnetic time series after the ML= 6.6 earthquake of 2018-10-25 near Zakynthos, Greece. *Geosciences* **2020**, *10*, 235. doi:https://doi.org/10.3390/geosciences10060235.
35. Nikolopoulos, D.; Petraki, E.; Rafique, M.; Alam, A.; Cantzos, D.; Yannakopoulos, P. Fractal Features in kHz Electromagnetic Observations Preceding Near-Field Earthquakes in Ilia, Greece. *Geosciences* **2023**, *13*. doi:10.3390/geosciences13120387.

36. Alam, A.; Nikolopoulos, D.; Wang, N. Fractal Patterns in Groundwater Radon Disturbances Prior to the Great 7.9 Mw Wenchuan Earthquake, China. *Geosciences* **2023**, *13*.
37. Pulinet, S.; Ouzounov, D. Lithosphere–Atmosphere–Ionosphere Coupling (LAIC) model – An unified concept for earthquake precursors validation. *J. Asian Earth Sci.* **2011**, *41*, 371–382. Validation of Earthquake Precursors-VESTO, doi:https://doi.org/10.1016/j.jseae.2010.03.005.
38. Calais, E.; Haase, J.S.; Minster, J.B. Detection of ionospheric perturbations using a dense GPS array in Southern California. *Geophys. Res. Lett.* **2003**, *30*. doi:https://doi.org/10.1029/2003GL017708.
39. Liu, J.Y.; Chen, Y.I.; Chen, C.H.; Liu, C.Y.; Chen, C.Y.; Nishihashi, M.; Li, J.Z.; Xia, Y.Q.; Oyama, K.I.; Hattori, K.; Lin, C.H. Seismoionospheric GPS total electron content anomalies observed before the 12 May 2008 Mw7.9 Wenchuan earthquake. *J. Geophys. Res. Space Phys.* **2009**, *114*. doi:https://doi.org/10.1029/2008JA013698.
40. Liu, X.; Yuan, Y.; Tan, B.; Li, M. Observational Analysis of Variation Characteristics of GPS-Based TEC Fluctuation over China. *ISPRS International Journal of Geo-Information* **2016**, *5*. doi:10.3390/ijgi5120237.
41. Sharma, G.; Saikia, P.; Walia, D.; Banerjee, P.; Raju, P. TEC anomalies assessment for earthquakes precursors in North-Eastern India and adjoining region using GPS data acquired during 2012–2018. *Quaternary International* **2021**, *575–576*, 120–129. doi:https://doi.org/10.1016/j.quaint.2020.07.009.
42. Klimenko, M.; Klimenko, V.; Zakharenkova, I.; Cherniak, I. The global morphology of the plasmaspheric electron content during Northern winter 2009 based on GPS/COSMIC observation and GSM TIP model results. *ASR* **2015**, *55*, 2077–2085. doi:https://doi.org/10.1016/j.asr.2014.06.027.
43. Gokhberg, M.B.; Morgounov, V.A.; Yoshino, T.; Tomizawa, I. Experimental measurement of electromagnetic emissions possibly related to earthquakes in Japan. *J. Geophys. Res. Space Phys.* **1982**, *87*, 7824–7828. doi:https://doi.org/10.1029/JB087iB09p07824.
44. Gufeld, I.L.; Rozhnoi, A.A.; Tyumensev, S.N.; Sherstuk, S.V.; Yampolsky, V.S. Radiowave disturbances in period to Rudber and Rachinsk earthquakes. *Phys. Solid Earth* **1992**, *28*, 267–270.
45. Molchanov, O.A.; Hayakawa, M. Subionospheric VLF signal perturbations possibly related to earthquakes. *J. Geophys. Res. Space Phys.* **1998**, *103*, 17489–17504.
46. Muto, F.; Yoshida, M.; Horie, T.; Hayakawa, M.; Parrot, M.; Molchanov, O.A. Detection of ionospheric perturbations associated with Japanese earthquakes on the basis of reception of LF transmitter signals on the satellite DEMETER. *NHESS* **2008**, *8*, 135–141. doi:10.5194/nhess-8-135-2008.
47. Rozhnoi, A.; Shalimov, S.; Solovieva, M.; Levin, B.; Hayakawa, M.; Walker, S. Tsunami-induced phase and amplitude perturbations of subionospheric VLF signals. *J. Geophys. Res. Space Phys.* **2012**, *117*. doi:https://doi.org/10.1029/2012JA017761.
48. Whitehead, N.; Barry, B.; Ditchburn, R.; Morris, C.; Stewart, M. Systematics of radon at the Wairakei geothermal region, New Zealand. *J. Environ. Radioactiv.* **2007**, *92*, 16–29.
49. King, C. Radon Emanation on San Andreas Fault. *Nature* **1978**, *271*, 516–519.
50. King, C. Impulsive radon emanation on a creeping segment of the San Andreas fault, California. *Pure Appl. Geophys.* **1985**, *122*, 340–352.
51. Tansi, C.; Tallarico, A.; Iovine, G.; Gallo, M.F.; Falcone, G. Interpretation of radon anomalies in seismo-tectonic and tectonic-gravitational settings: the south-eastern Crati graben (Northern Calabria, Italy). *Tectonophysics* **2005**, *396*, 181–193.
52. Walia, V.; Yang, T.; Hong, W.; Lin, S.; Fu, C.; Wen, K.; Chen, C. Geochemical variation of soil-gas composition for fault trace and earthquake precursory studies along the Hsincheng fault in NW Taiwan. *Appl. Radiat. Isot.* **2009**, *67*, 1855–1863.
53. Immé, G.; Delf, S.L.; Nigro, S.L.; Morelli, D.; Patané, G. Gas radon emission related to geodynamic activity on Mt. Etna. *Ann. Geophys.* **2005**, *48*, 65–71.
54. Morelli, D.; Martino, S.D.; Immé, G.; Delfa, S.L.; Nigro, S.L.; Patané, G. Evidence of soil Radon as a tracer of magma uprising in Mt.Etna. *Radiat. Meas.* **2006**, *41*, 721–725.
55. Ghosh, D.; Deb, A.; Dutta, S.; Sengupta, R. Multifractality of radon concentration fluctuation in earthquake related signal. *Fractals* **2012**, *20*, 33–39.
56. Majumdar, K. A study of fluctuation in radon concentration behaviour as an earthquake precursor. *Curr. Sci. India* **2004**, *86*, 1288–1292.
57. Moore, G.W. Magnetic disturbances preceding the 1964 Alaska earthquake. *Nature* **1964**, *203*, 508–509.

58. Fraser-Smith, A.C.; Bernardi, A.; McGill, P.R.; Ladd, M.E.; Helliwell, R.A.; Villard, O.G. Low-frequency magnetic field measurements near the epicenter of the Ms 7.1 Loma Prieta Earthquake. *Geophys. Res. Lett.* **1990**, *17*, 1465–1468.
59. Hayakawa, M.; Kawate, R.; Molchanov, O.; Yumoto, K. Results of ultra-low-frequency magnetic field measurements during the Guam earthquake of 8 August 1993. *Geophys. Res. Lett.* **1996**, *23*, 241–244.
60. Hayakawa, M.; Ito, T.; Smirnova, N. Fractal analysis of ULF geomagnetic data associated with the Guam Earthquake on August 8, 1993. *Geophys. Res. Lett.* **1999**, *26*, 2797–2800. doi:10.1029/1999GL005367.
61. Varotsos, P.; Alexopoulos, K. Physical properties of the variations of the electric field of the earth preceding earthquakes, I. *Tectonophysics* **1984**, *110*, 73–98.
62. Varotsos, P.; Alexopoulos, K. Physical properties of the variations of the electric field of the earth preceding earthquakes, II. *Tectonophysics* **1984**, *110*, 99–125.
63. Swati.; Singh, B.; Pundhir, D.; Hobara, Y. Fractal analysis of Ultra Low Frequency magnetic field emissions observed at Agra associated with two major earthquakes occurred in Pakistan. *Journal of Atmospheric Electricity* **2020**, *39*, 1–15. doi:10.1541/jae.39.1.
64. Varotsos, P.A.; Sarlis, N.V.; Skordas, E.S.; Nagao, T.; Kamogawa, M.; Flores-Márquez, E.L.; Ramírez-Rojas, A.; Perez-Oregon, J. Improving the Estimation of the Occurrence Time of an Impending Major Earthquake Using the Entropy Change of Seismicity in Natural Time Analysis. *Geosciences* **2023**, *13*. doi:10.3390/geosciences13080222.
65. Kopytenko, Y.A.; Matiashvili, T.G.; Voronov, P.M.; Kopytenko, E.A.; Molchanov, O.A. Detection of Ultra-low-frequency Emissions Connected with the Spitak Earthquake and its Aftershock Activity, Based on Geomagnetic Pulsations Data at Dusheti and Vardzia Observatories. *Phys. Earth Planet. Interiors* **1993**, *77*, 85–95. doi:10.1016/0031-9201(93)90035-8.
66. Du, A.; Huang, Q.; Yang, S. Epicenter location by abnormal ULF electromagnetic emissions. *Geophys. Res. Lett.* **2002**, *29*, 1455. doi:10.1029/2001GL013616.
67. Hattori, K. ULF magnetic anomaly preceding the 1997 Kagoshima earthquakes. *Seismo Electromagnetics, Lithosphere-Atmosphere-Ionosphere Coupling* **2002**, pp. 19–28.
68. Hattori, K.; Serita, A.; Yoshino, C.; Hayakawa, M.; Isezaki, N. Singular spectral analysis and principal component analysis for signal discrimination of ULF geomagnetic data associated with 2000 Izu Island Earthquake Swarm. *Phys. Chem. Earth* **2006**, *31*, 281–291. doi:10.1016/j.pce.2006.02.034.
69. Hattori, K.; Han, P.; Yoshino, C.; Febriani, F.; Yamaguchi, H.; Chen, C.H. Investigation of ULF Seismo-Magnetic Phenomena in Kanto, Japan During 2000–2010: Case Studies and Statistical Studies. *Surveys in Geophysics* **2013**, *34*, 293–316. doi:10.1007/s10712-012-9215-x.
70. Han, P.; Hattori, K.; Hirokawa, M.; Zhuang, J.; Chen, C.H.; Febriani, F.; Yamaguchi, H.; Yoshino, C.; Liu, J.Y.; Yoshida, S. Statistical analysis of ULF seismomagnetic phenomena at Kakioka, Japan, during 2001–2010. *J. Geophys. Res. Space Phys.* **2014**, *119*, 4998–5011. doi:https://doi.org/10.1002/2014JA019789.
71. Han, P.; Hattori, K.; Xu, G.; Ashida, R.; Chen, C.H.; Febriani, F.; Yamaguchi, H. Further investigations of geomagnetic diurnal variations associated with the 2011 off the Pacific coast of Tohoku earthquake (Mw 9.0). *J. Asian Earth Sci.* **2015**, *114*, 321–326. doi:10.1016/j.jseas.2015.02.022.
72. Xu, G.; Han, P.; Huang, Q.; Hattori, K.; Febriani, F.; Yamaguchi, H. Anomalous behaviors of geomagnetic diurnal variations prior to the 2011 off the Pacific coast of Tohoku earthquake (Mw9.0). *J. Asian Earth Sci.* **2013**, *77*, 59–65. doi:10.1016/j.jseas.2013.08.011.
73. Hayakawa, M.; Rozhnoi, A.; Solovieva, M.; Hobara, Y.; Ohta, K.; Schekotov, A.; Fedorov, E. The lower ionospheric perturbation as a precursor to the 11 March 2011 Japan earthquake. *Geom. Nat. Haz. Risk* **2013**, *4*, 275–287. doi:10.1080/19475705.2012.751938.
74. Nagao, T.; Orihara, Y.; Kamogawa, M. Precursory phenomena possibly related to the 2011 M9.0 off the Pacific coast of Tohoku earthquake. *J. Disaster Res* **2014**, *9*, 303–310.
75. Ouzounov, D.; Pulinets, S.; Romanov, A.; Romanov, A.; Tsybulya, K.; Davidenko, D.K.M.; Taylor, P. Atmosphere-ionosphere response to the M9 Tohoku earthquake revealed by multi-instrument spaceborne and ground observations: Preliminary results. *Earth Sci.* **2011**, *24*, 557–564.
76. Sarlis, N.; Skordas, E.; Varotsos, P.; Nagao, T.; Kamogawa, M.; Tanaka, H.; Uyeda, S. Minimum of the order parameter fluctuations of seismicity before major earthquake in Japan. *Proc. Natl. Acad. Sci. USA* **2013**, *110*, 13734–13738. doi:10.1073/pnas.1312740110.

77. Stanica, D.A.; Stanica, D.; Vladimirescu, N. Long-range anomalous electromagnetic effect related to M9 Great Tohoku earth- quake. *Earth Sci.* **2015**, *4*, 31–38.
78. Stanica, D.A.; Stanica, D.; Blecki, J.; Ernst, T.; Jozwiak, W.; Slominski, J. Pre-seismic geomagnetic and ionosphere signatures related to the Mw5.7 earthquake occurred in Vrancea zone on September 24. 2016. *Acta Geophys* **2018**, *66*, 167–177. doi:10.1007/s11600-018-0115-4.
79. Stanica, D.A.; Stanica, D.; Valeca, M.; Iordache, S. Electromagnetic contribution to the resilience improvement against the Vrancea intermediate depth earthquakes, Romania. *Ann. Geophys* **2020**, *63*, 551. doi:10.4401/ag-8096.
80. Hirano, T.; Hattori, K. ULF geomagnetic changes possibly associated with the 2008 Iwate–Miyagi Nairiku earthquake. *Journal of Asian Earth Science* **2011**, *41*, 442–449. doi:https://doi.org/10.1016/j.jseaes.2010.04.038.
81. Ouyang, X.; Liu, W.; Xiao, Z.; Hao, Y. Observations of ULF waves on the ground and ionospheric Doppler shifts during storm sudden commencement. *J. Geophys. Res. Space Phys.* **2016**, *121*, 2976–2983.
82. Eftaxias, K.; Balasis, G.; Contoyiannis, Y.; Papadimitriou, C.; Kalimeri, M.; Athanasopoulou, L.; Nikolopoulos, S.; Kopanas, J.; Antonopoulos, G.; Nomicos, C. Unfolding the procedure of characterizing recorded ultra low frequency, kHz and MHz electromagnetic anomalies prior to the L'Aquila earthquake as pre-seismic ones-Part 1. *NHESS* **2009**, *9*, 1953–1971.
83. Eftaxias, K.; Contoyiannis, Y.; Balasis, G.; Karamanos, K.; Kopanas, J.; Antonopoulos, G.; Koulouras, G.; Nomicos, C. Evidence of fractional-Brownian-motion-type asperity model for earthquake generation in candidate pre-seismic electromagnetic emissions. *NHESS* **2008**, *8*, 657–669.
84. Kapisir, P.; Peratzakis, J.P.A.; Nomikos, K.; K.Eftaxias. VHF-electromagnetic evidence of the underlying pre-seismic critical stage. *Earth Plan. Space* **2002**, *54*, 1237–1246.
85. Kapisir, P.; Eftaxias, K.; Nomikos, K.; Polygiannakis, J.; Dologlou, E.; Balasis, G.; Bogris, N.; Peratzakis, A.; Hadjicontis, V. Evolving towards a critical point: A possible electromagnetic way in which the critical regime is reached as the rupture approaches. *Nonlinear Proc. Geoph.* **2003**, *10*, 1–14.
86. Petraki, E. Electromagnetic Radiation and Radon-222 Gas Emissions as Precursors of Seismic Activity. PhD thesis, Department of Electronic and Computer Engineering, Brunel University London, UK, 2016.
87. Stavrakas, I.; Clarke, M.; Koulouras, G.; Stavrakakis, G.; Nomicos, C. Study of directivity effect on electromagnetic emissions in the HF band as earthquake precursors: Preliminary results on field observations. *Tectonophysics* **2007**, *431*, 263–271.
88. Contoyiannis, Y.; Kapisir, P.; Eftaxias, K. Monitoring of a preseismic phase from its electromagnetic precursors. *Phys. Rev. E* **2005**, *71*, 1–14.
89. Eftaxias, K.; Panin, V.; Deryugin, Y. Evolution-EM signals before earthquakes in terms of mesomechanics and complexity. *Phys. Chem. Earth*, *29*, 445–451.
90. K. Eftaxias, V. Sgrigna, T.C. Mechanical and electromagnetic phenomena accompanying preseismic deformation: From laboratory to geophysical scale. *Tectonophysics* **2007**, *341*, 1–5.
91. Contoyiannis, Y.; Eftaxias, K. Tsallis and Levy statistics in the preparation of an earthquake. *Nonlin. Processes Geophys.* **2008**, *15*, 379–388.
92. Petraki, E.; Nikolopoulos, D.; Chaldeos, Y.; Koulouras, G.; Nomicos, C.; Yannakopoulos, P.H.; Kottou, S.; Stonham, J. Fractal evolution of MHz electromagnetic signals prior to earthquakes: results collected in Greece during 2009. *Geom., Nat.Hazard Risk* **2016**, *7*, 550–564.
93. Sorokin, V.; Novikov, V. Possible Interrelations of Space Weather and Seismic Activity: An Implication for Earthquake Forecast. *Geosciences* **2024**, *14*. doi:10.3390/geosciences14050116.
94. Anagnostopoulos, G.; Spyroglou, I.; Rigas, A.; others. The sun as a significant agent provoking earthquakes. *Eur. Phys. J. Spec. Top.* **2021**, *230*, 287–333. doi:10.1140/epjst/e2020-000266-2.
95. Pulinets, S.; Ouzounov, D.; Karelin, A.; Boyarchuk, K., Multiparameter Approach and LAIC Validation. In *Earthquake Precursors in the Atmosphere and Ionosphere: New Concepts*; Springer Netherlands: Dordrecht, 2022; pp. 187–247. doi:10.1007/978-94-024-2172-9_4.
96. Sorokin, V.M.; Chmyrev, V.M.; Hayakawa, M. A Review on Electrodynamical Influence of Atmospheric Processes to the Ionosphere. *Open Journal of Earthquake Research* **2020**, *9*, 113–141. doi:10.4236/ojer.2020.92008.
97. Ouzounov, D.; Velichkova, S.; Botev, E. Modulation in VHF Wireless Signals Associated With Preearthquake Processes. Case Studies for the Balkans. *European Association of Geoscientists & Amplifier Engineers* **2021**, *2021*, 1–5. doi:https://doi.org/10.3997/2214-4609.202149BGS66.

98. Suárez, G.; Espinosa-Aranda, J.; Cuéllar, A.; Ibarrola, G.; García, A.; Zavala, M.; Maldonado, S.; Islas, R. A dedicated seismic early warning network: The Mexican Seismic Alert System (SASMEX). *Seismol. Res. Lett.* **2018**, *89*, 382–391.
99. Moriya, T.; Mogi, T.; Takada, M. Anomalous pre-seismic transmission of VHF-band radio waves resulting from large earthquakes, and its statistical relationship to magnitude of impending earthquakes. *Geophysical Journal International* **2010**, *180*, 858–870.
100. Devi, M.; Barbara, A.K.; Ruzhin, Y.Y.; Hayakawa, M. Over-the- Horizon Anomalous VHF Propagation and Earthquake Precursors. *Surv. Geophys.* **2012**, *33*, 1081–1106. doi:10.1007/s10712-012-9185-z.
101. Erickson, W.C. Radio noise near the Earth in the 1 - 30 MHz frequency range. In *Low frequency Astrophysics from Space*; Springer, 1990; pp. 57–69.
102. Eftaxias, K.; Kaporis, P.; Polygiannakis, J.; Peratzakis, A.; Kopanas, J.; Antonopoulos, G.; Rigas, D. Experience of short term earthquake precursors with VLF–VHF electromagnetic emissions. *NHESS* **2003**, *3*, 217–228. doi:10.5194/nheiss-3-217-2003.
103. Muhammad, S.; Tian, L. Mass balance and a glacier surge of Guliya ice cap in the western Kunlun Shan between 2005 and 2015. *Remote Sensing of Environment* **2020**, *244*, 111832. doi:https://doi.org/10.1016/j.rse.2020.111832.
104. Muhammad, S.; Thapa, A. Daily Terra–Aqua MODIS cloud-free snow and Randolph Glacier Inventory 6.0 combined product (M*D10A1GL06) for high-mountain Asia between 2002 and 2019. *Earth System Science Data* **2021**, *13*, 767–776. doi:10.5194/essd-13-767-2021.
105. Gul, J.; Muhammad, S.; Liu, S.y.; Ullah, S.; Ahmad, S.; Hayat, H.; Tahir, A.A. Spatio-temporal changes in the six major glaciers of the Chitral River basin (Hindukush Region of Pakistan) between 2001 and 2018. *Journal of Mountain Science* **2020**, *17*, 572–587. doi:10.1007/s11629-019-5728-9.
106. Hassan, J.; Chen, X.; Muhammad, S.; Bazai, N.A. Rock glacier inventory, permafrost probability distribution modeling and associated hazards in the Hunza River Basin, Western Karakoram, Pakistan. *Sci. Total Environ.* **2021**, *782*, 30. doi:10.1016/j.scitotenv.2021.146833.
107. Tian, L.; Yao, T.; Gao, Y.; Thompson, L.; Mosley-Thompson, E.; Muhammad, S.; Zong, J.; Wang, C.; Jin, S.; Li, Z. Two glaciers collapse in western Tibet. *J Glaciol.* **2017**, *63*, 194–197.
108. Khan, M.Y.; Turab, S.A.; Ali, L.; Shah, M.T.; Qadri, S.T.; Latif, K.; Kanli, A.I.; Akhter, M.G. The dynamic response of coseismic liquefaction-induced ruptures associated with the 2019 M w 5.8 Mirpur, Pakistan, earthquake using HVSR measurements. *Leading Edge.* **2021**, *40*, 590–600.
109. Mahmood, I.; Qureshi, S.N.; Tariq, S.; Atique, L.; Iqbal, M.F. Analysis of Landslides Triggered by October 2005, Kashmir Earthquake. *PLoS Curr* **2015**, *7*. PMID: 26366324, doi:10.1371/currents.dis.0bc3ebc5b8adf5c7fe9fd3d702d44a99.
110. Nath, B.; Singh, R.P.; Gahalaut, V.K.; Singh, A.P. Dynamic Relationship Study between the Observed Seismicity and Spatiotemporal Pattern of Lineament Changes in Palghar, North Maharashtra (India). *Remote Sensing* **2022**, *14*. doi:10.3390/rs14010135.
111. Kiseleva, E.; Mikhailov, V.; Smolyaninova, E.; Dmitriev, P.; Golubev, V.; Timoshkina, E.; Hooper, A.; Samiei-Esfahany, S.; Hanssen, R. PS-InSAR Monitoring of Landslide Activity in the Black Sea Coast of the Caucasus. *Procedia Technology* **2014**, *16*, 404–413. doi:https://doi.org/10.1016/j.protcy.2014.10.106.
112. Lin, C.H.; Liu, D.; Liu, G. Landslide detection in La Paz City (Bolivia) based on time series analysis of InSAR data. *Int. J. Remote Sens.* **2019**, *40*, 6775 – 6795.
113. Fiorentini, N.; Maboudi, M.; Leandri, P.; Losa, M.; Gerke, M. Surface Motion Prediction and Mapping for Road Infrastructures Management by PS-InSAR Measurements and Machine Learning Algorithms. *Remote Sensing* **2020**, *12*. doi:10.3390/rs12233976.
114. Saralioglu, E. Mapping surface deformation using SNAP-StaMPS after Seferhisar-Izmir earthquake. *Nat.Hazards* **2022**, *111*, 687–708.
115. Lapenna, V.; Lorenzo, P.; Perrone, A.; Piscitelli, S.; Sdao, F.; Rizzo, E. High-resolution geoelectrical tomographies in the study of Giarossa landslide. *southern Italy). Bull. Eng. Geol. Environ.* **2003**, *62*, 259–268.
116. Khan, M.Y.; Rehman, K.; Wajid, A.; Turab, S.A.; Latif, K.; Iqbal, S. Characterization of Ground Penetrating Radar (GPR) wave response in shallow subsurface for forensic investigation in controlled environment. *J. Himalayan Earth Sci.* **2019**, *52*, 58.
117. Khan, M.Y.; Shafique, M.; Turab, S.A.; Ahmad, N. Characterization of an unstable slope using geophysical, UAV, and geological techniques: Karakoram Himalaya, Northern Pakistan. *Front. Earth Sci.* **2021**, *9*, 668011.
118. Schwarz, B.; Krawczyk, C.M. Coherent diffraction imaging for enhanced fault and fracture network characterization. *Solid Earth.* **2020**, *11*, 1891–1907.

119. Hu, Z.; Shan, W. Landslide investigations in the northwest section of the lesser Khingan range in China using combined HDR and GPR methods. *Bull. Eng. Geol. Environ.* **2016**, *75*, 591.
120. Baradello, L.; Accaino, F. GPR and high resolution seismic integrated methods to understand the liquefaction phenomena in the Mirabello Village earthquake earthquake (ML 5.9) 2012. *Eng. Geol.* **2016**, *5*, 1–6.
121. Liu, L.; Li, Y. Identification of liquefaction and deformation features using ground penetrating radar in the New Madrid seismic zone, USA. *Journal of Applied Geophysics* **2001**, *47*, 199–215.
122. Yadav, K.S.; Vadnathani, R.B.; Goswami, K.R.; Patel, P.M. Anomalous Variations in Ionosphere TEC Before the Earthquakes of 2021 in the Different Parts of the Globe. *Trends in Sciences* **2023**, *20*, 5169. doi:10.48048/tis.2023.5169.
123. Muhammad, A.; K ulahcı, F.; Birel, S. Investigating radon and TEC anomalies relative to earthquakes via AI models. *Journal of Atmospheric and Solar-Terrestrial Physics* **2023**, *245*, 106037. doi:https://doi.org/10.1016/j.jastp.2023.106037.
124. Arikan, F.; Arikan, O.; Erol, C.B. Regularized estimation of TEC from GPS data for certain midlatitude stations and comparison with the IRI model. *ASR* **2007**, *39*, 867–874. doi:https://doi.org/10.1016/j.asr.2007.01.082.
125. Arikan, F.; Deviren, M.N.; O. Lenk, a.U.S.; Arikan, O. Observed Ionospheric Effects of 23 October 2011 Van, Turkey Earthquake. *Geom. Nat. Haz. Risk* **2012**, *3*, 1–8. doi:10.1080/19475705.2011.638027.
126. Gulyaeva, T.; Arikan, F. Statistical discrimination of global post-seismic ionosphere effects under geomagnetic quiet and storm conditions. *Geom. Nat. Haz. Risk* **2017**, *8*, 509–524. doi:10.1080/19475705.2016.1246483.
127. Tuna, H.; Arikan, O.; Arikan, F. Model based Computerized Ionospheric Tomography in space and time. *ASR* **2018**, *61*, 2057–2073. doi:https://doi.org/10.1016/j.asr.2018.01.031.
128. Sotomayor Beltran, C. *Ionospheric disturbances before and after the january 14, 2018 earthquake in Peru*; Academy of Sciences of the Czech Republic, 2019.
129. Liu, J.Y.; Chuo, Y.J.; Shan, S.J.; Tsai, Y.B.; Chen, Y.I.; Pulinets, S.A.; Yu, S.B. Pre-earthquake ionospheric anomalies registered by continuous GPS TEC measurements. *Annales Geophysicae* **2004**, *22*, 1585–1593. doi:10.5194/angeo-22-1585-2004.
130. Liu, J.Y.; Le, H.; Chen, Y.I.; Chen, C.H.; Liu, L.; Wan, W.; Su, Y.Z.; Sun, Y.Y.; Lin, C.H.; Chen, M.Q. Observations and simulations of seismoionospheric GPS total electron content anomalies before the 12 January 2010 M7 Haiti earthquake. *J. Geophys. Res. Space Phys.* **2011**, *116*. doi:https://doi.org/10.1029/2010JA015704.
131. Sharma, G.; Champati ray, P.; Mohanty, S.; Kannaujiya, S. Ionospheric TEC modelling for earthquakes precursors from GNSS data. *Quaternary International* **2017**, *462*, 65–74. doi:https://doi.org/10.1016/j.quaint.2017.05.007.
132. Ghafar, M.M.; Salh, H.; K ulahcı, F. Investigation of Radon, Total Electron Content and Linear and Nonlinear Variations of Meteorological Variables Due to Earthquakes: ARIMA and Monte Carlo Modelling. *Turkish Journal of Science and Technology* **2024**, *19*, 73–86.
133. Keskin, S.; K ulahcı, F. ARIMA model simulation for total electron content, earthquake and radon relationship identification. *Nat. Hazards* **2023**, *115*, 1955–1976.
134. Mohammed, D.H.K.; K ulahcı, F.; Alalı, A.S. Evaluation of the Effects of Earthquakes on Radon and Total Electron Content Values and Meteorological Changes on the North Anatolian Fault Zone, T rkiye. *Turkish Journal of Science and Technology* **2023**, *18*, 75–85.
135. Zhao, B.; Wang, M.; Yu, T.; Wan, W.; Lei, J.; Liu, L.; Ning, B. Is an unusual large enhancement of ionospheric electron density linked with the 2008 great Wenchuan earthquake? *J. Geophys. Res. Space Phys.* **2008**, *113*.
136. Ondoh, T. Seismo-ionospheric phenomena. *ASR* **2000**, *26*, 1267–1272.
137. Freeshah, M.A.; Zhang, X.; Chen, J.; Zhao, Z.; Osama, N.; Sadek, M.; Twumasi, N. Detecting ionospheric TEC disturbances by three methods of detrending through dense CORS during a strong thunderstorm. *Ann. Geophys* **2020**, *63*, GD667.
138. Toman, I.; Br    , D.; Kos, S. Contribution to the research of the effects of Etna volcano activity on the features of the ionospheric total electron content behaviour. *Remote sensing* **2021**, *13*, 1006.
139. Singh, V.; Chauhan, V.; Singh, O.P.; Singh, B. Ionospheric effect of earthquakes as determined from ground based TEC measurement and satellite data. *Indian J. Radio Space Phys* **2010**, *39*, 63–70.
140. Efstratios, V.; Dimitrios, N. Radon sources and associated risk in terms of exposure and dose. *Frontiers in public health* **2015**, *2*, 93477.
141. Nikolopoulos, D.; Louizi, A. Study of indoor radon and radon in drinking water in Greece and Cyprus: Implications to exposure and dose. *Radiat. Meas.* **2008**, *43*, 1305–1314. doi:https://doi.org/10.1016/j.radmeas.2008.03.043.

142. Organization, W.H. *WHO handbook on indoor radon: a public health perspective*, (2009); World Health Organization, 2009.
143. WHO. (World Health Organization), *Radon and health*, (2015); World Health Organization, 2015.
144. WHO. (World Health Organization), *Radon and Health*. (2023); World Health Organization, 2023.
145. Organization, W.H. (World Health Organization), *Radon and its effects on health*, (2004); World Health Organization, 2009.
146. Rahman, S.; Rafique, M.; Anwar, J.; others. Radon measurement studies in workplace buildings of the Rawalpindi region and Islamabad Capital area, Pakistan. *Building and environment* **2010**, *45*, 421–426.
147. Rafique, M.; Matiullah, R.S.; Rahman, S.; Shahzad, M.I.; Azam, B.; Ahmad, A.; Majid, A.; Siddique, M.I. Assessment of indoor radon doses received by dwellers of Balakot-NWFP Pakistan: a pilot study. *Carpathian J Earth Environ Sci* **2011**, *6*, 133–140.
148. Rafique, M.; Iqbal, J.; Shah, S.A.A.; Alam, A.; Lone, K.J.; Barkat, A.; Shah, M.A.; Qureshi, S.A.; Nikolopoulos, D. On fractal dimensions of soil radon gas time series. *Journal of Atmospheric and Solar-Terrestrial Physics* **2022**, *227*, 105775. doi:10.1016/j.jastp.2021.105775.
149. Nasir, T.; Rafique, M.; Rahman, S.U.; Khalil, M.; Anwar, N. Evaluation of radon induced lung cancer risk in occupants of the old and new dwellings of the Dera Ismail Khan City, Pakistan. *Journal of Radio-analytical and Nuclear Chemistry* **2014**, *300*, 1209–1215.
150. Kearfott, K.J.; Whetstone, Z.D.; Rafique, M. Use of a geographic information system (GIS) for targeting radon screening programs in South Dakota. *Journal of radiation research* **2016**, *57*, 84–90.
151. Dempsey, S.; Lyons, S.; Nolan, A. High Radon Areas and Lung Cancer Prevalence: Evidence from Ireland. *J. Environ. Radioact.* **2017**, *182*, Epub., 12–19. doi:10.1016/j.jenvrad.2017.11.014.
152. Sukanya, S.; Jacob, N.; Sabu, J. Application of radon (²²²Rn) as an environmental tracer in hydrogeological and geological investigations: An overview. *Chemosphere* **2022**, *303*, 135141. doi:10.1016/j.chemosphere.2022.135141.
153. Tareen, A.D.K.; Asim, K.M.; Kearfott, K.J.; Rafique, M.; Nadeem, M.S.A.; Talat, I.; Mir, A.A.; Çelebi, F.V.; Alsolai, H.; Qureshi, S.A.; Rafique, M.; Alzahrani, J.S.; Mahgoub, M.; Hamza, M.A. Anomalies Forecast in Radon Time Series for Earthquake Likelihood Using Machine Learning-Based Ensemble Model. *IEEE Access* **2022**, *10*, 37984–37999.
154. Firstov, P.; Makarov, E. Reaction in the field of subsoil gases to the preparation of the earthquake on March 16, 2021 with MW = 6.6 (Kamchatka, Russia). *J. Phys.: Conf. Ser.* **2021**, *2094*. Article 052026, doi:10.1088/1742-6596/2094/5/052026.
155. Tiwari, R.C.; Jaishi, H.P.; Singh, S.; Tiwari, R.P. A study of soil radon and seismicity along active fault region in northeastern India. *Arabian Journal of Geosciences* **2023**, *16*, 253.
156. D'Incecco, S.; Di Carlo, P.; Aruffo, E.; Chatzisavvas, N.; Petraki, E.; Priniotakis, G.; Voyiatzis, I.; Yannakopoulos, P.H.; Nikolopoulos, D. Fractal dimension analysis applied to soil CO₂ fluxes in Campotosto's Seismic Area, Central Italy. *Geosciences* **2020**, *10*, 233.
157. D'Incecco, S.; Petraki, E.; Priniotakis, G.; Papoutsidakis, M.; Yannakopoulos, P.; Nikolopoulos, D. and Radon Emissions as Precursors of Seismic Activity. *Earth Systems and Environment* **2021**, *5*, 655–666.
158. Orihara, Y.; Kamogawa, M.; Nagao, T. Preseismic Changes of the Level and Temperature of Confined Groundwater related to the 2011 Tohoku Earthquake. *Sci. Rep.* **2014**, *4*, 6907. doi:10.1038/srep06907.
159. Hosono, T.; Yamada, C.; Shibata, T.; Tawara, Y.; Wang, C.Y.; Manga, M.; Rahman, A.T.M.S.; Shimada, J. Coseismic Groundwater Drawdown Along Crustal Ruptures During the 2016 Mw 7.0 Kumamoto Earthquake. *Water Resources Research* **2019**, *55*, 5891–5903. doi:https://doi.org/10.1029/2019WR024871.
160. Omori, Y.; Nagahama, H.; Yasuoka, Y.; M., J. Radon degassing triggered by tidal loading before an earthquake. *Sci. Rep.* **2021**, *11*, 4092. doi:10.1038/s41598-021-83499-0.
161. Huang, P.; Lv, W.; Huang, R.; Luo, Q.; Yang, Y. Earthquake precursors: A review of key factors influencing radon concentration. *J. Environ. Radioactiv* **2024**, *271*, 107310.
162. Petraki, E.; Nikolopoulos, D.; Panagiotaras, D.; Cantzos, D.; Yannakopoulos, P.; others. Radon-222: A Potential Short-Term Earthquake Precursor. *J. Earth Sci. Clim. Change* **2015**, *6*, 1–11. doi:10.4172/2157-7617.1000282.
163. Kuo, T.; Chen, W.; Lewis, C.; Ho, C.; Kuochen, H. Precursory Behavior of Groundwater Radon in Southeastern Taiwan: Effect of Tectonic Setting in the Subduction Zone. *Pure Appl. Geophys.* **2020**, *177*, 2877–2887.

164. Torkar, D.; Zmazek, B.; Vaupotić, J.; Koba, I. Application of artificial neural networks in simulating radon levels in soil gas. *Chem. Geol.* **2010**, *270*, 1–8.
165. Chetia, T.; Baruah, S.; Dey, C.; Baruah, S.; Sharma, S. Seismic induced soil gas radon anomalies observed at multiparametric geophysical observatory, Tezpur (Eastern Himalaya), India: an appraisal of probable model for earthquake forecasting based on peak of radon anomalies. *Nat.Hazards* **2022**, *111*, 3071–3098. doi:10.1007/s11069-021-05168-9.
166. Jaishi, H.P.; Singh, S.; Tiwari, R.P.; Tiwari, R.C. Analysis of Subsurface Soil Radon with the Environmental Parameters and Its Relation with Seismic Events. *Journal of the Geological Society of India* **2023**, *99*, 847–858.
167. Iwata, D.; Nagahama, H.; Muto, J.; Yasuoka, Y. Non-parametric detection of atmospheric radon concentration anomalies related to earthquakes. *Sci. Rep.* **2018**, *8*, 13028. doi:10.1038/s41598-018-31341-5.
168. Kawabata, K.; Sato, T.; Takahashi, H.A.; Tsunomori, F.; Hosono, T.; Takahashi, M.; Kitamura, Y. Changes in groundwater radon concentrations caused by the 2016 Kumamoto earthquake. *J. Hydrol.* **2020**, *584*, 124712. doi:https://doi.org/10.1016/j.jhydrol.2020.124712.
169. Romano, D.; Sabatino, G.; Magazù, S.; others. Distribution of soil gas radon concentration in north-eastern Sicily (Italy): hazard evaluation and tectonic implications. *Environ. Earth Sci.* **2023**, *82*, 273. doi:10.1007/s12665-023-10956-6.
170. Chowdhury, S.; Deb, A.; Barman, C.; Nurujjaman, M.; Bora, D.K. Simultaneous monitoring of soil ²²²Rn in the Eastern Himalayas and the geothermal region of eastern India: an earthquake precursor. *Nat. Hazards* **2022**, *112*, 1477–1502.
171. Walia, V.; Kumar, A.; Chowdhury, S.; Lin, S.J.; Lee, H.F.; Fu, C.C. Earthquake precursory study using decomposition technique: time series soil radon monitoring data from the San-Jie Station in Northern Taiwan. *J. Radioanal. Nucl. Chem.* **2023**, pp. 1–8.
172. Karastathis, V.K.; Eleftheriou, G.; Kafatos, M.; Tsinganos, K.; Tselentis, G.A.; Mouzakiotis, E.; Ouzounov, D. Observations on the stress related variations of soil radon concentration in the Gulf of Corinth, Greece. *Sci. Rep.* **2022**, *12*, 5442.
173. Manisa, K.; Erdogan, M.; Zedef, V.; Bircan, H.; Biçer, A. Variations of ²²²Rn concentrations over active fault system in Simav, Kütahya, Western Turkey: Possible causes for soil-gas ²²²Rn anomalies. *Appl. Radiat. Isot.* **2022**, *190*, 110484.
174. Galiana-Merino, J.J.; Molina, S.; Kharazian, A.; Toader, V.E.; Moldovan, I.A.; Gómez, I. Analysis of radon measurements in relation to daily seismic activity rates in the vrancea region, romania. *Sensors* **2022**, *22*, 4160.
175. Chowdhury, S.; Guha Bose, A.; Das, A.; Deb, A. A study of some research work on soil radon concentration and ionospheric total electron content as earthquake precursors. *J. Radioanal. Nucl. Chem.* **2024**, pp. 1–27.
176. Eftaxias, K. Footprints of non-extensive Tsallis statistics, self-affinity and universality in the preparation of the L'Aquila earthquake hidden in a pre-seismic EM emission. *Physica A* **2010**, *389*, 133–140.
177. Planinić, J.; Radolić, V.; Lazanin, Z. Temporal variations of radon in soil related to earthquakes. *Appl. Radiat. Isot.* **2001**, *55*, 267–272.
178. Radolić, V.; Vuković, B.; Stanić, D.; Planinić, J. Radon chaotic regime in the atmosphere and soil. *Fizika A* **2005**, *2*, 195–206.
179. Alam, A.; Wang, N.; Zhao, G.; Mehmood, T.; Nikolopoulos, D. Long-lasting patterns of radon in groundwater at Panzhihua, China: Results from DFA, fractal dimensions and residual radon concentration. *Geochem. J.* **2019**, *53*, 341–358.
180. Alam, A.; Wang, N.; Petraki, E.; Barkat, A.; Huang, F.; Shah, M.A.; Cantzos, D.; Priniotakis, G.; Yannakopoulos, P.H.; Papoutsidakis, M.; Nikolopoulos, D. Fluctuation Dynamics of Radon in Groundwater Prior to the Gansu Earthquake, China (22 July 2013: M_s = 6.6): Investigation with DFA and MF DFA Methods. *Pure and Applied Geophysics* **2021**, *178*, 3375–3395.
181. Stoulos, S.; Ioannidou, A. Time-series analysis of radon monitoring in soil gas in association with earthquakes in Stivos faulting, at Lagadas basin, North Greece. *J. Radioanal. Nucl. Chem.* **2023**, *332*, 4581–4590.
182. Zhou, H.; Wan, Y.; Su, H.; Li, C. Spatial-temporal evolution of soil gas Rn before two M_s ≥ 5.0 earthquakes in the mid-eastern of the Qilian fault zone (QLF). *Sci. Rep.* **2023**, *13*, 21491.
183. M.H.Al-Tamimi.; Abumura, K. Radon anomalies along faults in North of Jordan. *Radiat. Meas.* **2001**, *34*, 397–400.

184. Mogro-Campero, A.; Fleischer, R. *Search for long-distance migration of subsurface radon*; US Department of Energy: Washington DC, 1979.
185. Sadovsky, M.A.; Nersesov, I.L.; Nigmatullaev, S.K.; others. (1972) The Processes Preceding Strong Earthquakes in Some Regions of Middle Asia. *Tectonophysics* **1972**, *14*, 295–307.
186. King, C.Y. Gas geochemistry applied to earthquake prediction: An overview. *Geophys. Res. Solid Earth* **1986**, *91*, 12269–12281. doi:https://doi.org/10.1029/JB091iB12p12269.
187. Wakita, H.; Nakamura, Y.; Notsu, K.; Noguchi, M.; Asada, T. Radon anomaly: a possible precursor of the 1978 Izu-Oshima-kinkai earthquake. *Science; (United States)* **1980**, *207*. doi:10.1126/science.207.4433.882.
188. Shapiro, M.H.; Melvin, J.D.; Tombrello, T.A.; Whitcomb, J.H. Automated radon monitoring at a hard-rock site in the southern California transverse ranges. *Geophys. Res. Solid Earth* **1980**, *85*, 3058–3064. doi:https://doi.org/10.1029/JB085iB06p03058.
189. Hauksson, E. Radon content of groundwater as an earthquake precursor: Evaluation of worldwide data and physical basis. *Geophys. Res. Solid Earth* **1981**, *86*, 9397–9410. doi:https://doi.org/10.1029/JB086iB10p09397.
190. Igarashi, G.; Saeki, S.; Takahata, N. Ground-water radon anomaly before the Kobe earthquake in Japan. *Science* **1995**, *269*, 60–61.
191. Ohno, M.; Wakita, H. Coseismic radon changes of the 1995 Hyogo-ken Nanbu earthquake. *J. Phys. Earth* **1996**, *44*, 391–395.
192. Virk, H.S.; Walia, V.; Kumar, N. Helium/radon pre-cursory anomalies of Chamoli earthquake, Garhwal Himalaya. *India. J. Geodyn.* **2001**, *31*, 201–210.
193. Baykara, O.; Dogru, M. Measurements of radon and uranium concentration in water and soil samples from East Anatolian Active Fault Systems (Turkey). *Radiat. Meas.* **2006**, *41*, 362–367.
194. Kuo, T.; Fan, K.; Kuochen, H.; Han, Y.; Chu, H.; Lee, Y. Anomalous decrease in groundwater radon before the Taiwan M6.8 Chengkung earthquake. *J. Environ. Radioactiv.* **2006**, *88*, 101–106. doi:https://doi.org/10.1016/j.jenvrad.2006.07.005.
195. Zmazek, B.; Todorovski, L.; Zivcic, M.; Dzeroski, S.; Vaupotic, J.; Kobal, I. Radon in a thermal spring: Identification of anomalies related to seismic activity. *Appl. Radiat. Isot.* **2006**, *64*, 725–734.
196. Kumar, A.; Singh, S.; Mahajan, S.; Bajwa, B.S.; Kalia, R.; Dhar, S. Earthquake precursory studies in Kangra Valley of North West Himalayas, India with special emphasis on radon emission. *Appl. Radiat. Isot* **2009**, *67*.
197. Kuo, T. Correlating Precursory Declines in Groundwater Radon with Earthquake Magnitude. *Groundwater* **2014**, *52*, 217–224. doi:https://doi.org/10.1111/gwat.12049.
198. Skelton, A.; Andrén, M.; Kristmannsdóttir, H.; Stockmann, G.; Mörrth, C.M.; Sveinbjörnsdóttir, Á.; Jónsson, S.; Sturkell, E.; Guðrúnardóttir, H.R.; Hjartarson, H.; Siegmund, H.; Kockum, I. Changes in groundwater chemistry before two consecutive earthquakes in Iceland. *Nature Geoscience* **2014**, *7*, 752–756.
199. Nevinsky, I.; Tsvetkova, T.; Nevinskaya, E. Measurement of radon in ground waters of the Western Caucasus for seismological application. *J. Environ. Radioactiv* **2015**, *149*, 19–35. doi:https://doi.org/10.1016/j.jenvrad.2015.07.005.
200. Zhang, S.; Shi, Z.; Wang, G.; Yan, R.; Zhang, Z. Groundwater radon precursor anomalies identification by decision tree method. *Appl. Geochem.* **2020**, *121*, 104696.
201. Qiao, Z.; Wang, G.; Fu, H.; Hu, X. Identification of Groundwater Radon Precursory Anomalies by Critical Slowing down Theory: A Case Study in Yunnan Region, Southwest China. *Water* **2022**, *14*. doi:10.3390/w14040541.
202. Alam, A.; Wang, N.; Zhao, G.; Barkat, A. Implication of radon monitoring for earthquake surveillance using statistical techniques: a case study of Wenchuan earthquake. *Geofluids* **2020**, *2020*, 1–14.
203. Tarakçı, M.; Harmanşah, C.; Saç, M.M.; İçhedef, M. Investigation of the relationships between seismic activities and radon level in western Turkey. *Appl. Radiat. Isot.* **2014**, *83 Pt A*, 12–17.
204. Sandıkcioglu Gümüş, A. Investigation of the relationship between the decline in well waters radon anomalies and the earthquake magnitude (Mw). *J. Radioanal. Nucl. Chem.* **2024**, pp. 1–14.
205. Jin, X.; Bu, J.; Qiu, G.; Ma, L.; Chen, Z.; Chen, T.; Wu, J.; Pan, B.; Ji, H.; Tian, J.; Wu, X.; Li, Z.; Zhang, L.; Liu, C.; Zhao, X.; Cheng, X. Non-normal distribution of radon and residual radon and short-term abnormal precursors of residual radon before major earthquakes. *Earth Science Informatics* **2022**, *15*, 2495–2511.
206. Kandari, T.; Aswal, S.; Prasad, M.; Bourai, A.; Ramola, R. Estimation of annual effective dose from radon concentration along Main Boundary Thrust (MBT) in Garhwal Himalaya. *JRRAS* **2016**, *9*, 228–233.
207. Fonollosa, E.; Peñalver, A.; Borrull, F.; Aguilar, C. Radon in spring waters in the south of Catalonia. *J. Environ. Radioactiv* **2016**, *151*, 275–281.

208. Alonso, H.; Cruz-Fuentes, T.; Rubiano, J.G.; González-Guerra, J.; Cabrera, M.d.C.; Arnedo, M.A.; Tejera, A.; Rodríguez-Gonzalez, A.; Pérez-Torrado, F.J.; Martel, P. Radon in groundwater of the northeastern Gran Canaria aquifer. *Water* **2015**, *7*, 2575–2590.
209. Rahimi, M.; Abadi, A.A.M.; Koopaei, L.J. Radon concentration in groundwater, its relation with geological structure and some physicochemical parameters of Zarand in Iran. *Appl. Radiat. Isot.* **2022**, *185*, 110223.
210. Abbas, S.Q.; Khan, J.; Riaz, M.T.; Rafique, M.; Zaman, A.; Khan, S. Radon concentration in spring water as an indicator of seismic activity: a case study of the Muzaffarabad Fault in Pakistan. *Environmental Monitoring and Assessment* **2024**, *196*, 41.
211. Nikolopoulos, D.; Vogianis, E. Modelling of radon concentration peaks in thermal spas: Application to Polichnitos and Eftalou spas (Lesvos Island-Greece). *Sci. Total Environ.* **2008**, *405*, 36–44.
212. Vogianis, E.; Nikolopoulos, D. Modelling of radon concentration peaks in thermal spas: Application to Polichnitos and Eftalou spas (Lesvos Island—Greece). *Science of The Total Environment* **2008**, *405*, 36–44. doi:https://doi.org/10.1016/j.scitotenv.2008.06.029.
213. Yan, X.; Shi, Z.; Wang, G.; Zhang, H.; Bi, E. Detection of possible hydrological precursor anomalies using long short-term memory: A case study of the 1996 Lijiang earthquake. *J. Hydrol.* **2021**, *599*, 126369.
214. Hayashi, K.; Yasuoka, Y.; Nagahama, H.; Muto, J.; Ishikawa, T.; Omori, Y.; Suzuki, T.; Homma, Y.; Mukai, T. Normal seasonal variations for atmospheric radon concentration: a sinusoidal model. *J. Environ. Radioactiv* **2015**, *139*, 149–153.
215. Omori, Y.; Tohbo, I.; Nagahama, H.; Ishikawa, Y.; Takahashi, M.; Sato, H.; Sekine, T. Variation of atmospheric radon concentration with bimodal seasonality. *Radiat. Meas.* **2009**, *44*, 1045–1050.
216. Yasuoka, Y.; Shinogi, M. Anomaly in atmospheric radon concentration: a possible precursor of the 1995 Kobe, Japan, earthquake. *Health Phys.* **1997**, *72*, 759–761.
217. Goto, M.; Yasuoka, Y.; Nagahama, H.; Muto, J.; Omori, Y.; Ihara, H.; Mukai, T. Anomalous changes in atmospheric radon concentration before and after the 2011 northern Wakayama Earthquake (Mj 5.5). *Rad. Prot. Dos.* **2016**, *174*, 412–418. doi:10.1093/rpd/ncw142.
218. Kawada, Y.; Nagahama, H.; Omori, Y.; Yasuoka, Y.; Ishikawa, T.; Tokonami, S.; Shinogi, M. Time-scale invariant changes in atmospheric radon concentration and crustal strain prior to a large earthquake. *Nonlinear Processes in Geophysics* **2007**, *14*, 123–130.
219. Yasuoka, Y.; Kawada, Y.; Nagahama, H.; Omori, Y.; Ishikawa, T.; Tokonami, S.; Shinogi, M. Preseismic changes in atmospheric radon concentration and crustal strain. *Phys. Chem. Earth* **2009**, *34*, 431–434. doi:https://doi.org/10.1016/j.pce.2008.06.005.
220. Tsunogai, U.; Wakita, H. Precursory chemical changes in ground water: Kobe earthquake, Japan. *Science* **1995**, *269*, 61–63.
221. Yasuoka, Y.; Nagahama, H.; Muto, J.; Mukai, T. The anomaly in atmospheric radon concentrations prior to the 2011 Tohoku-Oki earthquake in Japan. *REM* **2018**, *7*, 86–94.
222. Draganov, A.B.; Inan, U.S.; Taranenko, Y.N. ULF magnetic signatures at the Earth surface due to ground water flow: A possible precursor to earthquakes. *Geophys. Res. Lett.* **1991**, *18*, 1127–1130. doi:https://doi.org/10.1029/91GL01000.
223. Y, S. Tectonomagnetic modeling on the basis of the linear piezomagnetic effect. *Bulletin of the Earthquake Research Institute University of Tokyo* **1991**, *66*, 585–722.
224. Fitterman, D.V. Electrokinetic and magnetic anomalies associated with dilatant regions in a layered Earth. *Geophys. Res. Solid Earth* **1978**, *83*, 5923–5928. doi:https://doi.org/10.1029/JB083iB12p05923.
225. Varotsos, P.; Alexopoulos, K.; Nomicos, K.; Lazaridou, M. Earthquake prediction and electric signals. *Nature* **1986**, *322*, 120–120.
226. MIZUTANI, H.; ISHIDO, T. A New Interpretation of Magnetic Field Variation Associated with the Matsushiro Earthquakes. *Journal of geomagnetism and geoelectricity* **1976**, *28*, 179–188. doi:10.5636/jgg.28.179.
227. Jouniaux, L.; Pozzi, J.P. Streaming potential and permeability of saturated sandstones under triaxial stress: Consequences for electrotelluric anomalies prior to earthquakes. *Geophys. Res. Solid Earth* **1995**, *100*, 10197–10209. doi:https://doi.org/10.1029/95JB00069.
228. Surkov, V.; Uyeda, S.; Tanaka, H.; Hayakawa, M. Fractal properties of medium and seismoelectric phenomena. *Journal of Geodynamics* **2002**, *33*, 477–487. doi:https://doi.org/10.1016/S0264-3707(02)00009-1.
229. Feder, J. *Fractals*; Springer Science, 1988. doi:1007/978-1-4899-2124-6.

230. Yasuoka, Y.; Kawada, Y.; Omori, Y.; Nagahama, H.; Ishikawa, T.; Tokonami, S.; Hosoda, M.; Hashimoto, T.; Shinogi, M. Anomalous change in atmospheric radon concentration sourced from broad crustal deformation: A case study of the 1995 Kobe earthquake. *Appl. Geochem.* **2012**, *27*, 825–830.
231. Nikolopoulos, D.; Yannakopoulos, P.H.; Petraki, E.; Cantzos, D.; Nomicos, C. Long-Memory and Fractal Traces in kHz-MHz Electromagnetic Time Series Prior to the ML=6.1, 12/6/2007 Lesvos, Greece Earthquake: Investigation through DFA and Time-Evolving Spectral Fractals. *J. Earth Sci. Clim. Change* **2018**, *9*, 1–15.
232. Scholz, C.; Sykes, L.; Agarwal, Y. Earthquake prediction: a physical basis. *Science* **1973**, *181*, 803–810.
233. Lay, T.; Williams, Q.; Garnero, E. The core-mantle boundary layer and deep Earth dynamic. *Nature* **1998**, *392*, 461–468.
234. Anderson, O.; Grew, P. Stress corrosion theory of crack propagation with applications to geophysics. *Rev. Geophys. Space Phys.* **1997**, *15*, 77–84.
235. Gregorić, A.; Zmazek, B.; Džeroski, S.; Torkar, D.; Vaupotić, J. Radon as an Earthquake Precursor-Methods for Detecting Anomalies. In *Earthquake Research and Analysis-Statistical Studies, Observation and Planning*; D'Amico, S., Ed.; IntechOpen: Rijeka, 2012; chapter 9. doi:10.5772/29108.
236. Nikolopoulos, D.; Matsoukas, C.; Yannakopoulos, P.H.; Petraki, E.; Cantzos, D.; Nomicos, C. Long-Memory and Fractal Trends in Variations of Environmental Radon in Soil: Results from Measurements in Lesvos Island in Greece, J Earth Sci. *J. Earth Sci. Clim. Change* **2018**, *9*, 1–11. doi:https://doi.org/10.4172/2157-7617.1000460.
237. Talwani, P.; Chen, L.; Gahalaut, K. Seismogenic permeability , ks. *J. Geoph. Res.* **2007**, *112*. doi:10.1029/2006JB004665.
238. Awais, M.; Barkat, A.; Ali, A.; Rehman, K.; Ali Zafar, W.; Iqbal, T. Satellite thermal IR and atmospheric radon anomalies associated with the Haripur earthquake (Oct 2010; M_w 5.2), Pakistan. *ASR* **2017**, *60*, 2333–2344. doi:10.1016/j.asr.2017.08.034.
239. Barkat, A.; Ali, A.; Hayat, U.; Crowley, Q.G.; Rehman, K.; Siddique, N.; Haidar, T.; Iqbal, T. Time series analysis of soil radon in Northern Pakistan: Implications for earthquake forecasting. *Appl. Geochem.* **2018**, *97*, 197–208.
240. Jilani, Z.; Mehmood, T.; Alam, A.; Awais, M.; Iqbal, T. Monitoring and descriptive analysis of radon in relation to seismic activity of Northern Pakistan. *J. Environ. Radioactiv* **2017**, *172*, 43–51. doi:https://doi.org/10.1016/j.jenvrad.2017.
241. Yonaiguchi, N.; Ida, Y.; Hayakawa, M.; Masuda, S. Fractal analysis for VHF electromagnetic noises and the identification of preseismic signature of an earthquake. *J. Atmos. Sol. Ter. Phy.* **2007**, *69*, 1825–1832.
242. Hayakawa, M.; Ida, Y.; Gotoh, K. Multifractal analysis for the ULF geomagnetic data during the Guam earthquake. Electromagnetic Compatibility and Electromagnetic Ecology. IEEE 6th International Symposium on June 2005. 239-243, 2005, pp. 21–24.
243. Balasis, G.; Daglis, I.A.; Kapisir, P.; Manda, M.; Vassiliadis, D.; Eftaxias, K. From pre-storm activity to magnetic storms: a transition described in terms of fractal dynamics,. *Ann. Geophys.* **2006**, *24*, 3557–3567.
244. Balasis, G.; Potirakis, S.; Manda, M. Investigating Dynamical Complexity of Geomagnetic Jerks Using Various Entropy Measures. *Front. Earth. Sci* **2016**, *4*, 1–10.
245. Cantzos, D.; Nikolopoulos, D.; Petraki, E.; Yannakopoulos, P.H.; Nomicos, C. Fractal Analysis, Information-Theoretic Similarities and SVM Classification for Multichannel, Multi-Frequency Pre-Seismic Electromagnetic Measurements. *J. Earth. Sci. Clim. Change* **2016**, *7*, 1–10.
246. Cantzos, D.; Nikolopoulos, D.; Petraki, E.; Yannakopoulos, P.H.; Nomicos, C. Earthquake precursory signatures in electromagnetic radiation measurements in terms of day-to-day fractal spectral exponent variation: analysis of the eastern Aegean 13/04/2017–20/07/2017 seismic activity. *J. Seismol.* **2018**, *22*, 1499–1513.
247. de la Torre, F.C.; Ramirez-Rojas, A.; Pavia-Miller, C.; Angulo-Brown, F.; E, E.Y.; Peralta, J. A comparison between spectral and fractal methods in electrotelluric time series. *Revista Mexicana de Fisica* **1999**, *45*, 298–302.
248. de la Torre, F.C.; Gonzaalez-Trejo, J.; Real-Ramírez, C.; Hoyos-Reyes, L. Fractal dimension algorithms and their application to time series associated with natural phenomena. *J. Phys. Conf. Ser.* **2013**, *475*, 1–10.
249. Gotoh, K.; Hayakawa, M.; Smirnova, N. Fractal analysis of the ULF geomagnetic data obtained at Izu Peninsula, Japan in relation to the nearby earthquake swarm of June-August 2000. *Nat. Haz. Earth Sys.* **2003**, *3*, 229–234.
250. Gotoh, K.; Hayakawa, M.; Smirnova, N.; Hattori, K. Fractal analysis of seismogenic ULF emissions. *Phys. Chem. Earth* **2004**, *29*, 419–424.

251. Hayakawa, M.; Ida, Y.; Gotoh, K. Fractal (mono- and multi-) analysis for the ULF data during the 1993 Guam earthquake for the study of prefraction criticality. *Current Development in Theory and Applications of Wavelets* **2008**, *2*, 159–174.
252. Ida, Y.; Hayakawa, M. Fractal analysis for the ULF data during the 1993 Guam earthquake to study prefraction criticality. *Nonlinear Processes in Geophysics* **2006**, *13*, 409–412.
253. Ida, Y.; Hayakawa, M. Fractal analysis for the ULF data during the 1993 Guam earthquake to study prefraction criticality. *Nonlin. Processes Geophys.* **2012**, *13*, 409–412.
254. Ida, Y., Y.; Li, D.; Q., S.; H., H.; M.. Fractal analysis of ULF electromagnetic emissions in possible association with earthquakes in China. *Nonlin. Processes Geophys.* **2012**, *19*, 577–583.
255. Nikolopoulos, D.; Petraki, E.; Cantzos, D.; Yannakopoulos, P.H.; Panagiotaras, D.; Nomicos, C. Fractal Analysis of Pre-Seismic Electromagnetic and Radon Precursors: A Systematic Approach. *J. Earth Sci. Clim. Change* **2016**, *7*, 1–11.
256. Smirnova, N.; Hayakawa, M.; Gotoh, K. Precursory behavior of fractal characteristics of the ULF electromagnetic fields in seismic active zones before strong earthquakes. *Phys. Chem. Earth* **2004**, *29*, 445–451.
257. Smirnova, N.A.; Kiyashchenko, D.A.; Troyan.; N., V.; Hayakawa, M. Multifractal Approach to Study the Earthquake Precursory Signatures Using the Ground-Based Observations. *Review of Applied Physics* **2013**, *2*, 3.
258. Karamanos, K. From symbolic dynamics to a digital approach: Chaos and Transcendence. *Lect. Notes Phys.* **2000**, *550*, 357–371.
259. Karamanos, K. Entropy analysis of substitutive sequences revisited. *J Phys. A Math. Gen.* **2001**, *34*, 9231–9241.
260. Karamanos, K.; Nicolis, G. Symbolic Dynamics and Entropy Analysis of Feigenbaum Limit Sets. *Chaos Soliton. Frac.* **1999**, *10*, 1135–1150.
261. Karamanos, K.; Dakopoulos, D.; Aloupis, K.; Peratzakis, A.; Athanasopoulou, L.; Nikolopoulos, S.; P, P.K.; Eftaxias, K. Study of pre-seismic electromagnetic signals in terms of complexity. *Phys. Rev. E.* **2006**, *74*, 21–36.
262. Karamanos, K.; Dakopoulos, D.; Aloupis, K.; Peratzakis, A.; Athanasopoulou, L.; Nikolopoulos, S.; P, P.K.; Eftaxias, K. Study of pre-seismic electromagnetic signals in terms of complexity. *Phys. Rev. E.* **2006**, *74*, 21–36.
263. Varotsos, P.; Sarlis, N.; Skordas, E. Natural time analysis of critical phenomena. *Chaos* **2009**, *19*.
264. Varotsos, P.; Sarlis, N.; Skordas, E. Scale-specific order parameter fluctuations of seismicity in natural time before mainshocks. *EPL* **2011**, *96*.
265. Varotsos, P.; Sarlis, N.; Skordas, E. *Natural Time Analysis: The new view of time. Precursory Seismic Electric Signals, Earthquakes and other Complex Time- Series*; Springer-Verlag: Berlin Heidelberg, 2011.
266. Varotsos, P.A.; Sarlis, N.V.; Skordas, E.S. Self-organized criticality and earthquake predictability: A long-standing question in the light of natural time analysis. *Europhysics Letters* **2020**, *132*, 29001. doi:10.1209/0295-5075/132/29001.
267. Varotsos, P.A.; Sarlis, N.V.; Skordas, E.S. Order Parameter and Entropy of Seismicity in Natural Time before Major Earthquakes: Recent Results. *Geosciences* **2022**, *12*. doi:10.3390/geosciences12060225.
268. Nikolopoulos, D.; Cantzos, D.; Petraki, E.; Yannakopoulos, P.H.; Nomicos, C. Traces of long-memory in pre-seismic MHz electromagnetic time series-Part1: Investigation through the R/S analysis and time-evolving spectral fractals. *J. Earth Sci. Clim. Change* **2016**, *7*.
269. Pastén, D.; Pavez-Orrego, C. Multifractal time evolution for intraplate earthquakes recorded in southern Norway during 1980–2021. *Chaos, Solitons & Fractals* **2023**, *167*, 113000. doi:https://doi.org/10.1016/j.chaos.2022.113000.
270. Telesca, L.; Lapenna, V.; Vallianatos, F. Monofractal and multifractal approaches in investigating scaling properties in temporal patterns of the 1983–2000 seismicity in the Western Corinth Graben, Greece. *Phys. Earth Planet. Int* **2002**, *131*, 63–79.
271. Telesca, L.; Lapenna, V.; Macchiato, M. Mono- and multi-fractal investigation of scaling properties in temporal patterns of seismic sequences. *Chaos Solit. Fractals* **2004**, *19*, 1–15.
272. Nikolopoulos, D.; Alam, A.; Petraki, E.; Papoutsidakis, M.; Yannakopoulos, P.; Moustris, K.P. Stochastic and self-organisation patterns in a 17-year PM10 time series in Athens, Greece. *Entropy* **2021**, *23*, 307.
273. Morales, I.O.; Landa, O.; Fossion, R.; Frank, A. Scale invariance, self-similarity and critical behaviour in classical and quantum system. *J. Phys. Conf. Ser.* **2012**, *380*.

274. May, R.M. Simple mathematical models with very complicated dynamics. *Nature* **1976**, *261*, 459–467.
275. Sugihara, G.; May, R. Nonlinear forecasting as a way of distinguishing chaos from measurement error in time series. *Nature* **1990**, *344*, 734–741.
276. Mandelbrot, B.B.; Ness, J.W.V. Fractional Brownian motions, fractional noises and applications. *J. Soc. Ind. Appl. Math* **1968**, *10*, 422–437.
277. Musa, M.; Ibrahim, K. Existence of long memory in ozone time series. *Sains Malaysiana* **2012**, *41*, 1367–1376.
278. Hurst, H. Long term storage capacity of reservoirs. *Trans. Am. Soc. Civ. Eng.* **1951**, *116*, 770–808.
279. Hurst, H.; Black, R.; Simaiki, Y. *Long-term Storage: An Experimental Study*; Constable: London, 1965. Hurst H, Black R, Simaiki Y (1965) Long-term Storage: An Experimental Study. Constable, London.
280. Lopez, T.; Martinez-Gonzalez, C.; Manjarrez, J.; Plascencia, N.; Balankin, A. Fractal Analysis of EEG Signals in the Brain of Epileptic Rats, with and without Biocompatible Implanted Neuroreservoirs. *AMM* **2009**, *15*, 127–136. doi:http://dx.doi.org/10.4028/www.scientific.net/AMM.15.127.
281. Fujinawa, Y.; Takahashi, K. Electromagnetic radiations associated with major earthquakes. *Phys. Earth Planet Inter.* **1998**, *105*, 249–259. doi:https://doi.org/10.1016/S0031-9201(97)00117-9.
282. Hayakawa, M. VLF/LF radio sounding of ionospheric perturbations associated with earthquakes. *Sensors* **2007**, *7*, 1141–1158.
283. Nikolopoulos, D.; Moustiris, K.; Petraki, E.; D., K.; Cantzos, D. Fractal and long-memory traces in PM₁₀ time series in Athens, Greece. *Environmetrics* **2019**, *6*, 1–19. doi:https://doi.org/10.3390/environments6030029.
284. Katz, M. Fractals and the analysis of waveforms. *Comput. Biol. Med.* **1988**, *18*, 145–156.
285. Raghavendra, B.; Dutt, D.N. Computing Fractal Dimension of Signals using Multiresolution Box-counting Method. *nter. J. Elec. Comp. Ener. Electronic Commun. Eng.* **2010**, *4*, 183–198.
286. Higuchi, T. Approach to an irregular time series on basis of the fractal theory. *Physica D* **1988**, *31*, 277–283.
287. Sevcik, C. On fractal dimension of waveforms. *Chaos Solit. Fract.* **2006**, *27*, 579–580.
288. Rikitake, T. *Earthquake Prediction*; Elsevier Sci. Publ. Co: Amsterdam, 1976.
289. Talwani, P. An empirical earthquake prediction model. *Phys. Earth Planet Inter.* **1979**, *18*, 288–302. doi:https://doi.org/10.1016/0031-9201(79)90065-7.
290. GUHA, S. Premonitory Crustal Deformations, Strains and Seismotectonic Features (B-VALUES) PRECEDING KOYNA EARTHQUAKES. In *Recent Crustal Movements*, 1977; WHITTEN, C.; GREEN, R.; MEADE, B., Eds.; Elsevier, 1979; Vol. 13, *Developments in Geotectonics*, pp. 549–559. doi:https://doi.org/10.1016/B978-0-444-41783-1.50082-9.
291. Dobrovolsky, I.; Zubkov, S.; Miachkin, V. Estimation of the size of earthquake preparation zones. *Pure Appl. Geophys.* **1979**, *117*, 1025–1044.
292. Fleischer, R.L. Dislocation model for radon response to distant earthquakes. *Geophys. Res. Lett.* **1981**, *8*, 477–480. doi:https://doi.org/10.1029/GL008i005p00477.
293. Fleischer, R.L.; Mogro-Campero, A. Association of subsurface radon changes in Alaska and the northeastern United States with earthquakes. *Geochimica et Cosmochimica Acta* **1985**, *49*, 1061–1071. doi:https://doi.org/10.1016/0016-7037(85)90319-9.
294. Virk, H.S. A critique of empirical scaling relationship between earthquake magnitude, epicentral distance and precursor time for interpretation of radon data. *Journal of Earthquake Prediction Research* **1996**, *5*, 574–583.
295. Warwick, J.W.; Stoker, C.; Meyer, T.R. Radio emission associated with rock fracture: Possible application to the Great Chilean Earthquake of May 22, 1960. *Geophys. Res. Solid Earth* **1982**, *87*, 2851–2859. doi:https://doi.org/10.1029/JB087iB04p02851.
296. Smith, B.E.; Johnston, M.J.S. A tectonomagnetic effect observed before a magnitude 5.2 earthquake near Hollister, California. *Journal of Geophysical Research (1896-1977)* **1976**, *81*, 3556–3560. doi:https://doi.org/10.1029/JB081i020p03556.
297. Yulin, Z.; Fuye, Q. Geoelectric precursors to strong earthquakes in China. *Tectonophysics* **1994**, *233*, 99–113. doi:https://doi.org/10.1016/0040-1951(94)90223-2.
298. Wallace, R.; Teng, T. Forecast of the Sungpan-Pingwu earthquakes, 1976. *Bulletin of the Seismological Society of America* **1980**, *70*, 1199–1223. doi:https://doi.org/10.1785/BSSA0700041199.
299. Gershenzon, N.; Gokhberg, M. On the origin of electrotelluric disturbances prior to an earthquake in Kalamata, Greece. *Tectonophysics* **1993**, *224*, 169–174. doi:https://doi.org/10.1016/0040-1951(93)90069-V.
300. Serebryakova, O.; Bilichenko, S.; Chmyrev, V.; Parrot, M.; Rauch, J.L.; Lefeuvre, F.; Pokhotelov, O.A. Electromagnetic ELF radiation from earthquake regions as observed by low-altitude satellites. *Geophys. Res. Lett.* **1992**, *19*, 91–94. doi:10.1029/91GL02775.

301. Dea, J.; Hansen, P.; Boerner, W. Long-term EMF background noise measurements, the existence of window regions and applications to earthquake precursor emission studies. *Phys. Earth Planet Inter.* **77**: 109-125 Wallace R, Teng T (1980) Forecast of the Sungpan-Pingwu earthquakes, 1976. *Bulletin of the Seismological Society of America* **1993**, *70*, 1199–1223.
302. Shalimov, S.; Gokhberg, M. Lithosphere–ionosphere coupling mechanism and its application to the earthquake in Iran on June 20, 1990. A review of ionospheric measurements and basic assumptions. *Phys. Earth Planet Inter.* **1998**, *105*, 211–218. doi:https://doi.org/10.1016/S0031-9201(97)00092-7.
303. Y, R.; C, N. Radio VHF precursors of earthquakes. *Nat. Hazards* **2005**, *40*, 573–583.
304. Smirnova, N.; Hayakawa, M. Fractal characteristics of the ground-observed ULF emissions in relation to geomagnetic and seismic activities. *J. Atmos. Sol. Ter. Phy.* **2007**, *69*, 1833–1841.
305. Sarlis, N.; Skordas, E.; Varotsos, P.; Nagao, T.; M. Kamogawa, M.; Tanaka, H.; Uyeda, S. Minimum of the order parameter fluctuations of seismicity before major earthquakes in Japan. *Proc. Natl. Acad. Sci. USA*, **2013**, Vol. *110*, *34*, pp. 13734–13738.
306. Maeda, K.; Tokimasa, N. Decametric radiation at the time of the Hyogo-ken Nanbu Earthquake near Kobe in 1995. *Geophys. Res. Lett.* **1996**, *23*, 2433–2436. doi:https://doi.org/10.1029/96GL02307.
307. Bernard, P.; Pinettes, P.; Hatzidimitriou, P.M.; Scordilis, E.M.; Veis, G.; Milas, P. From precursors to prediction: a few recent cases from Greece. *Geophysical Journal International* **1997**, *131*, 467–477. doi:https://doi.org/10.1111/j.1365-246X.1997.tb06590.x.
308. Eftaxias, K.; Kapisir, P.; Polygiannakis, J.; Bogris, N.; Kopanas, J.; Antonopoulos, G.; Peratzakis, A.; Hadjicontis, V. Signature of pending earthquake from electromagnetic anomalies. *Geophys. Res. Lett.* **2001**, *28*, 3321–3324. doi:https://doi.org/10.1029/2001GL013124.
309. Eftaxias, K.; Kapisir, P.; Dologlou, E.; Kopanas, J.; Bogris, N.; Antonopoulos, G.; Peratzakis, A.; Hadjicontis, V. EM Anomalies before the Kozani Earthquake: A Study of Their Behavior through Laboratory Experiments. *Geophys. Res. Lett.* **2002**, *29*, 69–4. doi:10.1029/2001gl013786.
310. Kapisir, P.G.; Eftaxias, K.A.; Chelidze, T.L. Electromagnetic Signature of Prefracture Criticality in Heterogeneous Media. *Phys. Rev. Lett.* **2004**, *92*, 065702. doi:10.1103/PhysRevLett.92.065702.
311. Contoyiannis, Y.F.; Diakonos, F.K.; Kapisir, P.G.; Peratzakis, A.S.; Eftaxias, K.A. Intermittent dynamics of critical pre-seismic electromagnetic fluctuations. *Phys. Chem. Earth* **2004**, *29*, 397–408.
312. Varotsos, P.; Sarlis, N.; Eftaxias, K.; Lazaridou, M.; Bogris, N.; Makris, J.; Abdulla, A.; Kapisir, P. Prediction of the 6.6 Grevena-Kozani earthquake of May 13, 1995. *Phys. Chem. Earth A* **1999**, *24*, 115–121.
313. Varotsos, P.A.; Sarlis, N.V.; Skordas, E.S. Electric Fields that “Arrive” before the Time Derivative of the Magnetic Field prior to Major Earthquakes. *Phys. Rev. Lett.* **2003**, *91*, 148501. doi:10.1103/PhysRevLett.91.148501.
314. Varotsos, P.; Sarlis, N.; Skordas, E.; Lazaridou, M. Electric pulses some minutes before earthquake occurrences. *Appl. Phys. Lett.* **2007**, *90*, 1–3.
315. Enomoto, Y.; Tsutsumi, A.; Yukio, F.; Kasahara, M.; Hashimoto, H. Candidate precursors: Pulse-like geoelectric signals possibly related to recent seismic activity in Japan. *Geophysical Journal International* **1997**, *131*, 485–494. doi:10.1111/j.1365-246X.1997.tb06592.x.
316. Biagi, P.; Ermini, A.; Kingsley, S. Disturbances in LF radio signals and the Umbria-Marche (Italy) seismic sequence in 1997–1998. *Phys. Chem. Earth C*. **2001**, *26*, 755–759. doi:https://doi.org/10.1016/S1464-1917(01)95021-4.
317. Karakelian, D.; Klemperer, S.; Fraser-Smith, A.; Thompson, G. Ultra-low frequency electromagnetic measurements associated with the 1998 Mw 5.1 San Juan Bautista, California earthquake and implications for mechanisms of electromagnetic earthquake precursors. *Tectonophysics* **2002**, *359*, 65–79.
318. Eftaxias, K.A.; Kapisir, P.G.; Balasis, G.T.; Peratzakis, A.; Karamanos, K.; Kopanas, J.; Antonopoulos, G.; Nomicos, K.D. Unified approach to catastrophic events: from the normal state to geological or biological shock in terms of spectral fractal and nonlinear analysis. *NHESS* **2006**, *6*, 205–228. doi:10.5194/nhess-6-205-2006.
319. Nikolopoulos, S.; Kapisir, P.; Karamanos, K.; Eftaxias, K. A unified approach of catastrophic events. *NHESS* **2004**, *4*, 615–631. doi:10.5194/nhess-4-615-2004.
320. Kapisir, P.; Nomicos, K.; Antonopoulos, G.; others. Distinguished seismological and electromagnetic features of the impending global failure: Did the 7/9/1999 M5.9 Athens earthquake come with a warning? *Earth Planet Sp* **2005**, *57*, 215–230. doi:10.1186/BF03351818.

321. Kalimeri, M.; Papadimitriou, C.; Balasis, G.; Eftaxias, K. Dynamical complexity detection in pre-seismic emissions using non-additive Tsallis entropy. *Physica A* **2008**, *387*, 1161–1172.
322. Chuo, Y.; Liu, J.; Pulinet, S.; Chen, Y. The ionospheric perturbations prior to the Chi-Chi and Chia-Yi earthquakes. *Journal of Geodynamics* **2002**, *33*, 573–583.
323. Saroso, S.; Hattori, K.; Ishikawa, H.; Ida, Y.; Shirogane, R.; Hayakawa, M.; Yumoto, K.; Shiokawa, K.; Nishihashi, M. ULF geomagnetic anomalous changes possibly associated with 2004–2005 Sumatra earthquakes. *Phys. Chem. Earth* **2009**, *34*, 343–349.
324. Balasis, G.; Manda, M. Can EM disturbances related to the recent great earthquakes be detected by satellite magnetometers? *Tectonophysics* **2007**, *431*, 173–195.
325. Hayakawa, M.; Ohta, K.; Maekawa, S.; Yamauchi, T.; Ida, Y.; Gotoh, T.; Yonaiguchi, N.; Sasaki, H.; Nakamura, T. Electromagnetic precursors to the 2004 Mid Niigata Prefecture earthquake. *Phys. Chem. Earth* **2006**, *31*, 356–364. doi:10.1016/j.pce.2006.02.023.
326. Varotsos, P.; Sarlis, N.; Skordas, E.; Lazaridou, M. Identifying sudden cardiac death risk and specifying its occurrence time by analyzing electrocardiograms in natural time. *Appl. Phys. Lett.* **2007**, *91*.
327. Akpan, A.E.; Ibang, J.I.; George, N.J.; Ekanem, A.M. Assessing seismo-ionospheric disturbances using Vanuatu and Honshu earthquakes of March 25, 2007, employing DEMETER and GPS data. *International Journal of Environmental Science and Technology* **2019**, *16*, 7187–7196. doi:https://doi.org/10.1016/j.asr.2020.03.007.
328. Li, M.; Lu, J.; Zhang, X.; Shen, X. Indications of Ground-based Electromagnetic Observations to A Possible Lithosphere–Atmosphere–Ionosphere Electromagnetic Coupling before the 12 May 2008 Wenchuan MS 8.0 Earthquake. *Atmosphere* **2019**, *10*. doi:10.3390/atmos10070355.
329. Tachema, A.; Nadji, A. Contribution of ionospheric TEC anomalies to detecting the seismic precursors related to the 2008 Oran-Algeria event. *ASR* **2020**, *65*, 2559–2572. doi:https://doi.org/10.1016/j.asr.2020.03.007.
330. Zhang, X.; Liu, J.; De Santis, A.; Perrone, L.; Xiong, P.; Zhang, X.; Du, X. Lithosphere-atmosphere-ionosphere coupling associated with four Yutian earthquakes in China from GPS TEC and electromagnetic observations onboard satellites. *Journal of Geodynamics* **2023**, *155*, 101943. doi:https://doi.org/10.1016/j.jog.2022.101943.
331. Argunov, V.V.; Gotovcev, M.R. Study of Ionospheric Effects and Earthquake Precursors Using Radio Engineering Methods. *IOP Conference Series: Earth and Environmental Science* **2021**, *720*, 012087. doi:10.1088/1755-1315/720/1/012087.
332. Shi, K.; Guo, J.; Zhang, Y.; Li, W.; Kong, Q.; Yu, T. Multi-Dimension and Multi-Channel Seismic-Ionospheric Coupling: Case Study of Mw 8.8 Concepcion Quake on 27 February 2010. *Remote Sensing* **2021**, *13*. doi:10.3390/rs13142724.
333. Choi, B.K.; Lee, S.J. Anomalous ionospheric disturbances over South Korea prior to the 2011 Tohoku earthquake. *ASR* **2016**, *57*, 302–308. doi:https://doi.org/10.1016/j.asr.2015.10.025.
334. He, Y.; Zhao, X.; Yang, D.; Wu, Y.; Li, Q. A study to investigate the relationship between ionospheric disturbance and seismic activity based on Swarm satellite data. *Phys. Earth Planet Inter.* **2022**, *323*, 106826. doi:https://doi.org/10.1016/j.pepi.2021.106826.
335. Wang, J.; Chen, G.; Yu, T.; Deng, Z.; Yan, X.; Yang, N. Middle-Scale Ionospheric Disturbances Observed by the Oblique-Incidence Ionosonde Detection Network in North China after the 2011 Tohoku Tsunamiogenic Earthquake. *Sensors* **2021**, *21*. doi:10.3390/s21031000.
336. Yadav, A.; Singh, R.P. Effect of VLF electric field changes associated with major shallow earthquakes ($M = 5.6$ – 5.9) occurred in Indian subcontinent, on the atmosphere. *Indian Journal of Physics* **2023**, *97*, 3367–3378.
337. Joshi, S.; Madhusudhanarao, K. Ultra-Low Frequency Geomagnetic Variations before Dholavira Earthquake $M = 5.1$ on the 20th of June 2012 in Kachchh Region, Gujarat, India. *Geotectonics* **2021**, *55*, 633–645.
338. Gavrilov, B.G.; Poklad, Y.V.; Rybnov, Y.S.; Ryakhovsky, I.A.; Sanina, I.A. Geomagnetic Effects of Remote Earthquakes. *Geomagnetism and Aeronomy* **2021**, *61*, 108–116.
339. Meng, X.; Ravanelli, M.; Komjathy, A.; Verkhoglyadova, O.P. On the North-South Asymmetry of Co-Seismic Ionospheric Disturbances During the 16 September 2015 Illapel M8.3 Earthquake. *Geophys. Res. Lett.* **2022**, *49*, e2022GL098090. doi:https://doi.org/10.1029/2022GL098090.
340. Cahyadi, M.N.; Arisa, D.; Muafiry, I.N.; Muslim, B.; Rahayu, R.W.; Putra, M.E.; Wulansari, M.; Setiadi, B.; Arisal, A.; Razi, P.; Arief, S. Directivity of Coseismic Ionospheric Disturbances Propagation Following the 2016 West Sumatra Earthquake Using Three-Dimensional Tomography GNSS-TEC. *Atmosphere* **2022**, *13*. doi:10.3390/atmos13091532.

341. Song, R.; Hattori, K.; Zhang, X.; Sanaka, S. Seismic-ionospheric effects prior to four earthquakes in Indonesia detected by the China seismo-electromagnetic satellite. *Journal of Atmospheric and Solar-Terrestrial Physics* **2020**, *205*, 105291. doi:https://doi.org/10.1016/j.jastp.2020.105291.
342. Marchetti, D.; De Santis, A.; Shen, X.; Campuzano, S.A.; Perrone, L.; Piscini, A.; Di Giovambattista, R.; Jin, S.; Ippolito, A.; Cianchini, G.; Cesaroni, C.; Sabbagh, D.; Spogli, L.; Zhima, Z.; Huang, J. Possible Lithosphere-Atmosphere-Ionosphere Coupling effects prior to the 2018 Mw=7.5 Indonesia earthquake from seismic, atmospheric and ionospheric data. *J. Asian Earth Sci.* **2020**, *188*, 104097. doi:https://doi.org/10.1016/j.jseaes.2019.104097.
343. Zong, J.; Tao, D.; Shen, X. Possible ELF/VLF Electric Field Disturbances Detected by Satellite CSES before Major Earthquakes. *Atmosphere* **2022**, *13*. doi:10.3390/atmos13091394.
344. Jia, D.; Yu, H.; Zhao, B.; Ma, Y. Geothermal Anomalies and Coupling with the Ionosphere before the 2020 Jiashi Ms6.4 Earthquake. *Applied Sciences* **2023**, *13*. doi:10.3390/app13053019.
345. Raleigh, B.; Bennett, G.; Craig, H.; Hanks, T.; Molnar, P.; Nur, A.; Savage, J.; Scholz, C.; Turner, R.; Wu, F. Prediction of the Haicheng earthquake. *Eos Trans. AGU* **1977**, *58*, 236–272.
346. Teng, T. *Ground water radon content as an earthquake precursor*; Geol. Surv. Open File Rep., U. S. 80-6, 1980; pp. 357–360.
347. Wang, C.Y. Some aspects of the Tangshan (China) earthquake of 1976. *Chin Geophys.* **1978**, *1*, 157–172.
348. Allegri, L.; Bella, F.; Della Monica, G.; Ermini, A.; Improta, S.; Sgrigna, V.; Biagi, P.F. Radon and tilt anomalies detected before the Irpinia (south Italy) earthquake of November 23, 1980 at great distances from the epicenter. *Geophys. Res. Lett.* **1983**, *10*, 269–272. doi:https://doi.org/10.1029/GL010i004p00269.
349. Igarashi, G.; Wakita, H. Groundwater radon anomalies associated with earthquakes. *Tectonophysics* **1990**, *180*, 237–254. doi:https://doi.org/10.1016/0040-1951(90)90311-U.
350. Humanante, B.F.; Giroletti, E.; Idrovo, J.; Monnin, M.; Pasinetti, R.; Seidel, J.L. Radon signals related to seismic activity in Ecuador, March 1987. *pure and applied geophysics* **1990**, *132*, 505–520.
351. Virk, H.S.; Singh, B. Radon recording of Uttarkashi earthquake. *Geophys. Res. Lett.* **1994**, *21*, 737–740. doi:https://doi.org/10.1029/94GL00310.
352. Walia, V.; Virk, H.S.; Bajwa, B.S. Radon Precursory Signals for Some Earthquakes of Magnitude > 5 Occurred in N-W Himalaya: An Overview. *Pure and Applied Geophysics* **2006**, *163*, 711–721. doi:10.1007/s00024-006-0044-z.
353. Richon, P.; Sabroux, J.C.; Halbwachs, M.; Vandemeulebrouck, J.; Poussielgue, N.; Tabbagh, J.; Punongbayan, R. Radon anomaly in the soil of Taal volcano, the Philippines: A likely precursor of the M 7.1 Mindoro earthquake (1994). *grl* **2003**, *30*, 1481. doi:10.1029/2003GL016902.
354. Yasuoka, Y.; Ishii, T.; Tokonami, S.; Ishikawa, T.; Narazaki, Y.; Shinogi, M. Radon anomaly related to the 1995 Kobe earthquake in Japan. *International Congress Series* **2005**, *1276*, 426–427. doi:https://doi.org/10.1016/j.ics.2004.10.011.
355. Goto, M.; Yasuoka, Y.; Nagahama, H.; Muto, J.; Omori, Y.; Ihara, H.; Mukai, T. Anomalous changes in atmospheric radon concentration before and after the 2011 northern Wakayama Earthquake (Mj 5.5). *Rad.Prot. Dos.* **2016**, *174*, 412–418. doi:10.1093/rpd/ncw142.
356. Ilic, R.; Rusov, V.; Pavlovych, V.; Vaschenko, V.; Hanzic, L.; Bondarchuk, Y. Radon in Antarctica. *Radiat. Meas.* **2005**, *40*, 415–422.
357. Das, N.K.; Choudhury, H.; Bhandari, R.; Ghose, D.; Sen, P.; Sinha, B. Continuous monitoring of ²²²Rn and its progeny at a remote station for seismic hazard surveillance. *Radiat. Meas.* **2006**, *41*, 634–637. doi:https://doi.org/10.1016/j.radmeas.2006.03.003.
358. Jaishi, H.P.; Singh, S.; Tiwari, R.P.; Tiwari, R.C. Temporal variation of soil radon and thoron concentrations in Mizoram (India), associated with earthquakes. *Nat. Hazards* **2014**, *72*, 443–454.
359. Deb, A.; Gazi, M.; Barman, C. Anomalous soil radon fluctuations - signal of earthquakes in Nepal and eastern India regions. *Journal of Earth System Science* **2016**, *125*, 1657–1665.

Disclaimer/Publisher's Note: The statements, opinions and data contained in all publications are solely those of the individual author(s) and contributor(s) and not of MDPI and/or the editor(s). MDPI and/or the editor(s) disclaim responsibility for any injury to people or property resulting from any ideas, methods, instructions or products referred to in the content.